Domain wall propagation in soft magnetic wires with periodical width modulation

Olga Lozhkina, M.Sc.

born in Lazaritskaya Luka, Russia

Disseration for Attaining the Academic Degree of
Doctor Rerum Naturalium (Dr. rer. nat.)
of the Departments 08 – Physics, Mathematics and Computer Science,
09 – Chemistry, Pharmacology, and Geoscience, 10 – Biology,
and University of Medicine of the Johannes Gutenberg University

Max Planck Graduate Center

Johannes Gutenberg University of Mainz

MAY 2023

Scientific supervisors

Prof. Dr. Mathias Kläui,

University of Mainz

Institute of Physics

Prof. Dr. - Ing. Tilmann Beck

Technical University of Kaiserslautern

Department of Mechanical and Process Engineering

Mentor

Prof. Dr. Gerhard Jakob

University of Mainz

Institute of Physics

Abstract

The relentless pursuit of shrinking computation devices, enhancing their power, reducing energy consumption, and eliminating excessive heat has brought magnetic sensors and spintronics into the spotlight in recent years. These simple, small, and robust magnetic sensors offer high sensitivity, often accompanied by non-volatility and non-contact operation. By incorporating spin as an additional degree of freedom in computation, integration density and computation speed can be improved compared to conventional systems.

Permalloy ($Ni_{81}Fe_{19}$) is a commonly used material for magnetic sensors due to its low coercivity and negligible magnetostriction. The deposition conditions of permalloy thin film using magnetron sputtering were investigated to achieve films with the lowest possible coercivity and controlled anisotropy for magnetoresistive sensor applications. Varying the inert gas pressure, deposition power and magnetic fields during growth is used to obtain films with controlled anisotropy and low coercivity. A robust method for characterising the intrinsic magnetic anisotropy of the films is developed and the possibility of suppressing magnetic anisotropy by introducing a rotating magnetic field during sputtering is demonstrated.

Among other spintronic concepts the study of domain wall propagation in magnetically soft nanowires is gaining attention for the potential use in logic, memory and sensor devices. Using micromagnetic simulations, it is shown that a periodic modulation of the wire width can completely eliminate the Walker breakdown of a field-driven domain wall for a certain field range, while preserving the domain wall spin structure over the entire operating field range of a device. The effectiveness of this wire width modulation depends on the width and thickness of the wire, with smaller wires showing the greatest benefit in extending the field operation window. The simulation of crossing magnetic wires also shows the importance of suppressing the Walker breakdown.

The experimental results support the findings that the efficiency of the Walker breakdown suppression depends on the geometry of the magnetic wire, with the domain wall velocity as a function of applied field strength showing a significantly lower slope in modulated wires, in contrast to the sharp peaks associated with Walker breakdown in straight magnetic wires.

Zusammenfassung

Das unablässige Verkleinern von elektronischen Bauteilen mit größerer Leistung und verringertem Energieverbrauch bei Vermeidung übermäßiger Hitze hat in den letzten Jahren magnetische Sensoren und Spintronik ins Rampenlicht gerückt. Diese simplen, kleinen, aber robusten magnetischen Sensoren bieten eine hohe Empfindlihckeit, die mit einer Nichtflüchtigkeit und einem kontaktlosen Betrieb einhergeht. Durch Einbeziehung des Spins als zusätzlichen Freiheitsgrad in die Berechnung können die Integrationsdichte und die Rechnungsgeschwindigkeit im Vergleich zu herkömmlichen Systemen verbessert werden.

Permalloy ($Ni_{81}Fe_{19}$) ist aufgrund seiner geringen Koerzitivfeldstärke und vernachlässigbarer Magnetostriktion ein häufig verwendetes Material für Magnetsensoren. Optimale Bedingungen für die Abscheidung von Permalloy (Ni81Fe19)-Dünnschichten durch Magnetron-Sputtern werden untersucht, um weichmagnetische Schichten für magnetoresistive Sensoren zu erhalten. Durch Variation des Inertgasdrucks, der Sputterrate und der Magnetfelder während des Wachstums werden Schichten mit kontrollierter Anisotropie und niedriger Koerzitivfeldstärke erhalten. Eine robuste Methode zur Charakterisierung der magnetischen Anisotropie der Schichten wird entwickelt und die Möglichkeit der Unterdrückung der magnetischen Anisotropie durch rotierende Magnetfelder während des Sputterns demonstriert.

Die Untersuchung der Ausbreitung von Domänenwänden in weichmagnetischen Nanodrähten gewinnt wegen ihrer potenziellen Anwendung in Logik-, Speicher- und Sensor-konzepten an Bedeutung. Mikromagnetische Simulationen zeigen, dass eine periodische Modulation der Drahtbreite den Walker-Breakdown einer feldgetriebenen Domänenwand unterdrücken kann. Die Wirksamkeit hängt von der Breite und Dicke des Drahtes ab, wobei die Modulation bei kleineren Drähten die größte Verbesserung bringt. Simulationen von sich kreuzenden Magnetdrähten zeigen, wie wichtig die Unterdrückung des Walker-Breakdowns ist.

Die experimentellen Ergebnisse bestätigen, dass die Wirksamkeit der Unterdrückung des Walker-

Breakdowns von der Form des Magnetdrahtes abhängt, wobei die Domänenwandgeschwindigkeit als Funktion der angelegten Feldstärke bei modulierten Drähten eine deutlich geringere Steigung aufweist, im Gegensatz zu den scharfen Spitzen, die mit dem Walker-Durchbruch in geraden Magnetdrähten verbunden sind.

Contents

List of Figures

Acknowledgements

I would like to express my deepest gratitude to my scientific supervisors, Prof. Mathias Kläui, Prof. Gerhard Jakob, Prof. Tilmann Beck, Dr. Robert Reeve and Dr. Robert Frömter, for their invaluable guidance, support and mentorship throughout my PhD studies. Their expertise, critical insights and encouragement were essential to the successful completion of my thesis. I am honoured to have had the opportunity to work under their supervision.

To my mother, for her unconditional love, support and encouragement throughout my educational journey, I would like to express my sincere gratitude. Her sacrifices, both financial and emotional, have been a constant source of motivation for me.

I would like to express my deepest gratitude to Dr. Rita Morgan, my therapist, for her guidance and support throughout my struggles. Her expertise, compassion and understanding have been instrumental in helping me navigate through the difficult times and regain control of my life.

I would like to express my deepest gratitude to my colleagues and friends, Tobias Reimer, Anja Dion, Pascal Krautscheid, Mehran Vafaee, Sven Becker, Satya Prakash, Fabian Kammerbauer, Mona Bhukta and Mandy Syskaki, for their invaluable help and support in familiarising me with the equipment, techniques and approaches used in my research. Their expertise and willingness to share their knowledge were crucial to the success of my work. I am especially grateful for their camaraderie and support, which made the research experience enjoyable and rewarding.

Declaration

I hereby declare that I wrote the dissertation submitted without any unauthorized external assistance and used only sources acknowledged in the work. All textual passages which are appropriated verbatim or paraphrased from published and unpublished texts as well as all information obtained from oral sources are duly indicated and listed in accordance with bibliographical rules. In carrying out this research, I complied with the rules of standard scientific practice as formulated in the statutes of Johannes Gutenberg University Mainz to insure standard scientific practice.

Olga Lozhkina

Abbreviations

- AFM – atomic force microscopy
- AMF – aligning magnetic field
- AMR – anisotropic magnetoresistance
- ATW – asymmetric transverse domain wall
- CCW – counter-clock-wise
- CMOS – complementary metal–oxide–semiconductor
- CW – clock-wise
- DC – direct current
- DW – domain wall
- EBL – electron beam lithography
- FOW – field operating window
- FS – Fuchs-Sondheimer model
- GMR – giant magnetoresistance
- GPU – graphics processing unit
- LED – light-emitting diode
- LLG – Landau-Lifshitz-Gilbert equation
- MOKE – magnetooptical Kerr effect
- MS – Mayadas-Shatzke model
- PHE – planar Hall effect
- Py – permalloy, Fe_xNi_{1-x}
- RF – radio frequency
- RMF – rotating magnetic field
- RMS – root-mean square
- SQUID – superconducting quantum interference device
- STW – symmetric transverse domain wall

- SZM – structure zone model
- TDR – time-domain reflectometry
- TW – transverse domain wall
- VW – vortex domain wall
- VW – vortex domain wall
- WB – Walker breakdown
- XRD – X-Ray diffraction
- XRR – X-Ray reflection
- ZMF – zero magnetic field
- rpm – revolutions per minute

Introduction

Since the formulation of Moore's Law, integrated circuits have been expected to reach the limit of transistor density at some point. Great efforts are constantly being made to further shrink device dimensions and increase computing power, reduce power consumption and dissipate excess heat [1, 2]. New approaches such as new transistor architectures, 3D stacking, advanced lithography techniques and new materials are needed to keep pace with increasing transistor densities in the future. Alongside these efforts, it's also worth exploring emerging beyond-CMOS (complementary metal–oxide–semiconductor) technologies. The discovery of giant magnetoresistance (GMR) [3] in the last quarter of the 20th century has drawn considerable attention to the relationship between magnetism and transport phenomena, leading to investigations into the use of spin for both fundamental understanding and technical applications. Spintronics exploits the spin property of electrons in addition to their charge property [4]. Incorporating the spin property and adding another degree of freedom offers potential advantages such as non-volatility, improved computing speed, reduced power consumption and increased integration density compared to conventional semiconductor devices.

One of the key advantages of spintronics is the ability of ferromagnetic materials to retain their magnetisation even when external magnetic fields are removed, which has sparked interest in the computer hardware industry to replace semiconductor-based components with magnetic ones. Spintronics also potentially requires less power to operate than conventional electronics, and the spin is thought to be more stable and reliable than charge when exposed to external factors such as temperature, pressure or radiation. Therefore, devices based on spintronics are expected to perform better than electronic devices in high-temperature or radiation environments. Conceptually, spintronic devices could be

smaller, faster and more durable than electronic devices [5].

Advanced processing techniques employed in spintronics enable the fabrication of reproducible confined soft magnetic wires, in which domain walls (DWs) [6] can be readily manipulated through the application of magnetic fields or electric currents. This, together with various magnetoresistance methods for detecting the orientation of magnetic domains, makes magnetic DWs of great interest for various applications such as non-volatile logic [7], memory [8] devices and magnetic sensors [9, 10]. The propagation of magnetic DWs in nanowires has also recently gained attention in the scientific community as a potential information carrier for neuromorphic computing [11, 12, 13] due to its inherently stochastic behaviour.

Certain crucial requirements must be realized to ensure the effective utilization of domain walls in soft magnetic wires for practical device applications. For current-driven domain walls, achieving a low threshold current density is critical. Additionally, high domain-wall velocities are essential for optimal device performance, while stability and controllability of domain wall position are vital for memory and sensing applications. Moreover, controlled stochasticity is beneficial to neuromorphic computation [5].

The development of new spintronic device concepts is closely linked to materials science, as metallic films play a critical role in many modern technologies that affect our daily lives, including integrated circuits, information storage systems, displays and sensors. These technologies require the exploitation of the unique electronic, magnetic, optical, mechanical and thermal properties of metallic materials [14].

The range of topics discussed in this thesis includes the investigation of the optimum conditions for depositing soft ferromagnetic permalloy films. The goal is to minimize the coercivity and control the anisotropy, both crucial for obtaining efficient domain wall propagation in magnetic sensors. Additionally, enhancing the magnetoresistance ratio is explored to improve the efficiency of sensor readout. The second part of this thesis focuses on the investigation of the DW propagation patterns in confined ferromagnetic nanowires. Efforts are made to manipulate and regulate their stochastic behavior, aiming to achieve improved reliability and greater control over the domain wall dynamics.

Chapter 1

Theoretical background

This chapter of the thesis presents the theoretical foundations that underlie the experimental work. The concept of magnetism is introduced by explaining how the properties of electrons in atoms give rise to the collective phenomenon of ferromagnetism. The dynamics of magnetism are described using the Landau-Lifshitz-Gilbert (LLG) equation, which accounts for the influence of external magnetic fields on the magnetization of a material. The Stoner-Wohlfarth model is introduced as a simplified model that is suitable for analysing magnetization switching in thin films of ferromagnetic materials.
Micromagnetic simulations, which use the LLG equation to study magnetic phenomena at the nanoscale, are described in terms of simulating magnetic domain walls (DWs) in confined permalloy wires. The chapter concludes by discussing the patterns of in-plane magnetic DW behaviour observed in simulations and experiments, including their pinning, propagation, and nucleation.

1.1 Microscopic origin of ferromagnetism

The angular momentum of an atom is a fundamental property that arises from the combined contributions of the orbital and spin angular momenta of its electrons. Protons and neutrons also both carry magnetic moment, but the magnetism created by electrons is larger and dominates the nuclear term. The magnitudes of these electron angular momenta, as well as their interaction, underlie the magnetic properties of atoms and their

compounds. The atomic spin angular momentum is is represented by the sum of the individual spin angular momenta, $\vec{S} = \Sigma\vec{s_i}$. Similarly, the atomic orbital angular momentum is represented by the sum of the individual orbital angular momenta, $\vec{L} = \Sigma\vec{l_i}$. The total angular momentum of an atom is the sum of its orbital and spin angular momenta, and $\vec{J} = \vec{L} + \vec{S}$ [15]. This quantity describes the magnetic properties of individual atoms. The saturation magnetic moment $M_s = -gM_BJ$, where g is g-factor and M_B is the Bohr magneton.

The magnetic moment of an atom is a measure of its intrinsic magnetic properties, and is determined by the presence or absence of unpaired electrons. When two electrons have opposite spins, their contributions to the magnetic moment cancel each other out. This means that the magnetic moment is due to the presence of unpaired electrons, which do not have a partner with opposite spin to cancel out their contribution.

When two atoms with unpaired electrons interact, an exchange interaction can occur between them. This interaction is described by the Heisenberg model [16] and is characterized by an energy term $E = -2J_{ex}S_iS_j$ that is related to the overlap of the charge distributions of the two atoms. The exchange integral J_{ex} is a measure of the strength of this interaction. Ferromagnetism occurs when the exchange interaction between the spins of adjacent atoms has a positive value. In this case, the exchange energy is minimized when the spins are parallel.

Elements with incomplete d-electron shells, known as transition elements, tend to have particularly interesting magnetic properties due to the presence of unpaired electrons. In solid state materials, electron bands formed by the d-shells have a high density of states. The presence of unpaired electrons on high-density $3d$-shells and relatively small interatomic distances in materials such as iron, cobalt, and nickel result in a positive exchange energy, which favors the parallel alignment of electron spins. This positive exchange energy gives rise to ferromagnetism [17].

The unusual magnetic properties of ferromagnets are reflected in the hysteresis of their magnetization curves. At zero external field, ferromagnets can exhibit a zero or non-zero net magnetization, depending on the history of applied fields. When an external field is applied, the magnetization of the material increases non-proportionally until it reaches the saturation magnetization, which is characteristic of the material and temperature.

When the field is reversed, the magnetization decreases and may remain non-zero at zero field.

This behavior was explained by Weiss [18], who proposed the existence of spontaneously magnetized regions within ferromagnetic materials. These regions, known as magnetic domains, are formed by the electron spins and magnetic moments that are arranged parallel to each other by internal interactions. Thermal fluctuations can affect the stability of the magnetic domains, but the internal interactions within the domains tend to counteract these fluctuations and maintain the alignment of the magnetic moments. The spin-orbit interaction also plays a role in determining the possible magnetic orientations of the magnetic domains, since the electron orbits are connected with the crystallographic structure of the material. This effect is known as magnetocrystalline anisotropy [17].

1.2 Domains and domain walls

Magnetic domain walls (DWs) are boundaries within a magnetic sample that separate different domains. These domains may be present to minimize the magnetostatic energy or may be a result of the sample's magnetic history. DWs tend to form in a way that avoids the creation of magnetic charges, which can contribute to magnetostatic energy. One type of DW is the Bloch wall, which forms at a 180° angle and has magnetization within the plane of the wall [19] (Figure 1.1). The wall width, known as the parameter δ, is determined by minimizing the energy of the domain wall by equating the derivative of the wall energy with respect to delta to zero.

Néel recognized the reduced symmetry at the surface of ferromagnets [20] and proposed using volume charge instead of surface charge as a way to lower the total energy [21]. In thin films, the perpendicular magnetization in a Bloch wall causes strong surface charges, so to minimize the total energy the magnetization rotates within the of the DW, which is known as a Néel wall (Figure 1.1).

In the intermediate film thickness region between Bloch and Néel domain wall types, it

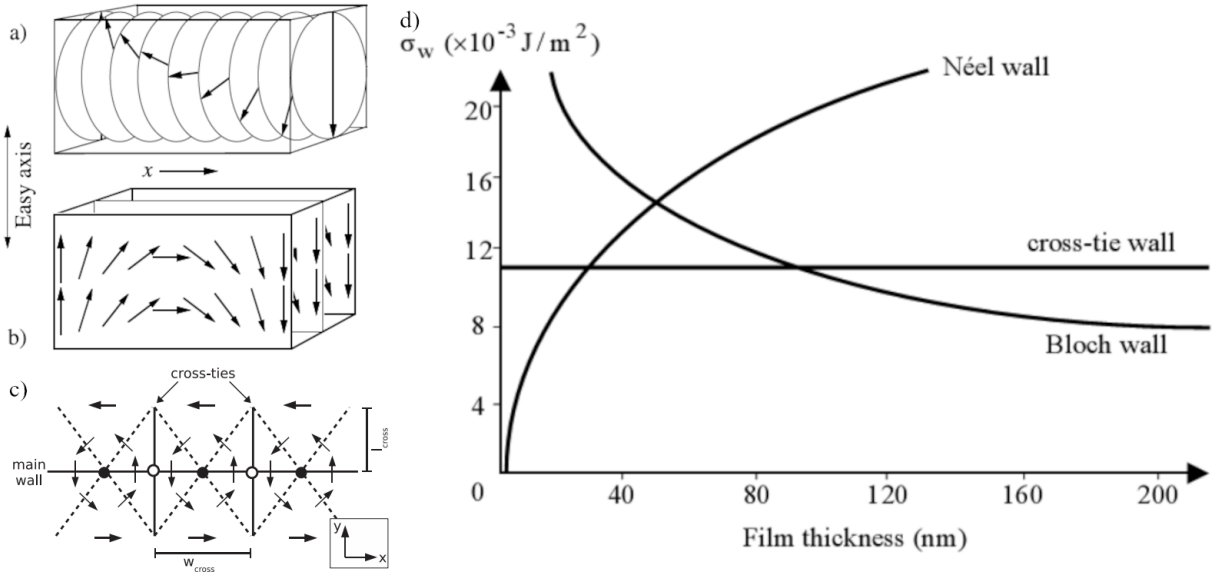

Figure 1.1: Schematics of the rotation of the magnetization vector for (a) Bloch [19], (b) Néel [22], and (c) cross-tie domain walls [23] and (d) a phase diagram of a permalloy film showing the energy density of Néel walls, Bloch walls, and cross-tie walls as a function of film thickness [24]

is possible to minimize energy by forming cross-tie domain walls. Here, the structure of the wall varies continuously along its length, comprising alternating Néel and Bloch sections [23]. The domain wall phase diagram of a permalloy ($Ni_{80}Fe_{20}$) film, which illustrates the relationship between the thickness of the wall and its energy density (σ_w), is presented in Figure 1.1 [24]. Magnetization swirls which occur to minimize magnetic flux as much as possible, are called vortices. Magnetization vortices, commonly found in ferromagnetic patterned films with a small amount of stray field, can be observed in various structures, such as permalloy discs of appropriate thickness.

1.3 Ferromagnetic switching: The Stoner-Wohlfarth model

Ferromagnetic materials can be subjected to an external magnetic field, which will cause the net magnetic moment of the material to increase. This increase in moment will eventually reach a maximum value known as the saturation magnetization. The process of magnetization involves the movement of domain walls and the rotation of the magnetiz-

ation of the domains.

The way in which thin films change their magnetization direction is typically examined using two main models: the rotation of a single, isolated magnetic particle and the movement of a domain wall. The first mathematical explanation of reversal through domain wall movement was described by Kondorsky [25]. Essentially, reversal through domain wall motion is a two-step process, involving the formation of reverse domains with domain walls, followed by the movement of the domain wall. The initial formation of these reverse domains is random across the film, and the reasons for this are not yet fully understood. However, it is known that factors such as crystal defects, the alignment of grains, and even strain can all influence the magnetic properties of the film and create areas where reversal is more likely to occur.

If a magnetic field is applied parallel to the magnetization of one of two domains separated by a domain wall, the displacement of the domain wall will result in an increase in the volume of the domain magnetized in the same direction as the field, and a decrease in the volume of the domain magnetized in the opposite direction (Figure 1.2). This results in an overall increase in the magnetization.

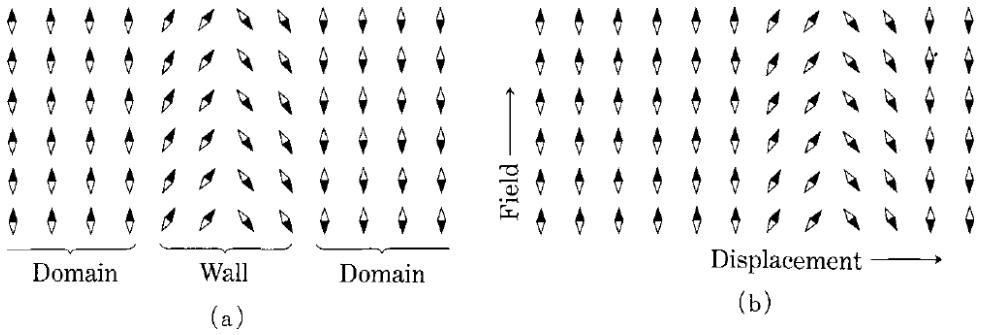

Figure 1.2: Magnetic domain wall displacement scheme [26]

The polar distribution of domain magnetizations changes as the field strength increases, as shown in Figure 1.3. Starting from a demagnetized state with an isotropic distribution of magnetizations, the magnetizations pointing in the negative direction are reversed as the field increases in the positive direction. This results in an increased population of magnetizations in the positive hemisphere. At a high enough field strength, all of the magnetizations will be nearly parallel to the field direction, which is the saturated state. As the field is reduced from this saturated state, the domain magnetizations will rotate

back towards the nearest positive easy direction and will cover a hemisphere at the residual magnetization point. If the field is then increased in the negative direction, the most energetically unfavourable magnetization (in the positive direction) will be reversed first, resulting in a net magnetization of zero at a certain field intensity known as the coercive field. This coercive field is a measure of the stability of the residual magnetization. Further increases in the field in the negative direction will result in negative saturation.

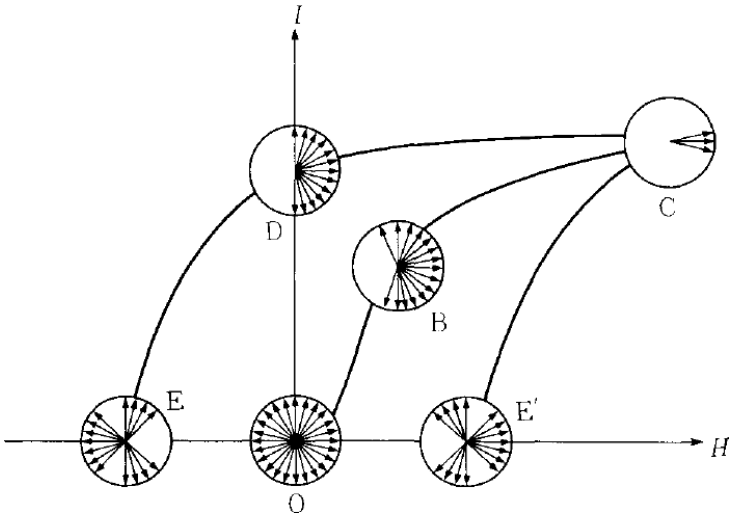

Figure 1.3: Magnetic domain wall displacement scheme [26]

The Stoner-Wohlfarth model [27] is a simplified model that is used to understand and predict the behavior of ferromagnetic materials when subjected to external magnetic fields. This model is based on the assumption that the material consists of small, non-interacting particles, whose spins are held parallel by the exchange energy.

One key feature of the Stoner-Wohlfarth model is that it assumes the material has a certain type of anisotropy, which refers to the preferential alignment of the particles' spins in a particular direction. In the original version of this model, the shape anisotropy of the particles was considered, which refers to the fact that the particles have a preferred direction of alignment due to their shape. For example, if the particles are elongated in a certain direction, they will have a tendency to align their spins along that direction. Alternatively, the model can be modified to consider uniaxial crystalline anisotropy, which occurs when the particles have a preferred direction of alignment due to the crystal structure of the material.

Overall, the Stoner-Wohlfarth model provides a useful way to understand the behavior

of ferromagnetic materials when subjected to external magnetic fields. This model is a widely used approximation in the field of magnetism and has been useful in predicting and explaining the behavior of a variety of ferromagnetic materials.

Slonczewski combined the stable solutions of the Stoner-Wohlfarth model and derived magnetization hysteresis curves of a uniaxial particle [28]. Figure 1.4 represents the magnetization shown as a function of the external longitudinal field. The field is expressed in terms of the anisotropy field $H_k = \frac{2K}{M_s}$.

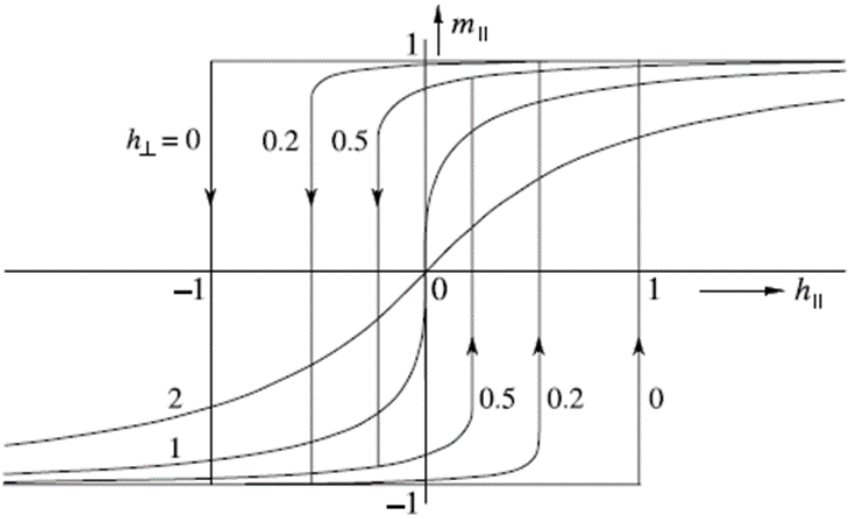

Figure 1.4: Derived hysteresis loops for a uniaxial particle [22]

The Stoner-Wohlfarth model is a widely applicable theory that is able to accurately describe a wide range of objects, including nanoparticles [29] and thin permalloy films [17, 30].

1.4 Landau-Lifshitz-Gilbert equation

Landau and Lifshitz [31] provided a comprehensive understanding of the formation and boundaries of domains, known as domain walls. In their work, they developed the energy terms that govern domain formation and the internal structure of domain walls as well as a domain configuration that minimizes stray fields (Landau flux-closure pattern). The formalism employs a continuum approximation, wherein individual atomic magnetic properties are replaced by averaging them over a small volume of space (several nm^3) by

assuming a continuous variation in magnetization direction within the region [32]. The Landau free energy is the sum of the individual energy contributions described above:

$$G(M) = E_{\text{exchange}} + E_{\text{Zeeman}} + E_{\text{dipole-dipole}} + E_{\text{anisotropy}}.$$

These energy contributions are expressed as functionals of the continuous variables magnetization $\vec{M}(x)$ or reduced magnetization $\vec{m}(x) = \frac{\vec{M}(x)}{M_s}$ instead of discrete atomic spins, where M_s is saturation magnetization. At a constant temperature, the sum of these energy terms is referred to as the Landau free energy. The Landau free energy describes an isothermal isobaric thermodynamic system with magnetization as an additional order parameter [33]. The Landau free energy has minima at thermodynamically stable magnetization configurations.

Exchange energy: In ferromagnets, the positive exchange constant favors the alignment of neighboring spins in the same direction. The presence of magnetization gradients $\nabla\vec{m}$ increases the energy, which is represented by the following term:

$$E_{\text{exchange}} = A \int dV (\nabla\vec{m})^2.$$

Here, A is a stiffness parameter that promotes the alignment of neighboring spins. Its value is proportional to the exchange integral J_{ex}.

Zeeman energy: The Zeeman energy of a magnetic moment $\vec{M}$ in an external magnetic field $\vec{H}$ is given by $E = -\vec{M} \cdot \vec{H}$. The whole magnetization contributes to the energy of the system, called the Zeeman energy, which is calculated as

$$E_{\text{Zeeman}} = -\mu_0 M_s \int dV \vec{H}(\vec{r}) \cdot \vec{m}(\vec{r}),$$

where μ_0 is the vacuum magnetic permeability. **Stray field energy:** The magnetization $\vec{M}(\vec{r})$ creates a magnetic field called the demagnetizing field $\vec{H}_d$: $\nabla \cdot \vec{H}_d = \nabla \cdot \vec{M}$. The demagnetizing field leads to an additional energy contribution known as the dipolar energy. This energy is similar to the Zeeman energy, but it arises from the field produced by the

sample's magnetization instead of an external field:

$$E_{\text{dipole-dipole}} = -\frac{1}{2}\mu_0 M_s \int dV \vec{H}_d \cdot \vec{m}(\vec{r}).$$

The demagnetizing field for a given magnetization and sample shape can be calculated by integrating over the entire volume and surface of the sample. However, a direct solution for this calculation is only possible for simple geometric shapes.

Anisotropy energies: The existence of preferred directions for magnetization are known as anisotropy. There are several possible causes of anisotropy, including mechanical stresses (magnetoelastic anisotropy), lattice mismatches, spin-orbit interaction (magnetocrystalline anisotropy), and the shape of the sample. While the shape anisotropy is naturally accounted for in the dipolar contribution, other forms of anisotropy are included in a more phenomenological way. The energy contribution due to anisotropy is modeled as an arbitrary function, $\varepsilon_{anisotropy}(\vec{m}(\vec{r}))$, of the magnetization:

$$E_{\text{anisotropy}} = \int dV \varepsilon_{\text{anisotropy}}(\vec{m}(\vec{r})).$$

In the case of a uniaxial anisotropy with a single preferred direction, the first-order approximation is $\varepsilon_{\text{anisotropy}}(\vec{m}(\vec{r})) = -K_1 cos^2\theta$, where θ is the angle between the easy axis and the magnetization [17].

Landau-Lifshitz-Gilbert equation The Landau-Lifshitz-Gilbert (LLG) equation is a mathematical model that describes the dynamics of magnetization in a material. It is based on the idea that a magnetization behaves like an angular momentum, which can precess in response to an external magnetic field. In the LLG equation, the magnetization $\vec{m}$ is subject to a torque that is proportional to the cross product of the magnetization and the effective magnetic field $\vec{H}$: $\frac{\partial \vec{m}}{\partial t} = \gamma \vec{m} \times \vec{H}$. Here, γ is the gyromagnetic ratio, which characterizes the strength of the precessional motion.

The LLG equation also includes a term that accounts for damping, or the dissipation of energy from the system proportional to the velocity $\frac{\partial \vec{m}}{\partial t}$ [34]:

$$\frac{\partial \vec{m}}{\partial t} = -\gamma \vec{m} \times \vec{H} + \alpha_G \vec{m} \times \frac{\partial \vec{m}}{\partial t}.$$

The coefficient α_G, known as the damping coefficient, characterizes the strength of the damping. It is determined by various physical processes, including spin-wave excitations and spin-orbit coupling, and can be measured using techniques such as ferromagnetic resonance spectroscopy [35].

1.5 Micromagnetic simulations

Micromagnetic simulations [32] provide a useful tool for studying the magnetic structure and dynamics of a variety of magnetic systems. With the increasing power of computers, there has been a rise in the use of these simulations in both fundamental and applied sciences.

In ferromagnets, the spontaneous magnetization tends to align parallel to form a single domain. In a finite size ferromagnet, fully aligned spins produce free magnetic poles at the surface, which leads to an increase in magnetostatic energy. This energy is minimized at the expense of exchange and magnetocrystalline energies. The Landau-Lifschitz theory [31] deals with an infinite crystal in one dimension without magnetostatic energy contribution. Later, Néel highlighted the importance of the broken symmetry at the surface of ferromagnets [21]. The Landau-Lifschitz theory was further developed in the 1940-1970s by Brown [36] to extend it to three dimensions. Micromagnetics describes domains and walls using continuous local magnetization. Exact solutions to the LLG are not possible for most problems due to their non-linearity and non-locality. Instead, numerical calculations of discretized samples are used to analyze and predict the magnetic structure and its dynamics.

This work focuses on the magnetization dynamics in nanowires with rectangular cross-sections, so the finite differences method can be applied. This method enables a much faster magnetostatic solution, which is the primary use of computing time, by evaluating the convolution product of charges through fast Fourier transformation for identical cells

instead of direct summation.

Another approach for simulating the magnetization of nanowires is to consider only a restricted region that includes the domain wall moving between two antiparallel domains and mimicking an infinitely long wire by removing the magnetostatic charges at the ends [37].

1.5.1 Domain wall structure in soft ferromagnetic in-plane magnetized wires

Thin films of soft magnetic materials often exhibit shape anisotropy, which causes the magnetization to align in the plane of the film [20, 17]. When nanowires are patterned from these thin films ($t \ll w$), the magnetization is governed by shape anisotropy, resulting in only two possible magnetization directions that are parallel to the wire axis. Under external fields, magnetic domain walls between antiparallel domains can move as the co-directional domain tends to expand and the opposing domain shrinks. There are several possible types of domain walls with complex structures that can exist in soft magnetic nanowires [38, 39]:

- symmetric (STW) and asymmetric transverse domain walls (ATW)
- vortex walls (VW)
- in wide strips, double and triple domain walls can be present [40]
- cross-tie and diamond structures exist at large widths and intermediate thicknesses [41]
- Landau domain walls are observed in nanostrips with larger thicknesses (around >55 nm in permalloy) [42] and Bloch-point walls are observed when the thickness is close to the nanowire width [43].

These structures can be stable or metastable depending on the wire sizes. Our study is limited to the first three types due to the investigated wire sizes (10-30 nm wire thickness t and 100-200 wire width w).

Transverse domain walls are stable in the range of small thicknesses and widths of soft magnetic wires. Their magnetic moments are oriented in-plane, perpendicular to the wire

(Figure 1.5). The domain wall has a triangular shape, with a half anti-vortex at the apex and a half-hedgehog vortex at the opposite end. A variant of this structure is stable at higher wire thicknesses: the two half-vortices are no longer aligned in the perpendicular direction.

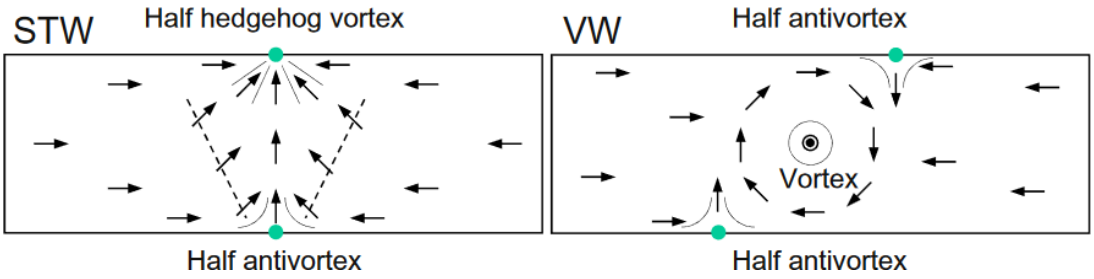

Figure 1.5: Schematic structures of the symmetric transverse (STW) and vortex (VW) domain walls [37]

The vortex domain wall consists of a full vortex with an out-of-plane core and two half-antivortices at the edges of the nanowire (Figure 1.5). The vortex wall has lower magnetostatic energy at the expense of higher exchange energy. Equal-energy lines separate thickness-width ranges corresponding to stable STW, ATW, and VWs (Figure 1.6). In order to transform one domain wall into another type, an energy barrier must be overcome, which allows for the presence of metastable domain walls outside their phase diagram range. The experimental verification of the domain wall phase diagram was achieved through photoemission electron microscopy [41] and scanning electron microscopy with polarization analysis [44] imaging techniques.

The width of the domain wall, δ_{DW}, can be approximately determined using the formula $\delta_{DW} \approx \frac{3}{\pi} w$ for symmetric transverse walls and $\delta_{DW} \approx \frac{3}{4} w$ for vortex walls (as shown in reference [45]). This relationship demonstrates a linear increase in δ_{DW} with wire width w, with a more pronounced effect for vortex walls. Both of these structures show little dependence on nanowire thickness, but for asymmetric transverse walls, δ_{DW} increases with both nanowire width and thickness.

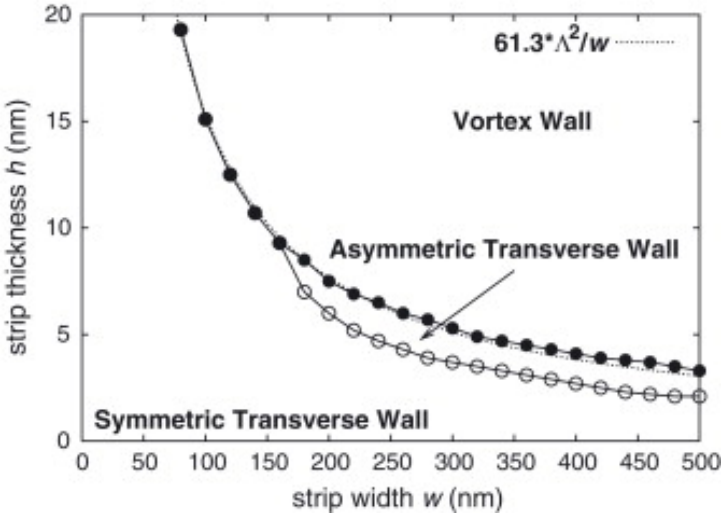

Figure 1.6: Domain wall phase diagram mapping stable DW configurations in permalloy nanostrips [37, 45]

1.5.2 Field-driven domain wall dynamics

Under low external magnetic fields parallel to the wire, all domain wall structures demonstrate steady propagation (Figure 1.7 a) with a linear or slightly curved velocity dependence on the applied magnetic field amplitude. The magnetization rotates, moving the domain walls, and the damping term in the LLG acts like a viscous friction. The structure does not change while moving, and thus this regime is called stationary motion.

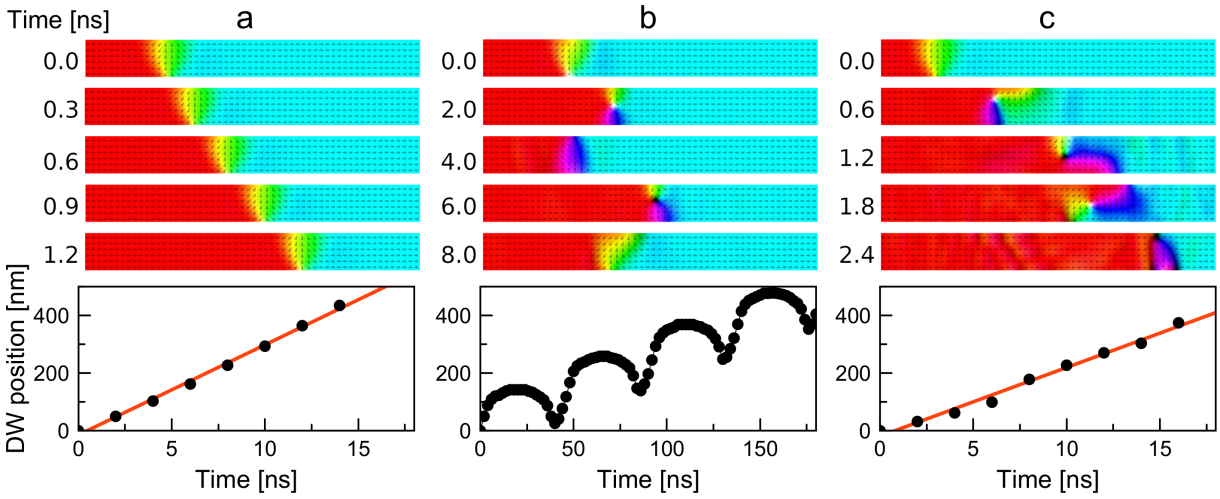

Figure 1.7: Simulation snapshots and corresponding plots of the DW positions of magnetic DW propagating through a permalloy nanowire ($t = 10$ nm, $w = 100$ nm) under external field at different regimes: (a) steady propagation under 1 mT, (b) oscillating propagation under 10 mT and (c) turbulent regime under 20 mT

When the external magnetic field reaches a certain threshold called the Walker breakdown, the domain wall behavior changes drastically [46]. Domain walls transform under the field, transverse walls generate a vortex core at the apex and turn into vortex walls. The core moves towards the opposite wire side and is expelled. The domain wall propagation direction and displacement show clear oscillations, and the velocity drops dramatically (Figure 1.7 b). At even higher fields, the oscillations' regularity gradually disappears, and the domain wall velocity increases again. In such a turbulent regime, domain walls can even exhibit a double domain wall structure and a complex linear velocity dependence on the external magnetic field (Figure 1.7 c).

An important feature of the above simulations is the assumption of perfect edges for the soft ferromagnetic wires. In real samples, processing defects are inevitable, and a random edge roughness may be introduced into simulations to account for this. Under these conditions, a certain minimum field is necessary to initiate domain wall movement along the wire to overcome edge pinning (propagation field). Another striking consequence of edge roughness is the disturbance of the domain wall spin transformation and a shift of the Walker breakdown towards higher fields.

1.6 Domain wall propagation in real soft magnetic wires

The movement of magnetic domain walls (DWs) through nanowires is influenced by external magnetic fields and the structure of the wire. Studies have observed steady, oscillating and turbulent regimes of DW propagation [47] and have found them to be in agreement with the theory of Schryer and Walker [46]. However, there are still some phenomena that require further explanation.

In real wires, a threshold magnetic field is needed to initiate DW displacement, known as propagation or depinning field (Figure 1.8 a) [48]. This is because the energy of a DW is related to its size [43], and the presence of notches and antinotches in the wire can serve as pinning centers. Researchers have been investigating the pinning and depinning

mechanisms of DWs based on the magnetic wire structure [49, 50, 51, 52], the DW structure [53, 54], and the pinning situation [53, 55].

The force required to move a magnetic DW against its pinning potential is determined by the derivative of the DW energy with respect to the DW position. This derivative is proportional to the slope of the artificial neck (Figure 1.8 b) in a simple model for an isolated notch defect. As a result, different depinning fields are expected depending on the direction of DW propagation in case of asymmetric notches. This discrepancy in depinning fields between rightward and leftward propagation leads to unidirectional motion of the DW under ac field drive, a phenomenon known as the ratchet effect in magnetic DW motion [56].

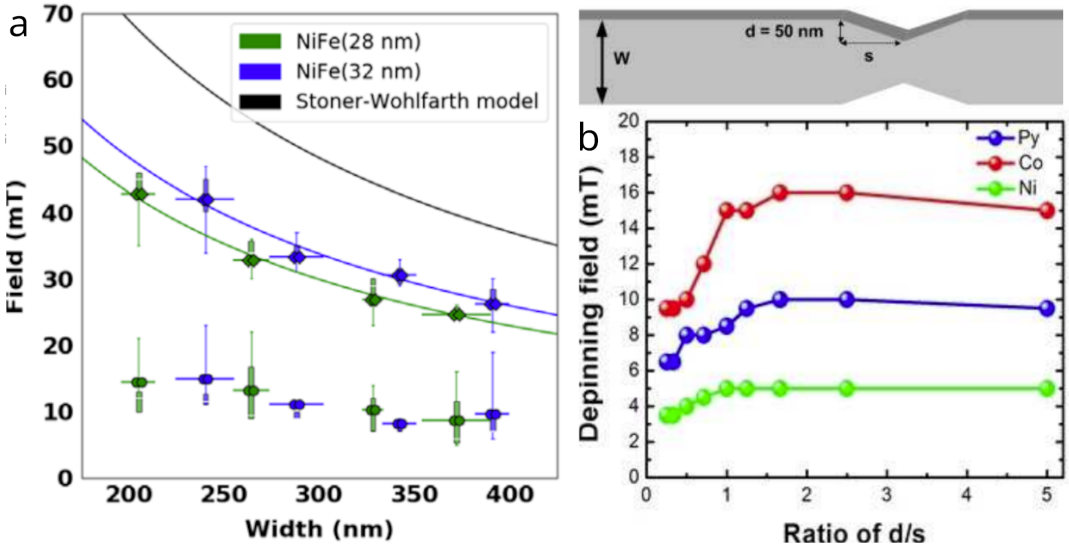

Figure 1.8: (a) Propagation (lower array of dots) and nucleation (upper array) fields of magnetic DWs in permalloy nanowires [48] and (b) sketch of a magnetic nanowire with a notch and DW depinning fields plotted vs. the notch slope [52]

The pinning probability of a DW also depends on its spin structure. Studies have shown that triangular notches in the wire can have a higher pinning probability for clockwise rotating than for anticlockwise rotating DWs [57]. This effect can be used for DW chirality filters. Similar results have been observed for DW propagation through wire branchings [58].

There are two types of depinning fields: static and kinetic. The static depinning field is the minimum field needed to displace a DW from its initial, energetically favorable position. Kinetic depinning in turn is the minimum field required for a moving DW to avoid getting

pinned at a pinning center. The values of these depinning fields are typically larger for static depinning and depend on the wire geometry (Figure 1.9 a) [53].

When thermal fluctuations occur in real wires, they can cause DW motion to occur very slowly just below the depinning threshold. This type of motion is referred to as the 'creep regime' and involves the DW moving between pinning positions by making small jumps [59, 60].

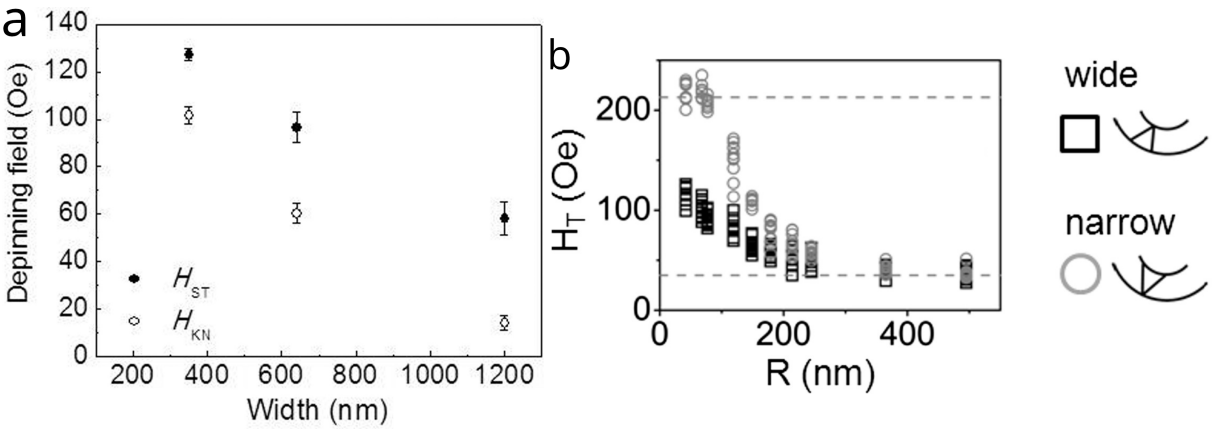

Figure 1.9: (a) Static and dynamic depinning fields with respect to the nanowire width in 20 nm-thick Py wires [53] and (b) transmission field measurements for wide (squares) and narrow (circles) configurations as a function of the curvature radius of the Py wire ($t = 10$ nm, $w = 100$ nm) presented in the sketch [61], "wide" and "narrow" describe the transverse DW orientation in the wire

DW devices can also take the form of curved shapes and this can have a distinct effect on DW propagation. Experimentally it is observed that bends can act as potential wells or barriers depending on the DW chirality [53]. Curvature has an effect on pinning field and the pinning field increases with decreasing radius of curvature. This effect can be explained by two types of pinning. First, geometrical pinning caused by deviation of the strip from the field direction. Second intrinsic pinning caused by a change in the potential landscape seen by a DW when the curvature changes (Figure 1.9 b). Studies with micromagnetic simulations have shown that both exchange and demagnetizing energies play an important role [61].

Finally, at sufficient external magnetic fields new domain walls are generated in magnetic wires. For an infinitely long wire, the nucleation field H_n is determined by the thickness t and width w of the sample as well as the saturation magnetization M_s of the material, and is given by the formula: $H_n = \frac{1}{2} M_s \frac{t}{t+w}$. However, wire irregularities can lower the nuc-

leation field as seen from inhomogeneous spin configurations in simulation results (Figure 1.8). Additionally, thermal activation can also have an impact that is not considered in the Stoner-Wohlfarth model. To account for these effects in the simplest manner, a scaling factor is included in the demagnetization factor [48].

Chapter 2

Materials and Methods

In this chapter, an overview of the magnetoresistance phenomena in thin films of soft magnetic materials and their applications in magnetic sensing is provided. Permalloy thin films serve as a representative example of this material class. Special attention is given to the technique of magnetron sputtering for depositing permalloy films and fine-tuning their magnetic properties, e. g., anisotropy and coercivity. The use of X-ray reflectivity as a quick and reliable method for controlling film thicknesses is discussed.

Additionally, the process of patterning structures in these films is described, which generally involves two stages: patterning using electron-beam lithography and depositing metal layers using magnetron sputtering, or alternatively, using ion beam etching on a pre-grown thin films. The use of Kerr microscopy and vibrating sample magnetometry to evaluate the magnetic properties (coercivity and anisotropy) of samples is also discussed. The experimental setup for generating short Ørsted-field pulses to displace domain walls in permalloy nanowires is described, along with its use in combination with a Kerr microscope to observe changes in the nanowires' domain pattern. Lastly, a brief explanation of the Mumax3 micromagnetic simulation program and the used parameters is provided.

2.1 Magnetic sensors and magnetoresistance phenomena

Magnetic sensors, which rely on the magnetic effects to function, are widely used in today's world [62, 63, 64]. One of the main advantages of these sensors is that they are durable, reliable, and require little to no maintenance, compared to other types of sensors. In particular, magnetic position sensors are cost-effective and sturdy, able to operate in harsh environments, such as those with oil present, where other sensors would fail. The magnetic proximity switch is one of the most commonly used sensor types worldwide [62]. Many magnetic sensors utilize soft magnetic materials, such as crystalline, amorphous, and nanocrystalline magnetically soft alloys, for applications in anisotropic magnetoresistance (AMR) [65] and giant magnetoresistance (GMR) [66] sensors. These materials must have high maximum saturation magnetization, low coercivity, constant or high permeability with minimal temperature dependence, and high electrical resistivity [63].
Anisotropy, a measure of the material's magnetic directionality, is typically averaged out in polycrystalline materials. However, induced and shape anisotropies, which can impact sensor performance, may be present. These anisotropies can be induced by applying a magnetic field during the material's deposition or through subsequent annealing in fields. This induced anisotropy is often exploited in AMR sensors, creating a single domain within the sensor volume and allowing for rotational magnetization switching rather than domain wall movement [62].

2.1.1 Resistivity of thin films

The primary reason for resistance in pure metals at standard temperatures is the obstruction of conduction electrons by phonons, i. e., vibrations in the lattice structure. As films become thinner, their resistivity increases; a phenomenon referred to as the size effect [14]. Fuchs was the first to explain and model the resistivity caused by obstruction at the top

and bottom surfaces of thin films [67]. Later, Sondheimer expanded on Fuchs' work to include narrow metal lines [68]. Together, their theory of surface obstruction is known as the Fuchs-Sondheimer (FS) model. However, many researchers have taken issue with Fuchs' assumption of constant specularity for electron-interface interactions, as it ignores the electron wavelength, the incident angle, and the interface roughness.

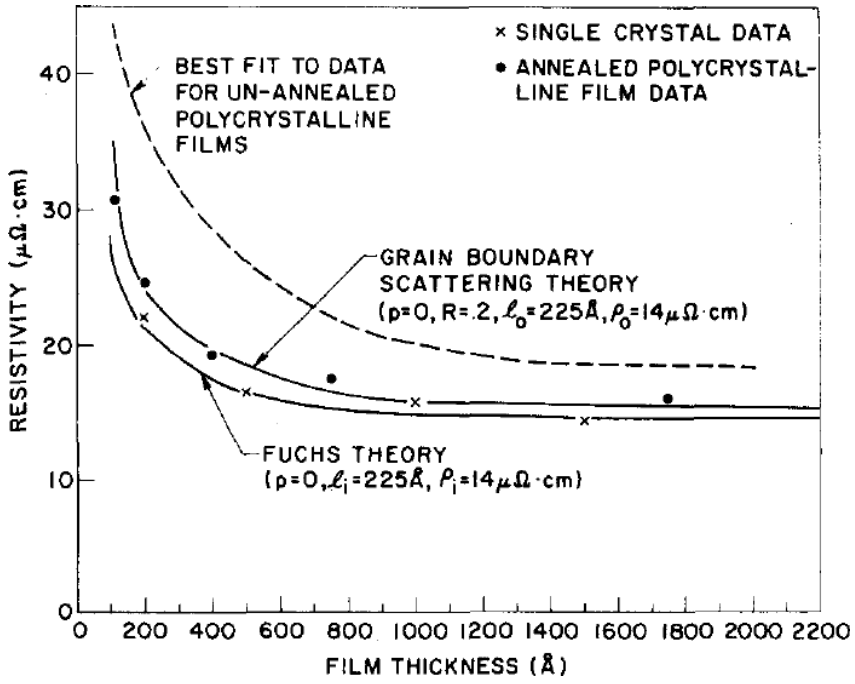

Figure 2.1: Resistivity of permalloy films with different thicknesses [69]

Mayadas and Shatzkes observed that the size effect on the resistance was more pronounced in polycrystalline conductors compared to single crystals [70] (Figure 2.1). They developed the Mayadas-Shatzkes (MS) model to explain this additional resistance size effect in terms of grain boundary scattering. When the grain size of a polycrystalline conductor is on the same order of magnitude as the conductor's electron mean free path, the conduction electrons can be obstructed by the grain boundaries that separate the individual crystallites. The MS model considers all interactions of conduction electrons with a grain boundary as either a reflection with a random momentum direction, a loss of energy, and a probability R, or a transmission with no change in momentum and a probability $1-R$. The transmitted electrons maintain their electric-field-induced momentum, and do not contribute to the resistance size effect. The reflected electrons lose their field-induced momentum and contribute to a size-effect resistance increase when the grain size of the conductor is

reduced.

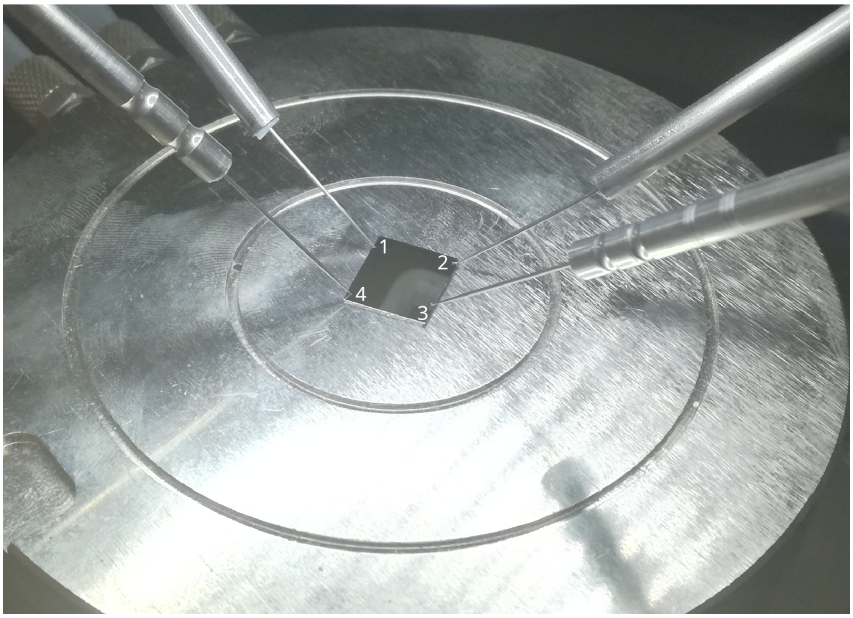

Figure 2.2: Sheet resistance measurement of a square sample in the van der Pauw geometry

For optimizing permalloy deposition conditions thin films sputtered under different conditions were investigated including their sheet resistance. The resistivity of the thin films was determined using the van der Pauw technique commonly used for quasi-2D materials ($t \ll w$) [71, 72]. Four electrodes were positioned at the corners of a square-shaped sample (Figure 2.2), allowing for the calculation of the average sheet resistance R_s of the sample:

$$e^{\frac{-\pi R_{12,34}}{R_s}} + e^{\frac{-\pi R_{23,41}}{R_s}} = 1,$$

where $R_{12,34}$ and $R_{23,41}$ are the resistances measured through the voltage drop along one side of the sample (3-4 and 4-1) with current applied along the opposite side (1-2 and 2-3 correspondingly).

2.1.2 Anisotropic magnetoresistance and planar Hall effect

Anisotropic magnetoresistance (AMR) sensors have a wide range of industrial applications, such as in vehicle detection, contactless measurement of electrical currents, measurement of position and rotational speed in machinery, and low-end electronic compasses [62]. Recently, it was discovered that AMR sensors can have ultra-sensitive detection capabilities for small magnetic fields, down to the 1 nT range [73]. The AMR effect is based on the property that some ferromagnetic materials have a dependence of their resistivity on the angle between the direction of the current flow and the direction of their magnetization. This effect was first discovered by William Thomson in 1856 in some ferromagnetic samples, such as iron and nickel, with a change in resistance of about 5% in an applied field of several T [74]. The microscopic theory of this dependence is based on the larger probability of $s-d$ scattering for electrons traveling parallel to the magnetization. As a result, the resistivity has its maximum value for a current flowing along the direction of magnetization and its minimum value for a current flow in a perpendicular direction [75, 76].

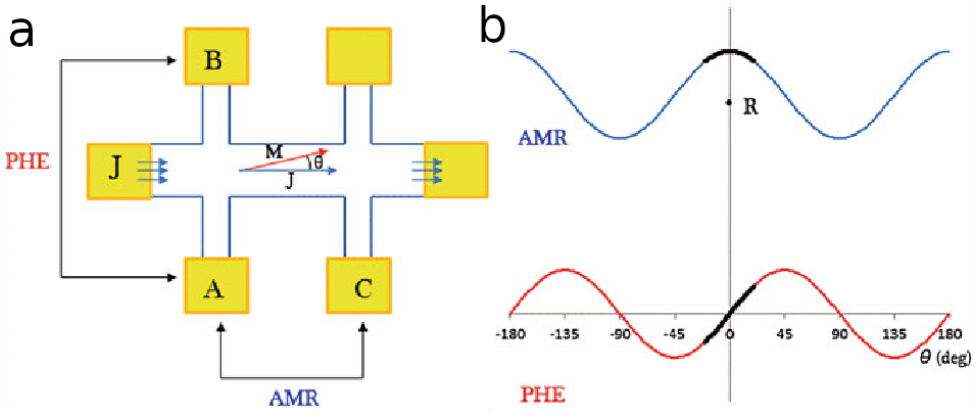

Figure 2.3: (a) A diagram of a common design used to measure AMR and PHE and (b) the corresponding relationship of resistance to the angle between the current and magnetization [77]

The planar Hall effect (PHE) is closely related to the anisotropic magnetoresistance (AMR) [77]. For polycrystalline ferromagnetic $3d$ alloys the dependence is given by the equations:

$$\rho_{xx} = \rho_{\perp} + (\rho_{\parallel} - \rho_{\perp})cos^2\theta$$

$$\rho_{xy} = \frac{1}{2}(\rho_{\parallel} - \rho_{\perp})sin\theta.$$

The variation of resistance along the x-axis ρ_{xx} is called the anisotropic magnetoresistance (AMR), while the variation of resistance along y-axis ρ_{xy} is called the planar Hall effect (PHE), where $\rho_{\perp}$ is the low-resistance magnetization state with magnetization direction perpendicular to the electrical current, and $\rho_{\parallel}$ is the high-resistance magnetization state with magnetization direction parallel to the electrical current. The AMR is a function of the angle between the current and the magnetization and has its largest slope at $\frac{\pi}{4} \pm \frac{n\pi}{2}$ whereas the PHE has its largest slope at $\frac{n\pi}{2}$ (Figure 2.3). Additionally, the AMR signal is measured on top of a DC component associated with the average resistance, therefore temperature and aging drifts affecting the DC component can be detrimental for the AMR sensors.

A 4 nm $Ni_{47}Cr_{42}Fe_{11}$ seed layer improves the (111) texture of permalloy films and thus was employed to enhance the AMR [78]. The AMR of the samples under examination was determined using Hall bars [72].

2.1.3 Giant magnetoresistance

In 1988, it was discovered that single crystalline Fe/Cr/Fe sandwiches and Fe/Cr multilayers displayed much larger magnetoresistance values than could be explained by the magnetoresistance of the individual Fe layers alone [3, 79]. The resistance of these multilayers decreased by nearly a factor of two when a 2 T field was applied at low temperatures. This phenomenon was named giant magnetoresistance (GMR) [80].

Theoretical explanations of the GMR effect are based on Mott's model of electrical conduction in ferromagnetic metals [81]. In these materials, electrical current is carried independently in two conduction channels, corresponding mainly to spin-up and spin-down $s-p$ electrons with low effective masses. The scattering rates of these these conduction electrons are related to corresponding spin-up and spin-down empty states, that are largely of d-character and, as a result of the exchange-split d-bands, the ratio of spin-up to spin-down density of empty states at the Fermi level can be significantly different in

the ferromagnetically ordered states of Fe, Ni, Co, and their alloys. This leads to the possibility of substantially different mean free paths and conductivities in the two channels, resulting in the GMR effect.

2.1.4 Multiturn rotation counter

There have been several sensor concepts developed and discussed in the literature that utilize domain walls (DWs) [9, 82, 83]. The first to be commercialized was created by Novotechnik [84]. This sensor uses the GMR effect to count the number of rotations of a magnetic field. Information on the absolute rotation is stored by identifying the positions and number of DWs within the device. The sensor is made up of a soft magnetic wire formed into a spiral shape with several concentric loops, and it has a nucleation pad on one end. It is operated by rotating an external field. When the sensor undergoes a 180° rotation under an applied field, a new DW is generated in the nucleation pad and follows the applied field's projection, moving towards the tapered end or back to the nucleation pad, where it is eliminated (Figure 2.4 a). The DWs in the device are stable and can be stored without power until the readout, which is performed using the GMR effect. The resistance of areas of the sensor with parallel or antiparallel orientations with regard to the fixed layer of the GMR stack is different, enabling the detection of the number of DWs and thus the number of rotations. Magnetic DW-based sensors have many advantages over other technologies, one of the most notable being their stability well above room temperature, making them potential candidates for nonvolatile sensing.

One major drawback of multiturn sensors is their small and limited number of turns counted. When the maximum number of rotations is reached, its $n+1$ state is equivalent to the n-one. Commercially available counters have a maximum number of 46 rotations [85], but many industrial applications require a larger number of counts. A different approach has been proposed, using closed loops with varying numbers of cusps, which are directed towards the center of the loop [86] (Figure 2.4 c). However, an issue inherent to this cusp geometry is the increased width at the position of two merging nanowires. The wider area

serves as a nucleation site and reduces the nucleation field.

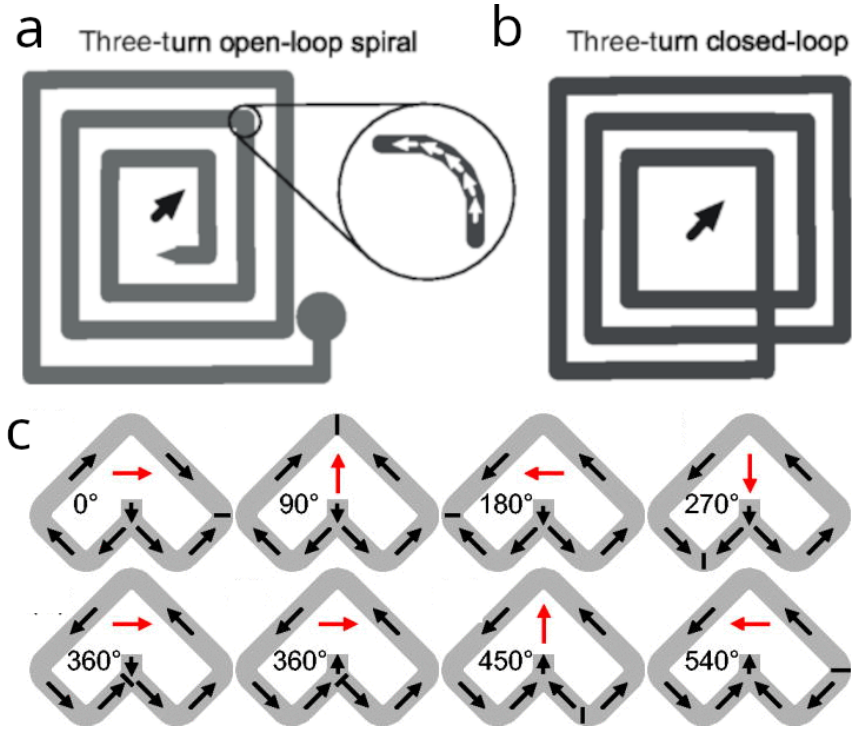

Figure 2.4: The multiturn counter is represented in (a), while ideas for a closed loop sensor and closed loops with cusps are presented in (b) and (c), respectively [10, 86]

More recently, a concept of a closed-loop sensor was suggested, which resets back to zero after reaching a maximum number of turns [10] (Figure 2.4 b). By using several closed-loop sensors with mutually prime numbers, it is possible to count to much larger numbers. However, the closed-loop concept has an intersection region and the DW propagation through it is crucial for the device performance. Stochastic DW pinning, nucleation or propagation reversal can lead to sensor failure, which can be avoided by thoroughly controlling either the DW spin structure by suppressing the Walker breakdown or the angle of the applied magnetic field (e. g. by introducing syphons [10]), moving the DW through the intersection. Therefore, more sophisticated device geometries than the one shown in the figure are needed for reliable device operation, robustness, and fault tolerance [10].

2.2 Permalloy thin films

Soft magnetic materials typically possess a low coercivity, a small degree of magnetocrystalline anisotropy, a significant saturation magnetization, and often minimal or no magnetostriction [14]. This last feature is important in applications that involve an alternating current, as magnetostriction can cause the conversion of field energy into mechanical energy, resulting in losses. Soft magnetic thin films are frequently made from the ferromagnetic elements found in the 3d transition metals, such as Fe, Co, and Ni, and their various alloys.

The $Ni_xFe_{(1-x)}$ alloy is a classic example of a soft magnetic material. When x is around 0.8, the alloy is known as permalloy, which has highly desirable properties such as high permeability, low coercivity, and near-zero magnetostriction. Permalloy was first discovered by Arnold and Elmen [87]; the early explanation of the low anisotropy of permalloy is based on the fact that pure iron and nickel have cubic crystalline lattices with similar parameters, and the different easy axis directions of magnetocrystalline anisotropy of each metal cancel out in the alloy.

Ferguson's study examined the anisotropy of permalloy as a function of the Ni content (Figure 2.5) [88]. He attributed the decrease in anisotropy to the magnetic ordering of iron pairs in the nickel matrix. However, there is a significant amount of scatter in the data, indicating that other sources of anisotropy may also be present. The ideal composition for permalloy, in terms of high permeability and near zero magnetostriction, is $Ni_{81}Fe_{19}$.

Thin films of permalloy were first reported in the 1950s by researchers such as Blois [90], Tannenwald and Seavey [91], and Smith [92]. Due to its attractive properties, permalloy thin films have been widely used in a variety of research and devices. Its soft magnetic properties have made it useful in many different types of devices, even if the final product uses a different, more optimized material. Permalloy is often used as a starting point to demonstrate early proof-of-principle devices and prototypes.

There are several types of anisotropy observed in thin permalloy films, including interfacial, shape, magnetocrystalline, induced, and stress anisotropy. The magnetocrystalline

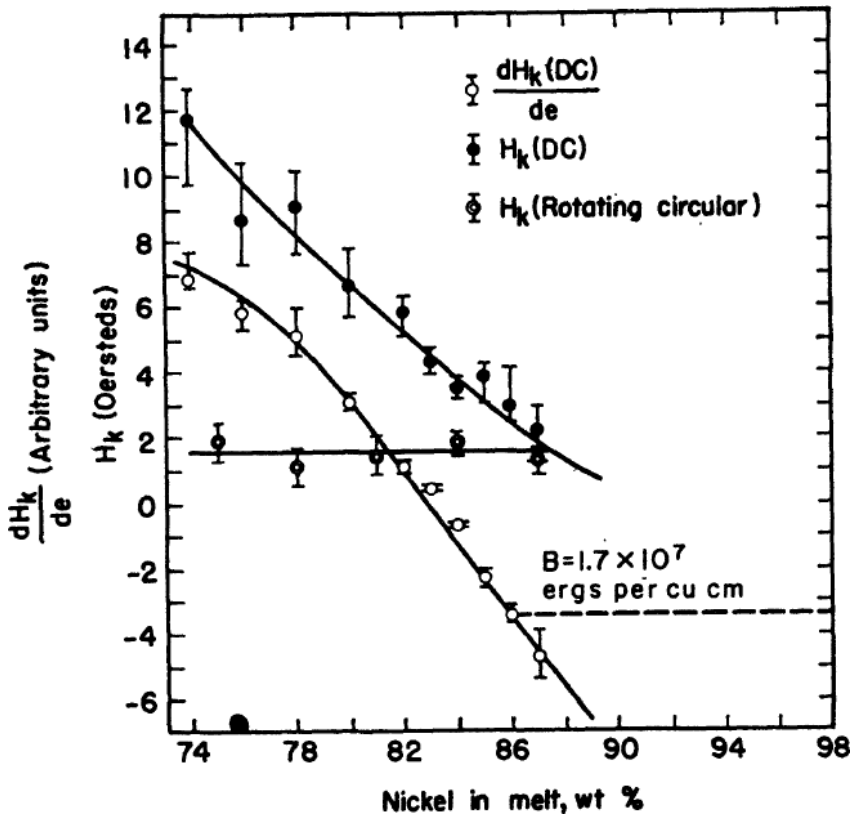

Figure 2.5: Anisotropy field H_k and isotropic magnetoelastic constant $\frac{dH_k}{de}$, where e is applied strain, of permalloy films vs. nickel content in melt [89]

anisotropy is intrinsic to the material, while the induced anisotropy is a result of the processes applied during material preparation, such as annealing in a magnetic field. An interfacial anisotropy of structural origin arises due to symmetry breaking at the interface between two materials, as first noted by Néel [20] and later the theory in terms of spin-orbit interaction was developed by Bruno [93].

Magnetocrystalline anisotropy arises from the arrangement of atoms in a crystal structure, where the total electronic wave functions overlap in an anisotropic manner. As a result, magnetic measurements along different crystallographic directions yield different magnetization curves. The main physical origin of the anisotropy is spin-orbit coupling and orbit-lattice coupling, which together result in a preferred set of directions along which the energy of the system is minimized and the magnetization preferentially lies.

The uniaxial anisotropy can be induced or suppressed by various techniques, such as depositing the material in a moderate magnetic field [94, 95, 72, 96] or a tilted geometry [97, 94, 72], or by subjecting it to annealing in a magnetic field [98, 99]. Certain materials including permalloy also have a tendency to self-anneal even in the absence of an external

magnetic field [89]. In some cases, thermal fluctuations in polycrystalline alloys during the deposition may be significant enough to prevent alignment of the magnetization through self-annealing in small particles of the material.

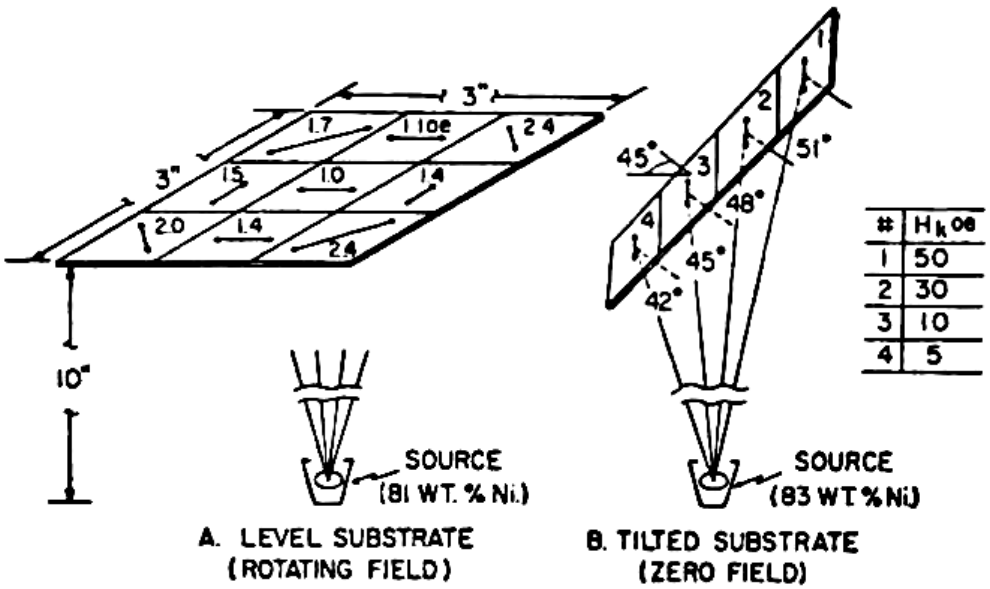

Figure 2.6: Schematic illustration of the permalloy melt (≈1550°C) used as a point source for vacuum deposition and heated glass substrates (200°C) positioned at different angles of incidence. Samples deposited on leveled substrates in a rotating magnetic field (A) exhibit clear rotational symmetry of the easy axes directions, which are perpendicular to the line of incidence from the source. Deposition in zero field on tilted substrates (B) results in defined in-plane easy axes with well-defined anisotropy constants. [89, 94]

The mechanisms responsible for the anisotropy in NiFe films are still a topic of debate among researchers. Different effects such as ordering [100], strain [101, 102], and inhomogeneities of various types (e.g. impurities [103], vacancies [104], grain boundaries [104], phases [105, 106]) have been proposed as potential causes for the induced uniaxial anisotropy observed in permalloy.

Recent studies have demonstrated that ordering is a source of induced anisotropy in permalloy by carefully measuring the resistance of thin permalloy films that were deposited in an external magnetic field [72]. This is because the axes of magnetic anisotropy and anisotropic resistivity are found to align with each other and that they are correlated with the atomic/pair order. Specifically, the alignment of Ni-Fe pairs along the easy axis leads to a lower conduction electron scattering rate, while Ni-Ni and Fe-Fe pairs along the hard axis provide a less uniform medium and higher resistance [107].

It is important to note that a solid solution can exhibit directional order even if it is perfectly random in the usual crystallographic sense. For example, a 50-50 solution would be considered random if the neighbors of any given A atom are on average half A and half B. However, this solution can deviate from randomness in two ways: by exhibiting short-range order, where more than half of the neighbors of an A atom would be B atoms, or by displaying clustering, where more than half of the neighbors would be A atoms. The solid state solution shown in Figure 2.7 does not show any tendencies towards short-range order or clustering, it has 56 unlike-atom pairs and 56 like-atom pairs, but the like-atom pairs are preferentially oriented. The basic hypothesis of directional order creating anisotropy is that there is a magnetic interaction between the axis of like-atom pairs and the direction of the local magnetization, such that the two tend to be parallel [108].

Wilts and Humphrey [104] described a dispersion of uniaxial anisotropy as being difficult to define due to its elusive nature, making any definition mostly operational. Essentially, this refers to a non-uniformity where the direction and magnitude of anisotropy varies from one location to another within the film. The challenge with this concept arises from the fact that all instruments measure the local direction of magnetization, which means that they not only observe the effect of local anisotropy in a specific area but also the influence of the surrounding material due to exchange.

Masuda [109] focused on the temperature variation of the dispersion and discovered that it increased as the temperature increased, whereas magnetocrystalline anisotropy decreased rapidly with temperature. Meanwhile, West and Simmons [110] discovered that the anisotropy dispersion was independent of thickness and unaffected by grain size.

2.3 Magnetron sputtering

Sputtering is a process in which high-energy atomic particles (typically ions) bombard a material, causing individual target atoms to acquire enough energy through collisions to be ejected from the surface. This was first observed by W. R. Grove in 1852 [111], who noticed metallic deposits on glass walls during his research on the electrical conductivity

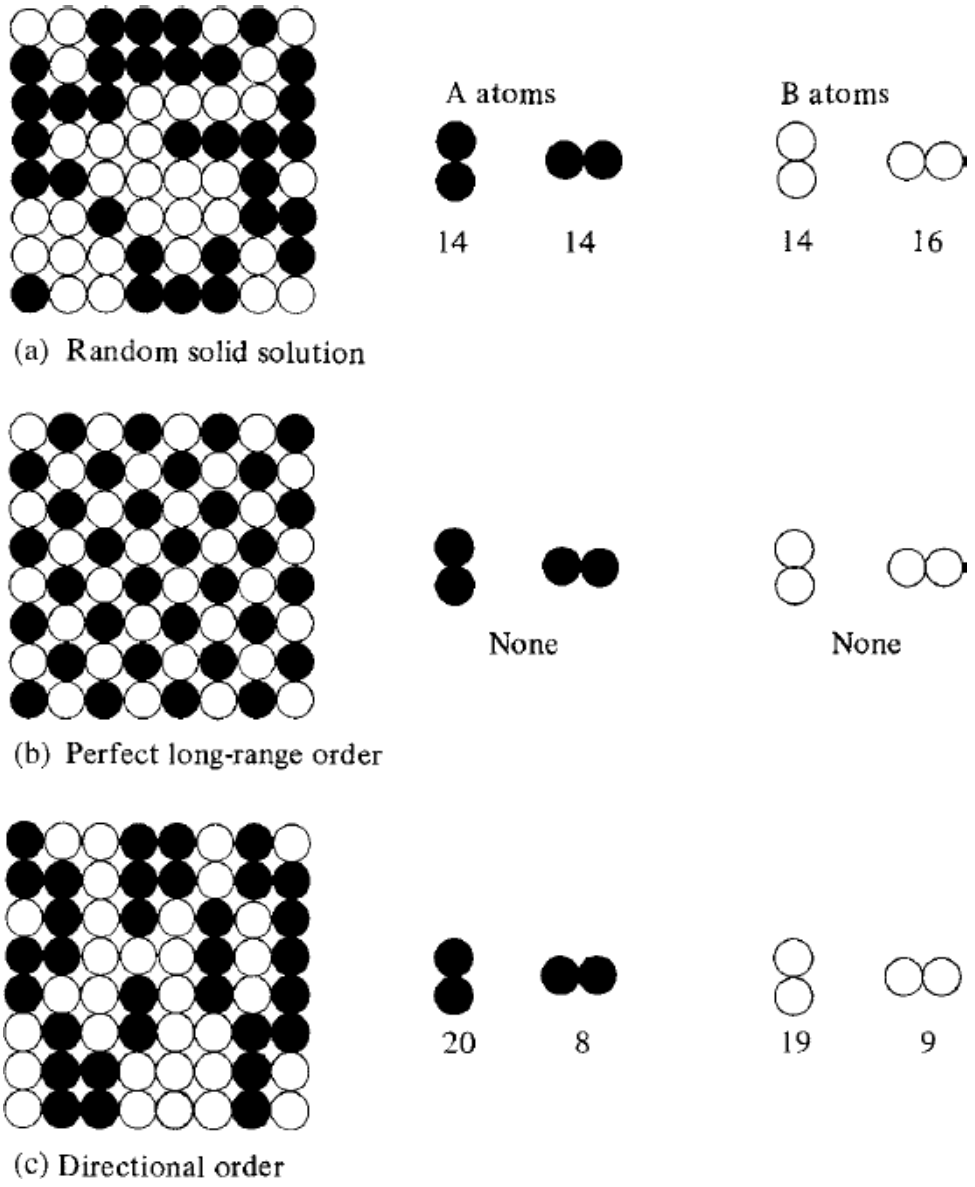

Figure 2.7: Examples of atom arrangements in a square 2D lattice [108]

of gases. Today, it is understood that sputtering is caused by a cascade of atomic collisions in the surface layers of a solid [112]. Sigmund has extensively studied the theory of sputtering and proposed a theoretical formula [113], which has been compared with experimental results [114]. There have been many studies on sputtering, including computer simulations of the emission of clusters by Harrison et al [115, 116]. They suggest that the emission of clusters of two and three atoms are common occurrences in sputtering of copper by argon ions in the energy range from 0.5 to 5.0 keV.

Sputtering sources use magnetrons to confine charged plasma particles near the surface of the sputter target through strong electric and magnetic fields (Figure 2.8). When subjected to a magnetic field, electrons follow a helical path around magnetic field lines, resulting

in an increased number of ionizing collisions with gaseous neutrals near the target surface. The sputtered atoms are neutral, making them unaffected by the magnetic trap [117].

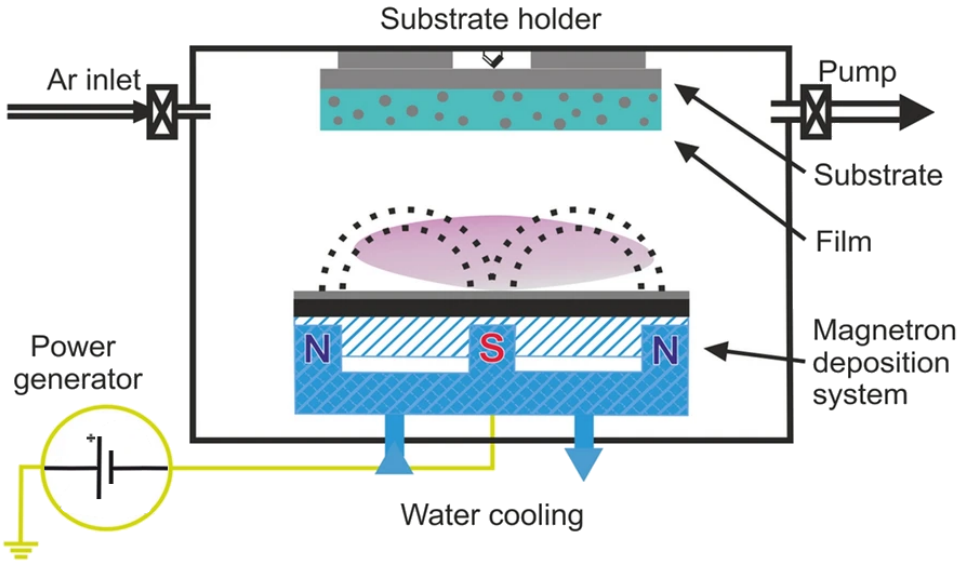

Figure 2.8: Schematic illustration of the magnetron sputtering process [118]

The atoms that are ejected from a surface through sputtering can be utilized to deposit a coating on a substrate. Sputtering has unique advantages as a method of deposition, such as high deposition rates with simple thickness control (which is not the case for e. g. electrolysis deposition), the ability to sputter complex materials while maintaining stoichiometry and co-sputtering, the ability to use sample preparation techniques like etching and annealing, and the ability to deposit in variable magnetic fields and temperature ranges [119]. Due to its scalability and reproducibility, sputtering is a suitable method for industrial applications. The samples investigated in this project are prepared using the Singulus Rotaris Universal Sputtering System [120], which is intended for commercial use and features 18 target slots in 2 chambers, in-situ annealing up to 550°C, and etching using a plasma etching source. The system is designed for deposition on 200 mm diameter silicon wafers and provides high uniformity of deposition by rotating the wafer at up to 60 rpm during deposition. Sputtering of the samples investigated in this thesis was carried out at room temperature in a ultra-high-vacuum vacuum chamber with a base pressure of less than 10^9 mbar using 10 cm diameter high-purity material targets provided by Singulus. The deposition tilt was 14° with respect to the substrate normal and the target to substrate distance was 20 cm (Figure 2.9). During deposition the sample stage was

rotated around its axis at 1 rpm to provide uniformly thick films, to remove the influence of static background magnetic fields such as the Earth's and the stray field of the cathode magnets, as well as to avoid self-shadowing [121].

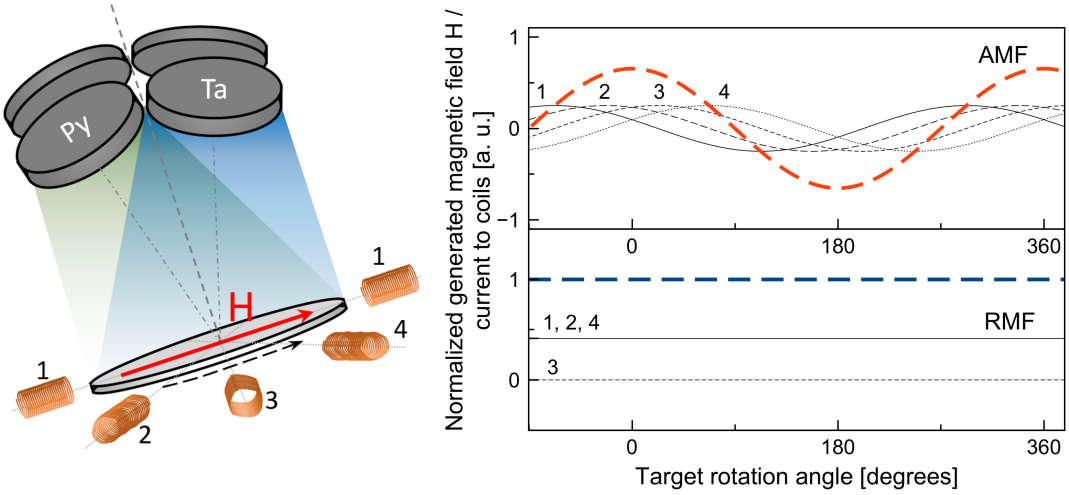

Figure 2.9: Schematic illustration of the deposition geometry in the Singulus Rotaris sputtering chamber that is used for the permalloy thin film deposition. The sample is placed on a rotating holder and four pairs of coils (1-4) are fixed in space in the plane of the holder to generate a mostly homogeneous magnetic field that is either static and thus rotating in the reference frame of the sample (RMF) or synchronized with the sample's rotation and thus constant (aligning) in the frame of the sample (AMF).

It has been observed that the chemical composition of a film deposited through sputtering an alloy target is very similar to that of the target. This indicates that sputtering is not controlled by thermal processes, but rather by a momentum transfer process. Various alloys are commonly sputtered, including permalloy. Flur and Riseman found that films sputtered from a permalloy target had the same composition (within ±0.3% instrumental error) as the target [122].

The structure of the film produced by sputtering is crucial to its physical properties. Permalloy films on oxidized silicon grow in Volmer-Weber mode [123, 124], in which adatoms are more strongly bound to each other than to the substrate. Volmer-Weber growth mode is observed when metals are deposited on insulating substrates, graphite, alkali halides, and mica, among others [125]. Film growth begins with randomly oriented nuclei. Surface energy minimization leads to the development of a <111>-fiber texture in *fcc* metals, where crystals tend to have crystallographic orientations with (111) planes parallel to the film [14]. The nucleation and growth of spatially isolated crystallites are associated

with intrinsic compressive stress due to surface stress. Research has shown that tensile stresses develop in a growing film when the crystallites begin to coalesce because as soon as they touch, they tend to minimize surface energy [14]. Stress affects the magnetic properties of permalloy [89, 126, 127]. For Permalloy, which has high adatom mobility, arriving atoms diffuse into grain boundaries and gradually relax tensile stress with increasing film thickness (Figure 2.10). Studies have shown that compressive stresses in sputtered films depend strongly on the atomic mass of the target material, the argon sputtering pressure, and other factors. A simple analysis of the energies and momenta of the argon ions (atoms) and the atoms in the target material helps to explain why the atomic mass of the target material correlates so strongly with compressive stresses in the deposited film [14].

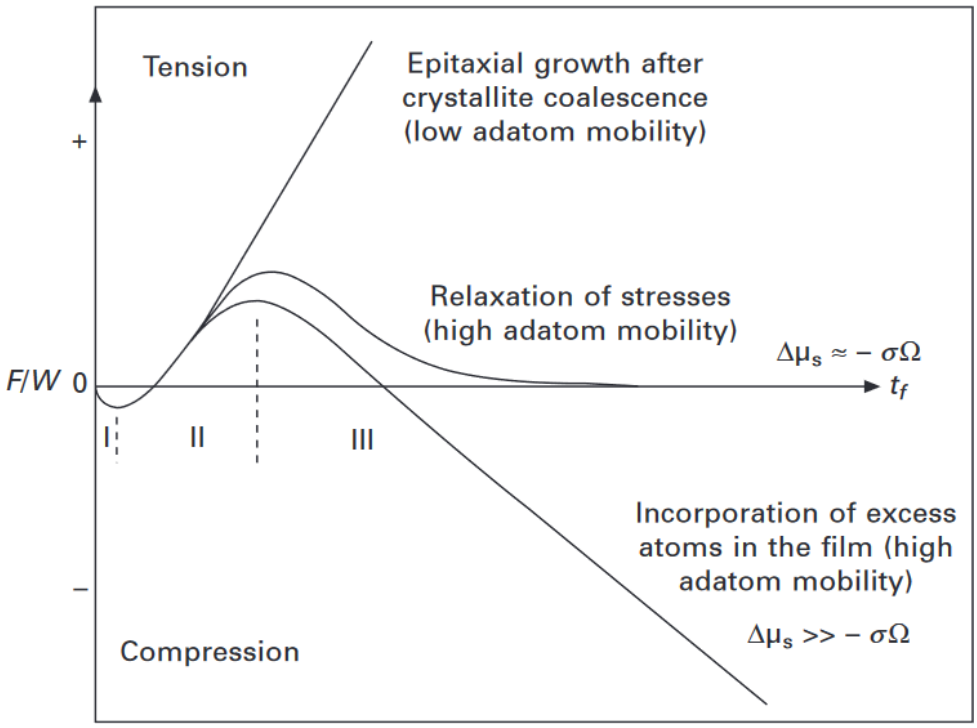

Figure 2.10: The force (per unit length) exerted on a substrate by a growing film as it thickens, highlighting the different behaviors observed for different adatom mobilities [14]

The properties of films deposited through sputtering are connected to the conditions under which they were deposited through the material microscopic structure (grain size distribution, density, roughnes, stress, etc.). In 1969, Movchan and Demchishin proposed the first structure zone model (SZM) for evaporated coatings as a function of temperature [128], and in 1973, the model was extended to magnetron sputtering [129] (Figure 2.11). The SZM illustrates how the structure of metal film deposited by magnetron sputtering is

affected by the homologous substrate temperature (the substrate temperature T relative to the melting point T_m of the coating material) and Ar discharge-gas pressure.

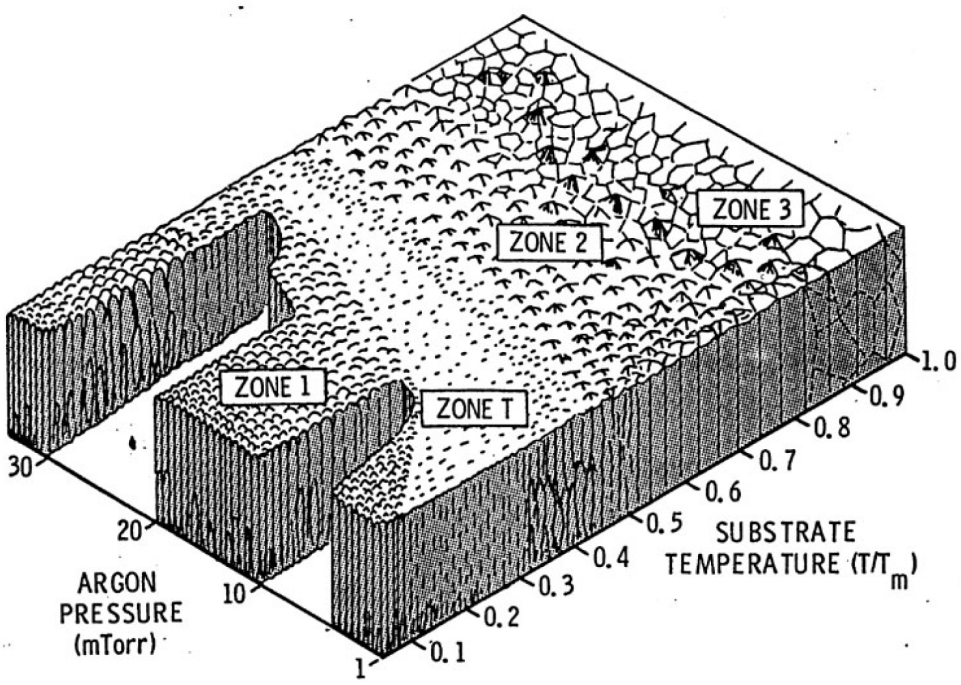

Figure 2.11: The structure zone model describes how the substrate temperature (relative to the melting point of the coating material T_m) and the argon pressure affect the structure of metal films deposited by magnetron sputtering [129]

In Zone 1, the film texture is an open-voided tapered fibrous structure, which results from the low-angle oblique incidence of thermalized particles and the limited diffusion of adatoms on the substrate surface. The former is caused by collisions between sputtered particles and discharge-gas particles during transportation, which is inherent in the sputter-deposition process, while the latter is caused by the low substrate temperature. Deposition under oblique incidence was shown to induce anisotropy in Py [121].

In the transition Zone T, the film texture shifts to wider columns with flat surfaces. This is due to the further advancement of thermally enhanced surface diffusion caused by an increase in substrate temperature from energetic particle bombardment. The Zone T structure forms as a result of the interaction between thermally enhanced surface diffusion and bombardment of energetic particles. The promoted diffusion fills the gaps between columns and the bombardment makes the column surfaces flat. However, surface and bulk diffusion are still limited due to the relatively low substrate temperature, resulting in an amorphous crystallographic structure in the columns.

In Zone 2, thermal surface and grain-boundary adatom diffusion increase with an increase in substrate temperature, which in turn, widens the columns and reduces the gaps between columns further. Enhanced surface diffusion, in comparison to reconstruction by energetic-particle bombardment, significantly promotes crystallographic growth in the columns, resulting in higher crystallinity. In Zone 3, enhanced bulk and boundary adatom diffusion dominate the formation of film texture and internal structure. As a result, the gaps between column boundaries narrow and internal thermal crystallization of the columns occurs, resulting in near-equiaxed and highly crystallized internal structures [130].

Target erosion, also known as target consumption, during magnetron sputtering alters the shape of the target [131] and can affect the deposition rates [131]. It has been reported that local heating and preferential sputtering cause changes in the crystallographic and magnetic texture of the target, which affects the emission trajectories and can affect the intrinsic stress in the deposited permalloy films and thus their magnetic properties [131]. Figure 2.12 illustrates an example of sputter-target consumption [132]: a new Ni target (a) and the same target worn out after multiple magnetron sputtering cycles (b).

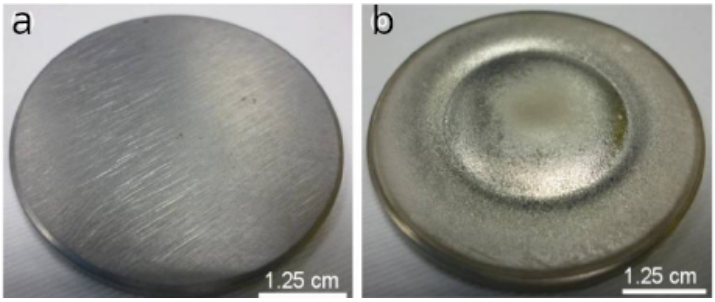

Figure 2.12: (a) A new Ni target and (b) the same target after multiple magnetron sputtering cycles, from [132]

Additionally, the magnetic properties of sputtered permalloy can be modified by the composition of the material stack. Capping layers, like Ta, Cu and Ru, that provide oxidation protection were found to cause intermixing between layers, resulting in magnetically "dead" layers [133, 134, 14]. A 4 nm Ta capping layer was deposited on the samples under investigation in order to safeguard the permalloy from oxidation while still providing reliable resistivity measurements due to the low electrical conductivity of tantalum.

A specially designed highly conductive material stack composed of alternating CuN and Ta layers developed by Daniel Schönke [135] was used for the field-generating Ørsted lines (Ta(4 nm)[CuN(16 nm)Ta(4 nm)]×6). It warrants a low surface roughness that is important to minimize pinning effects in Py deposited on top of the line.

2.4 Control of the thin-film quality

Investigating the thickness-dependent magnetic properties of permalloy films requires high standards for the uniformity of the sputtered film thicknesses in order to obtain reliable results. In this study, all permalloy films were prepared by *Fabian Kammerbauer* and *Maria Andromachi Syskaki*. Before each deposition, the thickness was calibrated using two test samples, resulting in an outstanding reproducibility of the deposited samples within a ±2Å variation (0.7%).

The resulting film parameters were investigated in terms of thickness, grain size distribution, and roughness. These parameters were extracted from X-ray reflectivity, diffraction, and atomic force microscopy measurements.

2.4.1 X-ray reflectivity

X-rays that are reflected off a surface at a very shallow angle penetrate very little into the medium. This makes them useful for analyzing the structure of the surface [136]. When X-rays hit a surface, they will be refracted, reflected, and scattered in different ways depending on the refractive index of the material they are interacting with. The interference between X-rays that are reflected off the top surface of the medium and those that are reflected off the bottom surface results in oscillations, known as Kiessig fringes [137]. These oscillations can be used to determine the thickness of the films [138]. Multilayered systems can be analyzed with the help of a model called Parratt's multilayer model [136], which can be implemented using the open-source program GenX [139]. The XRR measurements

were conducted using a Bruker D8 diffractometer, which is particularly well suited for the investigation of thin films. The source-side and detector slits were set to 0.3 mm, the rotary absorber was in automatic mode, and the scan was recorded in the range of 0.3 to 10° with a step size of 0.02° with 0.5 s dwell time. An example of an analyzed reflectogram is presented in Figure 2.13.

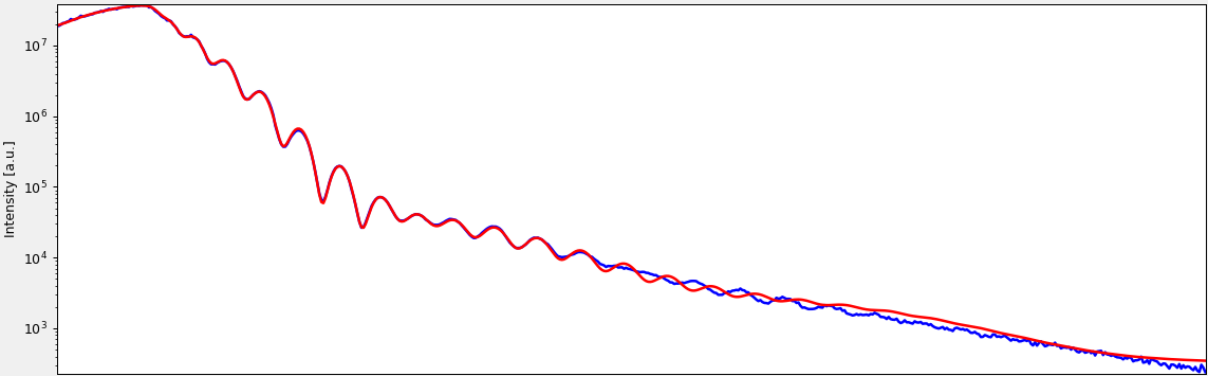

Figure 2.13: The XRR reflectogram (shown in red) of a thin permalloy film with 4 nm NiCrFe seed layer and 4 nm Ta capping sputtered on a thermally oxidized (100 nm) silicon wafer and analyzed using GenX [139] (model shown in blue). The extracted parameters include a permalloy thickness t=29.8±0.2 nm, a Py density d=8.70±0.08 g/cm^3 and a surface roughness σ=0.90±0.05 nm.

2.4.2 Atomic force microscopy

In 1981, Binnig and Rohrer created the scanning tunneling microscope, which is capable of imaging surfaces at the atomic level by utilizing quantum tunneling of electrons between a sharp tip and a conducting surface [140]. Shortly after, the concept of atomic force microscopy was proposed as a method for investigating insulating materials by measuring forces [141]. In order to detect atomic-scale surface topography, a sharp tip is mounted on the end of a soft cantilever spring. The system includes a mechanical raster-scanning mechanism (typically piezoelectric), a method to detect the cantilever deflection (typically interferometry), a feedback system to regulate and monitor the cantilever force, and a display to convert the force-position data into an image. In the contact AFM mode, also known as the repulsive mode, the tip physically touches the surface and repulsive forces

are generated [142].

The AFM measurements were performed using Digital Instruments Veeco Dimension 3100 SPM/AFM microscope with SNL-10 high-resolution tips. The image analysis was performed using the open-source Gwyddion software [143]. The root-mean-square roughness of thin film samples was extracted from 5×5 μm^2 AFM scans. An example of an AFM images and the grain size analysis is presented in Figure 2.14.

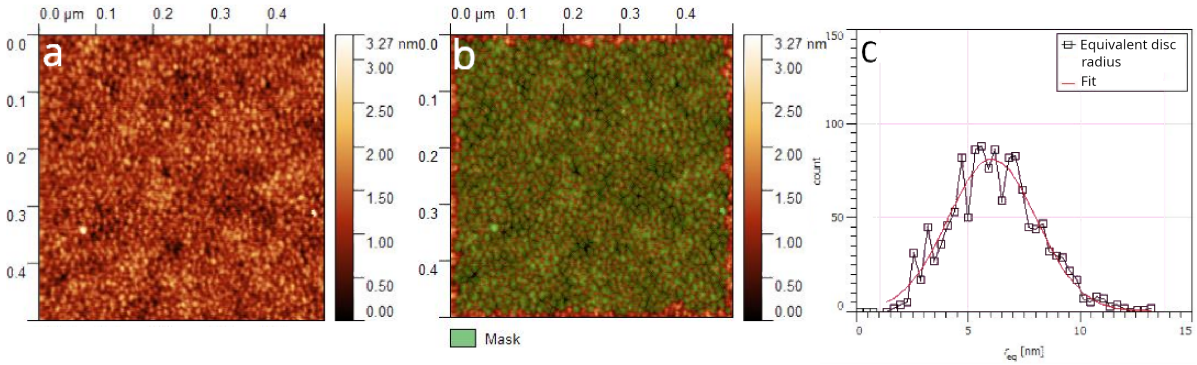

Figure 2.14: AFM results: (a) 500×500 nm^2 AFM image, (b) Gwyddion software [143] threshold mask, and (c) grain size distribution analysis, average grain size $\varnothing_{av}$=12.1±0.2 nm and surface roughness RMS=0.24 nm.

XRR and AFM provide a complementary approach to characterizing sample roughness, but the results obtained by these two techniques are often not consistent. Both techniques have different capabilities in terms of measuring the power spectral density [144]. The AFM measurement has a limit on the high spatial frequency information due to the size of the tip, resulting in a smoother surface appearance. However, the longest spatial wavelength on the surface that can be measured by AFM is limited by the maximum scan range. Additionally, XRR can examine buried interfaces, while AFM can only analyze the top surface. The uniformity of the sample is also a factor to consider [145]. The measurement area covered by XRR can be several square millimeters, depending on the size and angle of the incident beam, while atomic force microscopy only examines a small local area (typically some square micrometers) [146].

2.4.3 X-ray diffraction

X-ray diffraction (XRD) is a powerful technique used to study the structure of materials, particularly thin films. During an XRD measurement, X-rays are directed at the film and diffracted into different angles. These diffracted X-rays, known as Bragg peaks, are then analyzed. From an XRD measurement, one can learn about the phases present, the size of the crystallites, the lattice strain, the crystallographic texture, and defects such as stacking faults and strain distribution. However, the level of detail obtained depends on the properties of the film being studied, such as its thickness and the extent of its texture [14]. X-ray diffraction occurs when X-rays scatter of of the planes of atoms in a crystal, creating constructive interference. The distance between these crystal planes is known as the d-spacing. The smaller the d-spacing, the greater the angle of diffraction 2θ.

XRD can additionally provide information about crystallographic defects in films. These defects include crystallite size, stacking faults, and non-uniform strain. Since XRD patterns are recorded in reciprocal space, crystallite size is inversely related to the reciprocal space resolution. In a perfect, infinite crystal, the atomic periodicity is uninterrupted over an infinite length and the diffraction peak will be infinitely sharp. However, in disordered materials where only local pair correlations exist, the X-ray scattering features are broad. The Scherrer equation is a commonly used method to obtain a measure of the crystallite size from XRD peaks [147]:

$$W_{\mathrm{FWHM}(2\theta)=\frac{K\lambda}{D\cdot cos\theta}},$$

where W_{FWHM} is the full width at half maximum of the diffraction peak, λ is the probing X-ray's wavelength (Cu $K_\alpha = 1.5406$ Å), K is a shape factor (0.94 for monodisperse cubic crystallites [148]) and D is the crystallite size. The crystallite size analysis was performed using the Py (111) diffraction peak. The XRD measurements were conducted using a Bruker D8 diffractometer, particularly well suited for thin film investigations. An example of an XRD diffractogram and its Gaussian fit is presented in Figure 2.15. The source-side and detector slits were set to 0.3 mm, the rotary absorber was in automatic mode, and the scan was recorded in the range of 43° to 45.5° with a step size of 0.05° and 5 s dwell time.

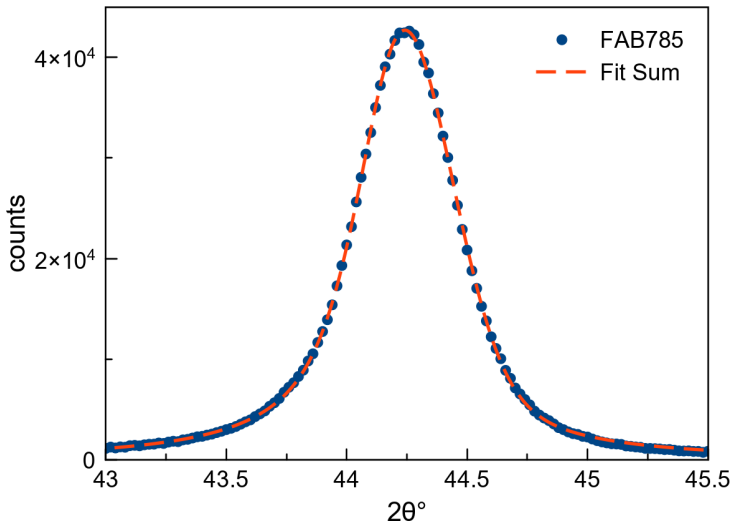

Figure 2.15: An example of an XRD diffractogram of the (111) diffraction peak from Py and its fit yielding a Scherrer average crystallite size 17.9 nm

2.5 Thin film patterning

Several of the experiments here have required patterned structures instead of continuous films. Structures with larger dimensions, such as permalloy discs, were patterned using optical lithography. However, to produce high-resolution permalloy structures, like nanowires, electron beam lithography (EBL) was used. Both methods involve coating the entire surface of a substrate by a resist and then using methods to remove the unwanted coating. This results in either opening undesired film areas for subsequent etching, or the desired pattern on the substrate surface to be covered by subsequent deposition (lift-off process). Photolithography makes use of resins that become photosensitive when applied to a surface and dried (photoresist) [149]. Electron-beam lithography utilizes electron-sensitive polymers (electron resist) (Figure 2.16). The areas of resist that are exposed to ultraviolet light or electron beams become soluble (positive resist) or insoluble (negative resist) in the developer solvent.

Thin permalloy films were patterned into a hexagonal lattice (5×5 mm) of discs with 80 μm diameter and 10 μm spacing using near-ultraviolet photolithography and ma-P 1215

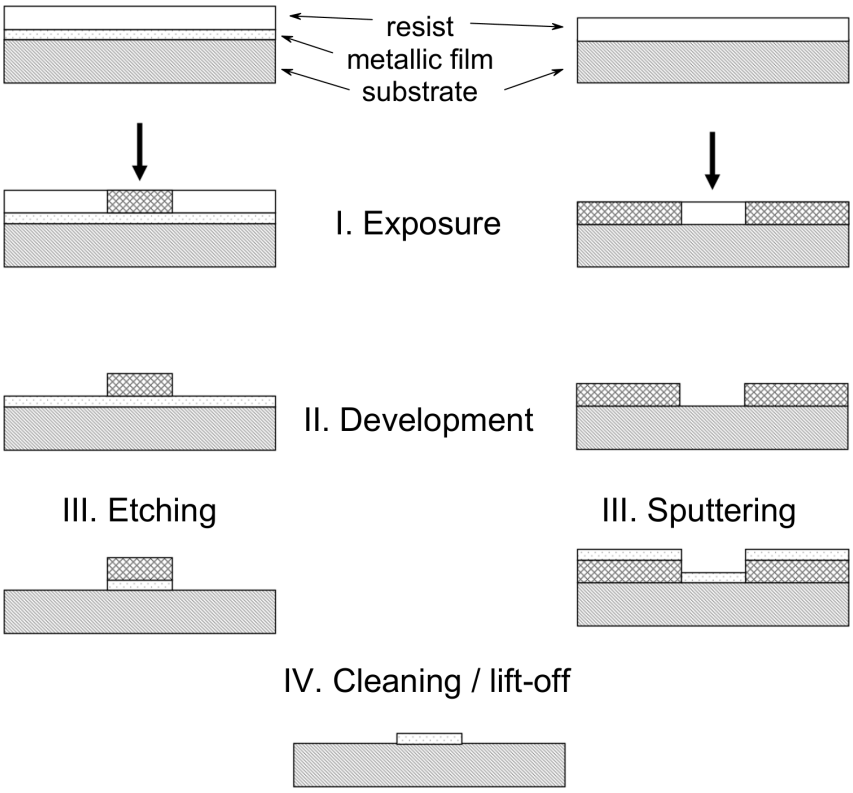

Figure 2.16: A diagram of the basic procedures for lithorgaphy using negative (left) and positive (right) resists

positive photoresist [150] on top of previously sputtered permalloy film and a specially produced metallic mask. The process involved a 30-second softbake at 90°C, followed by 5 minutes of Ar ion beam etching of the undesired areas of the Py film at normal incidence and at 300 eV (dose 300 μC/cm^2). The etching time was determined using available calibration rates. Residual photoresist was removed by soaking in acetone overnight and then 3 minutes of ultrasonic bath in acetone.

The Ørsted lines were patterned using negative photo/electron resist AR-N 7520.073 [151] on top of the CuN/Ta conductive stack on undoped single-crystalline silicon substrate with a thick thermal oxide layer (1 μm, ρ>10 kΩ·cm). The structure did not require maximum resolution, so the EBL parameters were chosen to accelerate the exposure: 80 nm step size, 120 μm aperture, 20 kV accelerating voltage and 10 mm working distance. The patterning was also followed by 5 minutes of Ar ion-beam etching under the same conditions. The etching time was determined by secondary ion mass spectroscopy [152]. Residual photoresist was removed by soaking in acetone overnight and then 3 minutes of ultrasonic bath in acetone.

Wavy permalloy wires required high spatial patterning resolution. To achieve this, a dose

correction similar to the one used in [153] was applied to obtain a well-defined width modulation; a part of the EBL design demonstrating the dose correction for patternig of wavy wires is presented in Figure 2.17. The structures were patterned using the positive electron resist PMMA A4, diluted with anisol, forming a uniform 200 nm thin film on top of the Ørsted lines prepared in the previous step. EBL parameters were chosen for maximum resolution: 2 nm step size, 7.5 µm aperture, 20 kV accelerating voltage and 8.5 mm working distance. The samples were then sputtered with thin permalloy films followed by the lift-off procedure in acetone. Sample patterning was performed by the author with invaluable help of *Alexander Pfeiffer* and *Tobias Reimer*.

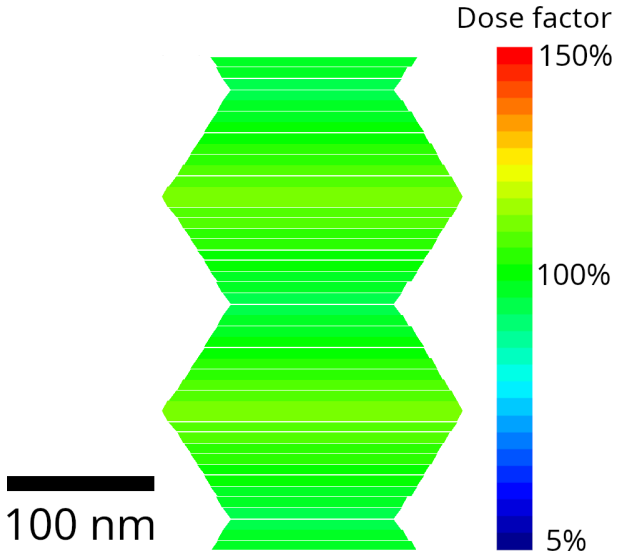

Figure 2.17: EBL design for wavy-wire patterning, resulting in 200 nm average width and 30 nm thick permalloy wires with ±5% width modulation amplitude and 200 nm period. The width of the EBL design varies from 120 to 200 nm and the dose factor from 0.75 to 1.00. The white areas are not exposed.

2.6 Measurement techniques for the magnetic properties of thin films

The magnetic properties of the thin Py films were studied using a vibrating sample magnetometer [154], which directly measures the macroscopic magnetic moment of the entire sample, and a Kerr microscope [155], which locally measures changes in sample magnetization and can be used to obtain normalized hysteresis loops. The use of both local and averaging approaches can reveal discrepancies between the results obtained using these two techniques, as investigated in the current work.

Vibrating sample magnetometry

Vibrating sample magnetometry (VSM) is a direct method of measuring the macroscopic magnetization moment of a sample. The instrument and technique were first developed in the 1950s by Foner [154]. VSM demonstrates high accuracy, versatility, and ease of use. The instrument works by oscillating a sample rod at a specific frequency, usually between 50 and 100 Hz, and a fixed amplitude, usually between 1-3 mm. An electromotive force is generated as the magnetized sample moves through the pickup coils, due to Faraday's law of induction [14].

All VSM measurements mentioned in the current work were performed by *Maria Andromachi Syskaki* using EZ VSM from MacroSense. The VSM hysteresis loops were recorded with 15° angular and 0.02 mT field resolution within 180° and ±2 mT range. The angle-resolved hysteresis loops allow for the extraction of the easy axis coercivity and anisotropy constant values, which are averaged over the sample under investigation. The measurement of the saturation magnetization was performed after calibrating the device using a thick Ni film, resulting in a 2% uncertainty in the obtained value.

Magnetooptical Kerr effect and Kerr microscope

The magneto-optical Kerr effect (MOKE) [156] is a widely-used experimental technique for studying the local magnetic properties of thin films and multilayers. Its advantages include high sensitivity, high temporal and spatial resolution, ease of use, and the ability to be implemented in situ, all at relatively low costs compared to alternative methods. Additionally, samples are not damaged or destroyed during observation and can be easily

manipulated, and different conditions like high or low temperature, mechanical stress or magnetic fields can be applied [22, 155, 157].

MOKE measurements in reflection using the magneto-optical Kerr effect [156] are based on small rotations of the polarization plane of light that can be observed under a polarizing microscope. For most materials, the results were not very promising until the introduction of the digital difference technique, which subtracts a saturated magnetic background image which also removes the non-magnetic information and enhances the magnetic contrast by averaging and digital processing. With such a setup, high-resolution observations up to the limit of optical microscopy are possible [158], based on a conventional polarizing microscope.

Hysteresis curves of the magnetization in Py thin films were obtained using the evico magnetics Kerr microscope, equipped with a 20× magnification objective, an in-plane rotable magnet and a set of blue LEDs (spectral maximum at 460 nm) within a ±2 mT field range with 0.02 mT step size and a 180° angular range with 5-15° resolution. The magnetic contrast is set parallel to the applied field in longitudinal mode and a dwell time 0.2 s is used. The propagation of domain walls was registered in subtraction images recorded using a 50× lens, with decreased contrast and 2× averaging.

Evaluation of the uniaxial anisotropy constant

To determine the directions of easy and hard axes the remanent magnetization vs. angle plot was fitted with the function $a \cdot |\cos(\alpha + x)| + c$ [159], where a is a normalization coefficient, α is the rotation angle with respect to the external probing magnetic field and x is the easy axis direction (Figure 2.18). The anisotropy constant was calculated as the difference between $M_s H_s - \frac{\int_0^{H_s} M_{asc} dH + \int_0^{-H_s} M_{desc} dH}{2}$ for easy and hard axis hysteresis loops [160, 161, 162], where M_s is the saturation magnetization, $M_{asc}(H)$ and $M_{desc}(H)$ are the ascending and descending hysteresis loop branches and H_s is the magnetic field value at which the sample reaches magnetic saturation.

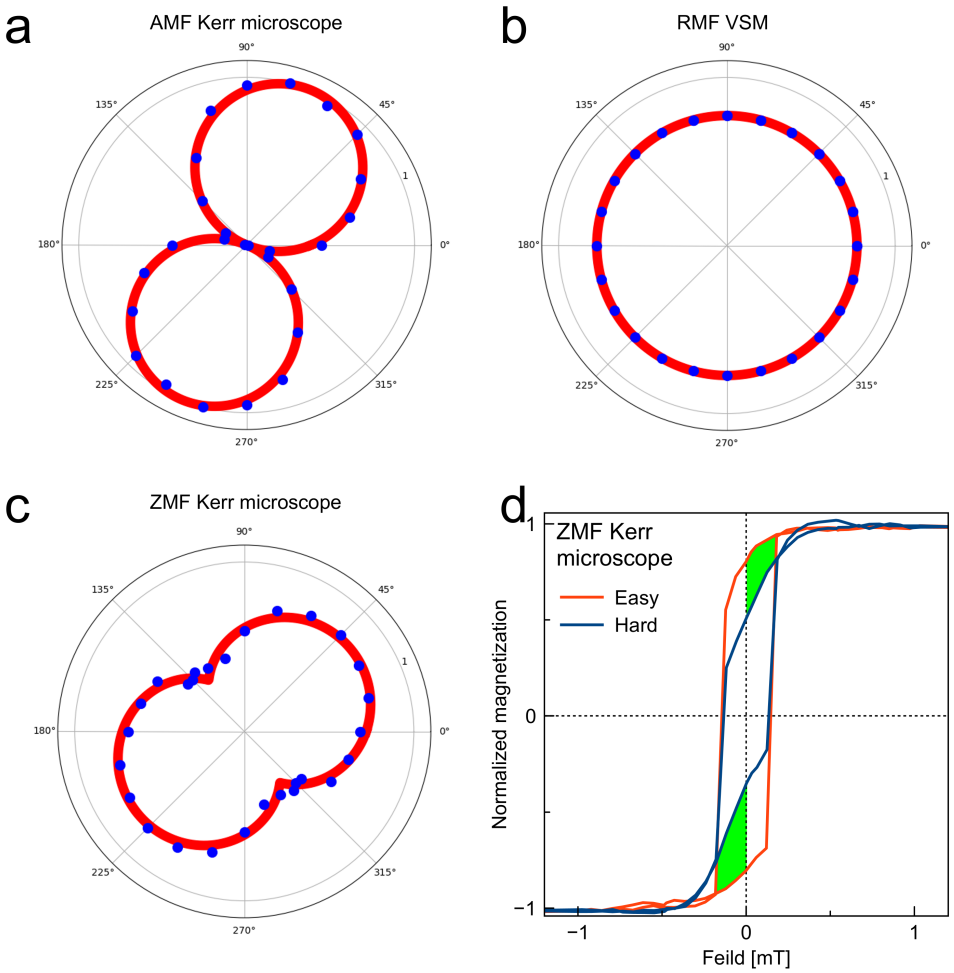

Figure 2.18: (a-c) Examples of angular dependencies of remanent magnetization measured using Kerr microscope or VSM (blue dots), along with their corresponding fits (red curves) using the modified Stoner-Wohlfarth model to determine the easy and hard axis directions. (d) Easy and hard hysteresis loops from (c) plotted with the green area representing the anisotropy constant$\cdot\frac{2}{M_s}$ (using the area method).

2.7 Generation of the Ørsted field

A simple setup developed by *Dr. Hermann Stoll* was used to send short electrical pulses through a 50 μm-long Ørsted wire. The output of a Keysight 33250A Function/Arbitrary Waveform Generator (with a 5 ns rise time) was connected to a Mini Circuits LZY-22+ amplifier (43 dB, 30 W, 0.1 to 200 MHz, 5 ns rise time), which was then connected to the sample that was mounted and wire-bonded to a RF-compatible sample holder. The output was also connected to a Tektronix DPO7254 oscilloscope through a 20 dB attenuator (as shown in Figure 2.19). The sample impedance was measured using a Tektronix DSA8300 analyzer with a 20 GHz time-domain reflectometry (TDR) module. Analysis of the pulse

shape and height before and after propagation through the sample using a pick-off tee revealed no change, which indicates that there was no significant sample heating within the utilized voltage range. The amplitude of the recorded oscilloscope signal is in agreement with the calculated reflection of the sample, which is caused by the impedance mismatch. This indicates that the sample is experiencing low Joule heating losses.

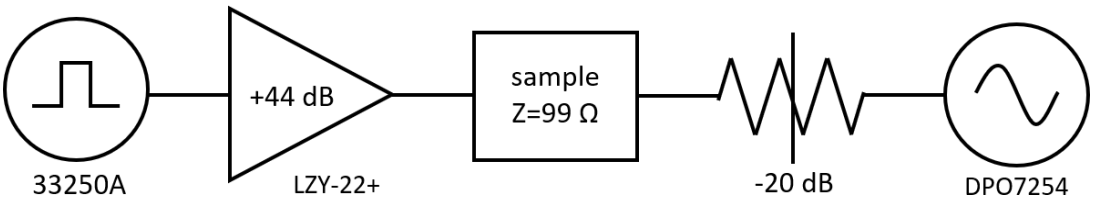

Figure 2.19: Experimental setup for generation of short Ørsted field pulses

The Biot-Savart law states that the magnetic field H at a distance r from an infinitely long, thin, current-carrying wire in Gaussian coordinates is equal to $\frac{2J}{cr}$, where c is the speed of light, J is the current in the wire, and the magnetic field vector and the cross product $J \times r$ are in the same direction [163]. In case of a conductor with rectangular cross section (Figure 2.20 a and b) the equation can be solved analytically [164]:

$$H_x = \frac{\gamma}{2}\left[\frac{-w}{2} ln\left(1+\frac{h^2+2z_0h}{\frac{w^2}{4}+z^2}\right) - 2(z_0+h)arctan\left(\frac{w}{2(z_0+h)}\right) + 2z_0 arctan\left(\frac{w}{2z_0}\right)\right] - \\ -\frac{\gamma}{2}\left[\frac{w}{2} ln\left(1+\frac{h^2+2z_0h}{\frac{w^2}{4}+z^2}\right) + 2(z_0+h)arctan\left(\frac{w}{2(z_0+h)}\right) - 2z_0 arctan\left(\frac{w}{2z_0}\right)\right];$$

$$H_z = \frac{\gamma}{2}\left[z_0 ln\left(1+\frac{w^2}{4z_0^2}\right) - (z_0+h) ln\left(1+\frac{w^2}{4(z_0+h)^2}\right) + w\left(arctan\left(\frac{2z_0}{w}\right) - arctan\left(2\frac{z_0+h}{w}\right)\right)\right] - \\ -\frac{\gamma}{2}\left[z_0 ln\left(1+\frac{w^2}{4z_0^2}\right) - (z_0+h) ln\left(1+\frac{w^2}{4(z_0+h)^2}\right) + w\left(arctan\left(2\frac{z_0+h}{w}\right) - arctan\left(\frac{2z_0}{w}\right)\right)\right].$$

The projection of the generated Ørsted field parallel to the sample surface H_x in the middle of the permalloy wavy wires is plotted in Figure 2.20 c.

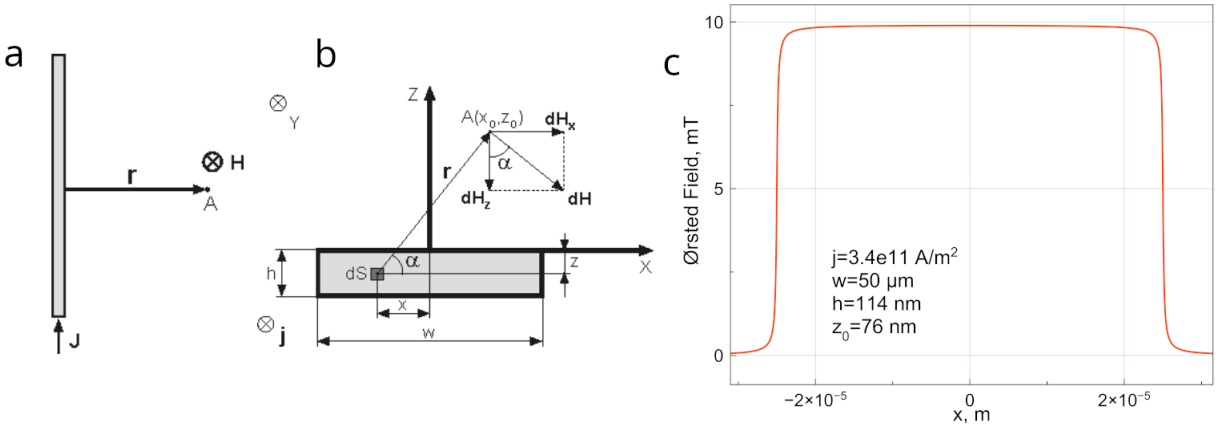

Figure 2.20: Schematics of a rectangular conducting wire (a) and its cross-section (b) [164] and the generated Ørsted field profile along the wire surface (c)

2.8 Micromagnetic simulations using mumax^3

Mumax^3 is a software that uses GPU acceleration to simulate the behavior of the magnetization in ferromagnets on the nano- to micro-scale [165]. It utilizes a finite-difference method [166] to discretize space, dividing it into a grid of orthorhombic cells. The program calculates the magnetization and effective field at the center of each cell, and the exchange strength between cells. The program computes the time-dependent dynamics of the reduced magnetization vector, which is represented by a unit vector $\frac{\partial \vec{m}}{\partial t} = \vec{r}$. Mumax3 employs the Landau-Lifshitz torque [31, 34] to calculate the dynamics of magnetization. We use following contributions to effective field:

- externally applied field
- magnetostatic field
- Heisenberg exchange field
- thermal field

Mumax^3 uses magnetostatic convolution to calculate the magnetostatic field. This method utilizes a finite-difference discretization and represents the magnetostatic field as a convolution of the magnetization with a demagnetizing kernel. Additionally, the program uses a 6-neighbour small-angle approximation to evaluate the effective field caused by the Heisenberg exchange interaction. To simulate finite-temperature effects, the program also includes a thermal field that fluctuates according to Brown's method [167].

Mumax^3 implements the RK45 Runge-Kutta method [168] also known as the Dormand-Prince method, which is a fifth-order convergence and a fourth-order error estimate. This allows for adaptive time-step control, which makes it suitable for dynamic simulations.

Mumax^3 provides a `relax()` function which aims to find the minimum energy state of the system. This function disables the precession term in the Landau-Lifshitz equation and causes the effective field to point towards a decreasing energy. The `relax()` function first advances in time until the total energy reaches a level where it is affected by numerical noise. Next, it starts monitoring the magnitude of the torque instead of the energy, since close to equilibrium the torque will decrease monotonically and is less noisy than the energy. The function continues to advance until the torque is also affected by noise. At this point, it is not possible to increase the accuracy anymore and the function stops advancing.

During the course of this project, various micromagnetic simulations were carried out to investigate the effect of a periodical modulation of the width on the propagation of magnetic domain walls (DWs) through nanowires. A standard value of the exchange stiffness for permalloy, $A_{\text{ex}} = 13 \cdot 10^{-12}$ J/m was used in all cases. For zero-temperature simulations, the value of the damping parameter was set to $\alpha = 0.01$ [169] and the saturation magnetization to $M_s = 7.95 \cdot 10^5$ A/m [10], as determined by means of a superconducting-quantum-interference-device (SQUID) measurement for the permalloy films grown in our lab. The cell size in the in-plane directions was set to 5 nm, which was chosen to not exceed the permalloy exchange length of $\Lambda = \sqrt{\frac{2A}{\mu_0 M_S^2}} = 5.7$ nm (μ_0 is the permeability of free space [170]), and the full film thickness t in the out-of-plane direction [10].

Firstly, the kinetic depinning fields were found for different magnetic wire structures. To do this, a DW was initiated in the unmodulated part of a wire consisting of an unmodulated and a width-modulated part, with wavy edges following sinusoidal curves of fixed phase and opposite sign (Figure 2.21). The thickness remains constant, while the width is modulated between $w \pm 2a$, where w is the average width, a is the amplitude, and $t \ll w$. The domain wall type was chosen based on the known DW phase diagram, taking into account the wire dimensions, and the state was relaxed before applying the field along the wire to displace the wall. Under an external field, the DW starts moving without pinning, propagates 1.5 μm and enters the modulated part under kinetic conditions. The

minimum field at which the DW continued its propagation is thus the kinetic depinning field.

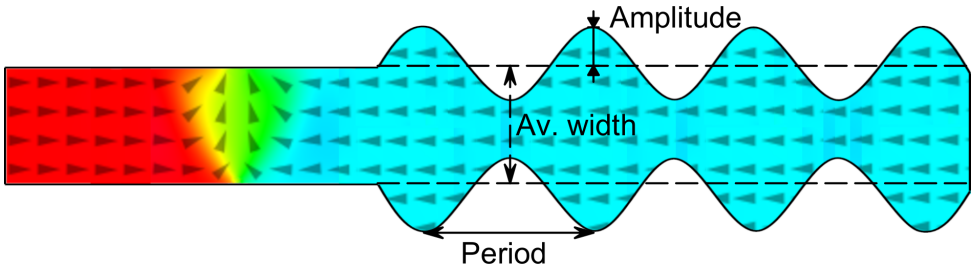

Figure 2.21: Scheme of the initial magnetization state for investigating the kinetic depinning fields

To evaluate the nucleation fields, additional simulations were performed with a ring in the vortex state with diameter $d = 8\ \mu$m, $w \ll d$. If an external in-plane field was applied above the critical value (nucleation field), the magnetization was observed to switch into an onion state with the formation of two DWs in the ring [171]. In these simulations, a larger value of $\alpha = 3$ was used to speed up the relaxation process [40].

To observe DW dynamics, the DW was propagated under external fields through 6 µm long wires with removed surface charges at the ends, mimicking an infinitely long wire. For room-temperature simulations, the material parameters used were $\alpha = 0.008$ and $M_s = 7.47 \cdot 10^5$ A/m for the Gilbert damping and the saturation magnetization ($\Lambda = 6.1$ nm), as determined by means of ferromagnetic resonance and VSM, respectively, for the optimized permalloy films grown in our lab.

Chapter 3

Optimizing the deposition of thin permalloy films for sensing applications

The results presented in this chapter have been partially submitted for publication as a paper. The results presented in this section are a collaborative effort by *Pascal Krautscheid* (magnetron sputtering, Kerr microscopy, and analysis), *Mehran Khanjani Vafaee* (magnetron sputtering), *Fabian Kammerbauer* (magnetron sputtering), *Maria Andromachi Syskaki* (magnetron sputtering, VSM), and the author (Kerr microscopy, XRR, XRD, AFM, and analysis).

Soft magnetic materials with small coercivity and controlled anisotropy are essential for the proliferation of magnetoresistance sensors in various fields, such as position sensing, biomedical applications, and flexible electronics. Permalloy is the most commonly used material for AMR sensors and is also utilized in PHE sensors, Hall effect sensors, and as a free layer in GMR stacks.

The chapter discusses selected parameters of magnetron sputtering to obtain magnetically softer permalloy films with a high AMR ratio. During the project, a perplexing phenomenon of random uniaxial anisotropy dispersion was observed, manifested in the discrepancy between local and average measurements of magnetic properties. This discrepancy was investigated and resolved through thin-film patterning experiments.

3.1 Magnetic sensors

Magnetic sensors converting the magnetic field into electrically mensurable signals are widely used in various industries and biomedical applications. Among the many types of magnetic sensors, magnetoresistive (MR) sensors are particularly appealing due to their low cost, small size, and high resolution at room temperature. Despite their relatively low sensitivity compared to other types of sensors (fluxgate and SQUID), MR sensors are ideal for miniaturization and integration, making them suitable for applications such as biosensors, wearable devices, and smart systems. Additionally, their compatibility with complementary metal-oxide-semiconductor (CMOS) fabrication processes allows for the integration of sensors and computing circuitry into systems on chip, which is highly desirable for internet of things applications. Specifically, MR sensors are expected to see significant growth in areas such as position sensing, biomedical applications, and flexible electronics [64].

Anisotropic magnetoresistance (AMR) sensors, which feature high sensitivity at low magnetic fields and low energy consumption, have recently demonstrated ultra-sensitive detection capabilities down to the 1 nT range [73]. Compared to tunneling magnetoresistance (TMR) or giant magnetoresistance (GMR) sensors, which require complex layer stacks, AMR sensors are simpler and easier and cheaper to fabricate.

However, the sensitivity as a derivative of the resistance of AMR sensors is very small at low angles between the current and the magnetization and the sign of the magnetic field cannot be determined. Barber pole structures are normally introduced to address these issues, consisting of a series of strips of high electrical conductivity that force the current flow at an angle of 45° with respect to the x axis [65]. Planar Hall Effect (PHE) sensors inherently do not have this drawback and have other advantages over AMR sensors, including less sensitivity to temperature drift, which limits the resolution at low frequencies [73]. The field sensitivity of PHE and AMR sensors can be increased by using materials with a high AMR effect and low field anisotropy. The field operating range of AMR/PHE sensors is also determined by the anisotropy field of the sensing material.

Overall, AMR sensors are popular due to their simple fabrication process, easy miniatur-

ization, and robust structure, which allows for fabrication on various substrates, including flexible and stretchable ones [64]. Permalloy is the most commonly used material for AMR sensors due to its low coercivity and negligible magnetostriction, which can also be used to fabricate sensors on flexible substrates [172, 173, 174].

Permalloy used in magnetoresistive sensors should possess a number of characteristics, including low coercivity, which is ensured by the ratio of nickel to iron in the composition. Secondly, low pinning, which is usually related to the quality of the substrate. In the presented study, we focused on obtaining films with the lowest possible coercivity and on controlling the anisotropy, on which the sensitivity and range of use of the sensors depends.

The task of investigating permalloy thin films was initially divided into several steps. Among the modifiable parameters of film deposition, the Singulus Rotaris can vary the target position (between two non-equivalent positions), the rotation speed of the sample carrier, the inert gas flow associated with chamber pressure, the sputtering power and the effect of an external magnetic field.

As the target tilt introduces additional uniaxial anisotropy, the permalloy target in all depositions is positioned at a lower tilt angle. Post-treatment of the films usually involves magnetic field annealing. This procedure is associated with grain coarsening and increase in coercivity, so we have omitted this step.

Firstly, we checked the homogeneity of permalloy sputtering at various positions on the sample holder. In addition, in order to test the influence of residual magnetic material on the magnetic properties of the permalloy films, test sputterings were carried out on clean single-crystalline silicon sample holders. No significant changes in magnetic properties were found so that specially fabricated aluminium sample holders were reused for subsequent sputterings.

In a second step, the effects of deposition power and chamber pressure on grain size and roughness and on anisotropy and coercivity were investigated. The final step focused on lateral anisotropy dispersion and its control by an external magnetic field applied during deposition, as well as a reliable way to measure the anisotropy of soft magnetic films.

3.2 Magnetron sputtering uniformity

To investigate the uniformity of permalloy films sputtered in different positions of the sample holder, a set of samples was prepared. The material stack consists of a 4 nm $Ni_{47}Cr_{42}Fe_{11}$ seed layer [78], a 30 nm $Ni_{81}Fe_{19}$ (Py) magnetic layer, and a 4 nm Ta capping layer for oxidation prevention (Figure 3.1 a). The stack was sputtered onto 1x1 cm^2 thermally oxidized (001) p-Si substrates with a 100 nm oxide layer. To check the deposition uniformity, four substrates were placed in different positions on a 20 cm diameter clean silicon wafer (Figure 3.1 b; chamber pressure P_{Ar} =(6.0 ±0.2)·10^{-3} mbar, deposition power 400 W). Subsequent measurements revealed no measurable difference in thickness, roughness (XRR), coercivity, or anisotropy (Kerr microscope).

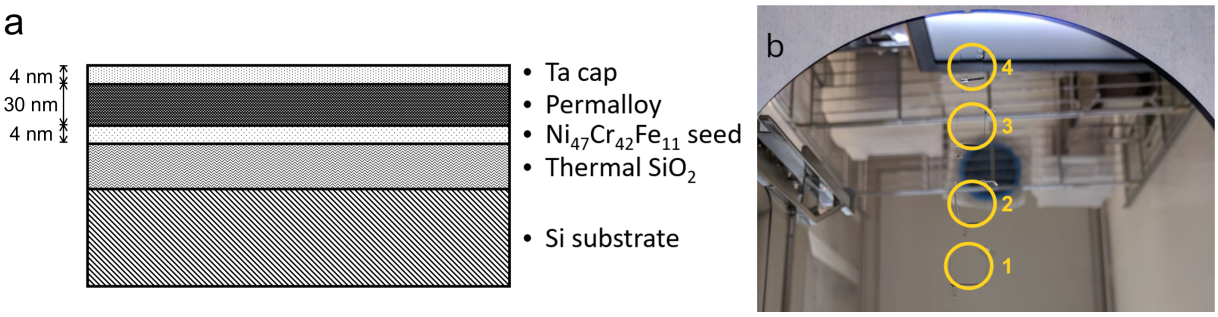

Figure 3.1: (a) The scheme of the magnetic material stack and (b) a photo of the substrates glued to the clean silicon wafer before the deposition for the sputtering uniformity test

Another set of samples was sputtered with different wafer rotation rates (same sputtering parameters; 15, 30 or 60 RPM). The coercivity and anisotropy of the samples are plotted in Figure 3.2. The sample sputtered at 60 RPM had the lowest values for both in-plane anisotropy and coercivity, so this condition was used for all subsequent depositions. The difference in wafer rotation rate observed in Figure 3.2 may be due to the relation between the deposition rate (0.1 nm/s) and the rotation rate. The wafer completes 1 rotation while depositing ≈2, 1, or 0.5 effective monolayers of Py respectively.

One can trace the effect of the Py target erosion by comparing magnetic properties of thin films. Under the same conditions but at different stages of the targets' lifespan thin film samples exhibit significant differences in anisotropy and coercivity values. Specifically, us-

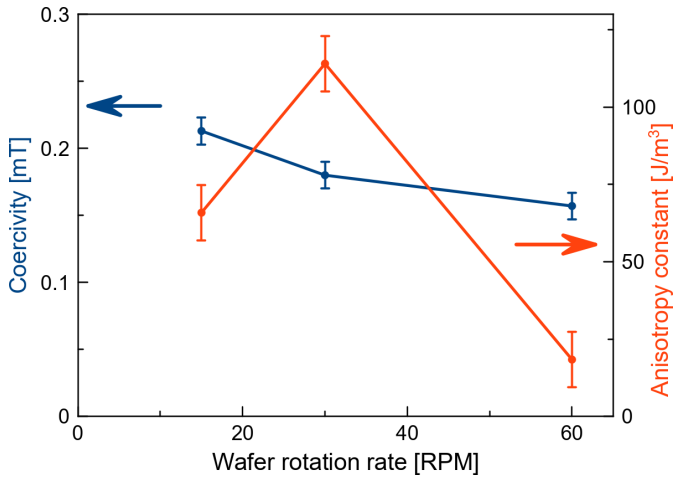

Figure 3.2: Magnetic coercivity and anisotropy of thin Py films sputtered with different wafer rotation rates in zero applied field

ing a "fresh" target immediately after the first pre-sputtering results in the production of the softest magnetic films, when all other conditions are held constant. Figure 3.3 shows the difference in hysteresis loops of two permalloy films sputtered under nominally the same conditions but at different stages of the same Py target's lifespan (4.4% and 72.9% from 100% stated by the manufacturer). The samples presented further in the work to analyse the permalloy properties depending on chamber pressure, sputter power etc. were deposited on the same day within a narrow region of the targets lifespan to avoid discrepancies caused by the target ageing.

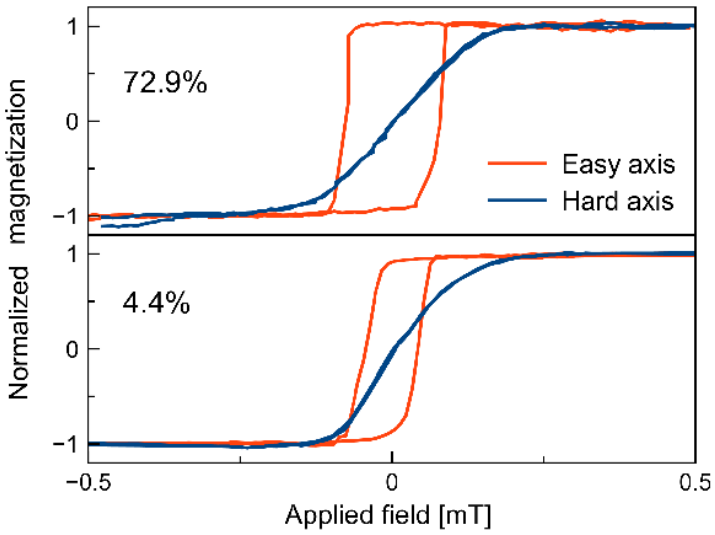

Figure 3.3: (Hysteresis loops of two permalloy films sputtered using the same Py target after 4.4% and 72.9% target consumption under same sputter conditions

3.3 Tailoring the magnetic properties of Py thin films

This section investigates the connection between the sputter parameters (power and chamber pressure) and the properties of thin permalloy films. The deposition parameters affect grain size, the density and roughness of the magnetic films, which is reflected in their resistivity, coercivity and anisotropy.

In the Singulus Rotaris system at fixed room temperature, the easiest parameters to adjust are the argon flow to regulate the chamber pressure (Figure 3.4a) and the power applied to the cathodes linked to the deposition rate (Figure 3.4b). We found that changing the flow of argon gas affects the deposition parameters by transitioning between zones 1 and T (see section 2.3), with lower pressures leading to denser and smoother Py films with lower coercivity and anisotropy [95]. Increasing the sputter power increases the deposition rate and results in a higher number of nuclei and smaller grain size in the *xy*-plane [175]. Smaller grain size in permalloy are generally associated with a lower coercivity [126, 175, 176, 177]. The grain size can be adjusted by changing the sputter power, depositing on heated substrates [176], or post-deposition annealing [126].

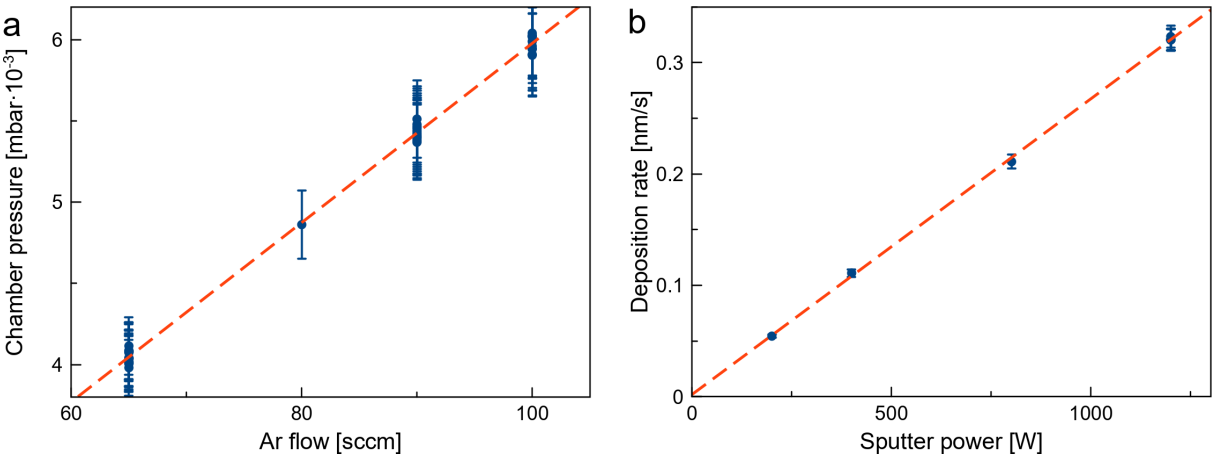

Figure 3.4: Parameter control in the Singulus Rotaris system: the Ar flow regulates the chamber pressure (a) and the sputter power affects the deposition rate (b)

Two different field protocols were used to sputter all Py thin films: an ”aligning” magnetic field (AMF) that remained fixed in relation to the rotating sample’s frame of reference, and a ”rotating” magnetic field (RMF) that remained fixed in the laboratory frame and

rotated in relation to the film's frame of reference. While sputtering the Py films, magnetic fields of up to 5 mT were generated by four pairs of sinusoidally commutated solenoids placed in vacuum around the sample holder. The $Ni_{47}Cr_{42}Fe_{11}$ layer was always sputtered using the same protocol as the Py layer. A third set of samples was prepared without any additional magnetic field (ZMF, zero magnetic field).

A first group of Py films was sputtered at room temperature using an external in-plane RMF of 5 mT, with different adatom energies achieved by varying the chamber pressures and different deposition rates achieved by varying the sputtering power. The chamber pressure was fixed at $4{\cdot}10^3$ mbar for samples with varied sputtering power, and the sputtering power was fixed at 1200 W for samples with varied chamber pressure.

The sputtering rate has a strong, approximately linear dependence on deposition power and is only slightly affected by chamber pressure within the investigated range (Figure 3.5 a). The Scherrer crystallite size varies significantly and does not follow the adatom energy in a simple linear relation: it increases when the deposition power is lowered, which is associated with lower adatom energies, but it also increases when the Ar pressure is lowered, which is associated with higher adatom energies. The average grain size determined from AFM data shows a similar trend to the Scherrer crystallite size obtained from XRD. The root-mean-square roughness of all samples, obtained from $5{\times}5$ μm^2 AFM scans, is also given in Figure 3.5 a.

The magnetic properties of the resulting continuous films, obtained locally using Kerr microscopy and integrating over the whole field of view, are presented in Figure 3.5 b, in relation to the average crystallite size obtained from XRD. Both the anisotropy and the coercivity of the Py films decrease simultaneously with increasing adatom energy, which can be achieved by either increasing the sputtering power or lowering the chamber pressure. In contrast, the thin-film resistivity demonstrates a linear correlation with the Scherrer crystallite size (shown in the inset). The AMR values for all measured samples are $(2.5{\pm}0.2)\%$ for the thickness of 30 nm and room temperature. The combination of a low inert-gas pressure and high deposition power, resulting in high deposition rates, enables achieving low coercivity and anisotropy values of 0.01 mT and 18 J/m^3, respectively, for the 30 nm thick Py films sputtered in a RMF, while maintaining a high AMR ratio.

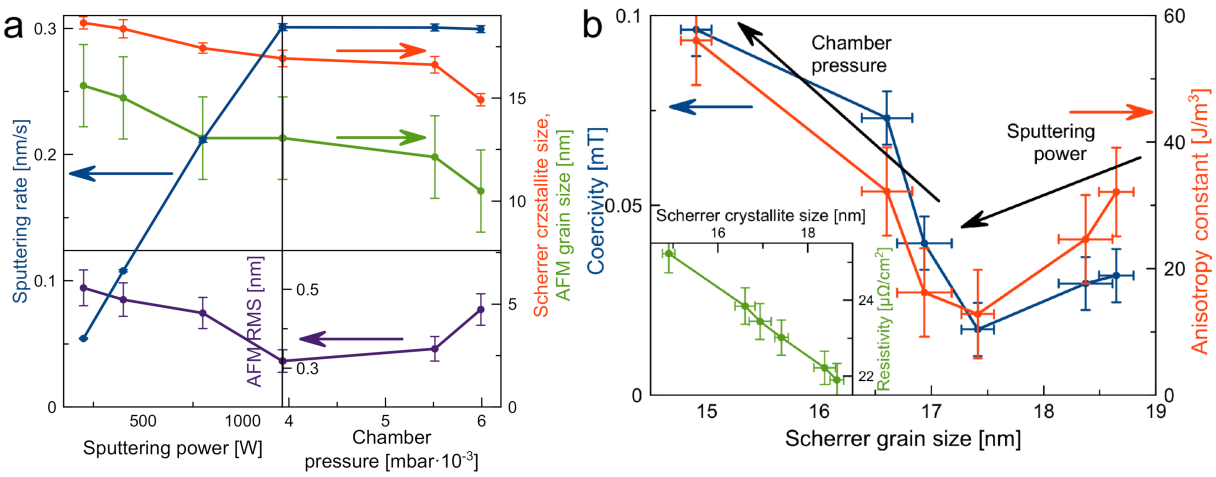

Figure 3.5: Properties of thin Py films grown with a rotating magnetic field (i.e., fixed in the laboratory frame) of 5 mT.(a) The sputtering rates (blue dots), Scherrer average crystallite sizes (red dots), AFM average grain size (green dots) and AFM RMS (purple dots) of Py films sputtered with different powers and chamber pressures are shown. The chamber pressure was fixed at $4{\cdot}10^{-3}$ mbar when the sputtering power was varied and the sputtering power was fixed at 1200 W when the chamber pressure was varied. (b) The coercivity (blue dots), anisotropy (red dots), and resistivity (green dots) of the continuous permalloy films are presented as a function of the Scherrer average crystallite size.

Despite the expected disorienting effect of sputtering on the rotating substrate and the use of a RMF to eliminate the anisotropy, all samples exhibit a small but finite anisotropy in the range of a few tens of J/m^3.

The deposition method, the *fcc* crystal lattice, and the use of a NiCrFe underlayer lead to {111}-textured films with a columnar structure, with grain size in the z-direction being close to the film thickness [14]. Figure 3.5 a shows a significant discrepancy between the XRD and AFM results on grain/crystallite size. The AFM data only records the grain size distribution in the xy-plane, which explains the systematically smaller values compared to the Scherrer analysis of the XRD results. The Scherrer analysis implies a spherical shape of the Py crystallites, while they are actually extended along the growth direction. The observed decrease in electrical resistivity with increasing grain size in Figure 3.5 b is the expected behavior [69] and supports the tendencies from both AFM and Scherrer analyses shown in Figure 3.5 a. The roughness values of the samples were evaluated from the AFM scans and found to be very low (RMS 0.3-0.5 nm). These values are presented in Figure 3.5 a. Figure 3.5 b demonstrates a peculiar non-monotonic dependence of the coercivity and anisotropy of the permalloy films on their average crystallite size. The coercivity of thin permalloy films is typically reported to show a monotonous increase with film

thickness and crystallite size for thicknesses above 5 nm [177, 176]. This grain coarsening is caused by Ostwald ripening [178] during deposition at high temperatures and is accompanied by a substantial increase in surface roughness [176]. Higher sputter power and lower chamber pressure both increase the adatom energy. Higher adatom energies at lower chamber pressure result in smoother and denser films due to the incorporation of excess atoms in the film, causing compressive stress [179] and reducing the coercivity. This qualitative behavior is also in agreement with the structure zone model [130] for sputtering, as introduced by Thornton [129]. Decreasing the chamber pressure at a fixed high sputter power leads to a transition from Zone 1 to the transition Zone T (see Figure 2.11, which is accompanied by an increase in grain size. No significant changes in density or roughness of the sputtered films were observed by XRR, but even minor changes in density and roughness can result in significant changes in coercivity.

While the chamber pressure has almost no effect on the deposition rate (Figure 3.5 a), the deposition rate changes proportionally with the sputter power. Increasing the sputter power has two effects: while the increased adatom energy still favors larger grains through stronger self-annealing, the increased deposition rate leads to stronger nucleation (magnetron sputtering of metals starts according to the Volmer-Weber mechanism [123]), resulting in smaller grains, which is found to be the dominant mechanism in the studied films. It is therefore the best quality films, i. e. those with the lowest roughness, coercivity and anisotropy, are deposited if the sample holder rotates rapidly (60 rpm), and the chamber pressure ($4 \cdot 10^{-3}$ mbar) is reduced together with an increase in the growth rate by means of a higher deposition power (1200 W).

3.4 Lateral dispersion of the uniaxial anisotropy

This section investigates a method for further improving the magnetic properties of permalloy films (i. e., lowering the coercivity and controlling the anisotropy) that were sputtered under the conditions optimized in the previous section, using external magnetic fields. The study delves into the puzzling finding of spatially varying, non-zero uniaxial

anisotropy directions and examines it in detail.

Several sets of Py film samples, sputtered in the absence of an additionally applied magnetic field (ZMF), in a suppressing magnetic field (RMF), or in an aligning magnetic field (AMF) were investigated using both local Kerr microscopy and integral VSM, averaging over the entire sample. When the strength of the external magnetic fields applied during sputtering is varied with the other parameters fixed (chamber pressure P_{Ar}=5.5·10^3 mbar, sputtering power 1200 W, substrate rotation 60 RPM), it results in a collective change of both coercivity and anisotropy, as shown in Figure 3.6 a. Small magnetic fields of about 1 mT are sufficient to achieve the full effect of the RMF or AMF.

Sputtering permalloy films in strong external magnetic fields has been shown to induce uniaxial anisotropy with high anisotropy fields (up to 11 mT for 35 nm thick Py films deposited in 0.5 T AMF) measured locally using Lorentz microscopy [180]. The anisotropy constants measured in our films are close to those extrapolated from the Ref. [180], although they do not follow the reported linear dependence on the externally applied field. The magnetization pattern of continuous films exibits magnetization ripples, i. e. a local and quasi-periodic variation of the magnetization direction from its average direction [181, 182] (Figure 3.6 b; the sample was sputtered at 1200 W power, P_{Ar}=5.5·10^3 mbar, and at ZMF). The direction of the ripple is perpendicular to the mean magnetization vector [180]. The magnetization patterns observed can be described as solutions that minimize the micromagnetic energy, that is made up of three components: exchange energy, stray field energy, and a noise term that behaves like a random transverse field with white-noise characteristics [183]. This indicates locally varying directions of the magnetization. For samples sputtered in RMF or ZMF, the main ripple orientation does not follow the same direction across the sample, but it has random orientations in different probed points. A curved ripple pattern can be an indirect indication of the presence of defects in the magnetic film [184] or the interaction of cross-tie domain walls [185]. This magnetic behavior of continuous films, i.e. the formation of magnetization ripples in the switching patterns of globally isotropic Py films, was reported previously [96].

Local Kerr measurements reveal a finite anisotropy for ZMF and RMF samples, with random values and orientations when measured in different areas of the samples. Figure

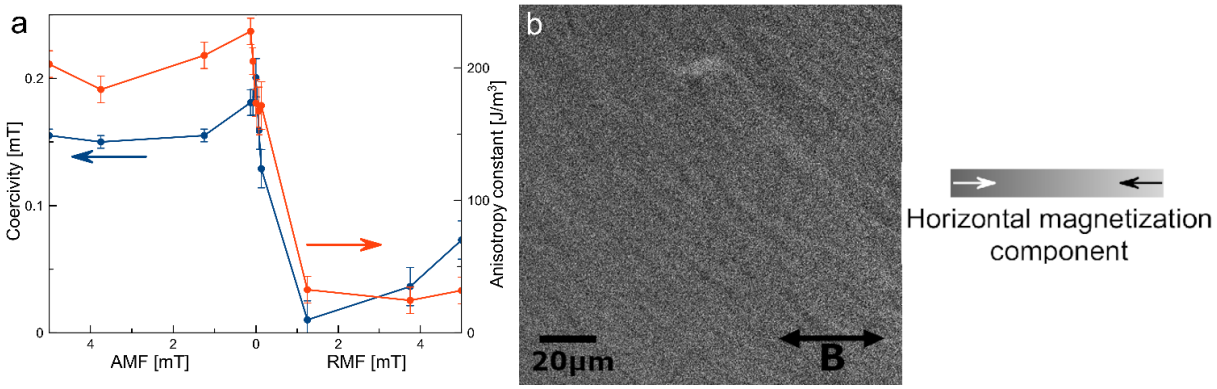

Figure 3.6: (a) Easy-axis coercivity (blue dots) and anisotropy constant (red dots) vs. applied magnetic field strength for AMF and RMF geometries as measured by Kerr microscopy and (b) emanent magnetization pattern of the ZMF sputtered Py film; the sensitive orientation of magnetic contrast in the Kerr microscope for all measurements is aligned with the indicated external magnetic field direction B

3.7 a shows remanence magnetization loops obtained for the ZMF sample (the sample was sputtered at 1200 W power, P_{Ar}=5.5·10^3 mbar) in different positions. A similar behavior is observed in the case of the RMF sample, while the AMF sample exhibits uniform values of anisotropy and coercivity throughout the sample (RMF and AMF samples are not shown). The local magnetic parameters measured in different areas of the continuous films vary in both direction and value of the anisotropy, while the easy-axis coercivity remains approximately constant.

The VSM results further highlight these differences (Figure 3.7 b): the hysteresis curves of the AMF sample exhibit a high degree of squareness in the easy direction and a zero-coercivity loop in the hard direction. The RMF sample shows zero spatially integrated anisotropy, and the ZMF sample still exhibits a low but finite anisotropy.

Various types of magnetic film defects can be sources of local anisotropy. To isolate sparsely distributed sources of stronger anisotropy that could be causing variations of the magnetic properties in RMF and ZMF sputtered Py films, the films were patterned into arrays of discs. The disc radii were chosen to be smaller than the area of uniform ripple orientation but much larger than the permalloy exchange length (≈5 nm), and the spacing is large enough to avoid significant interaction with neighboring discs. In the case of patterned films, the magnetization reversal is governed by the more homogeneous

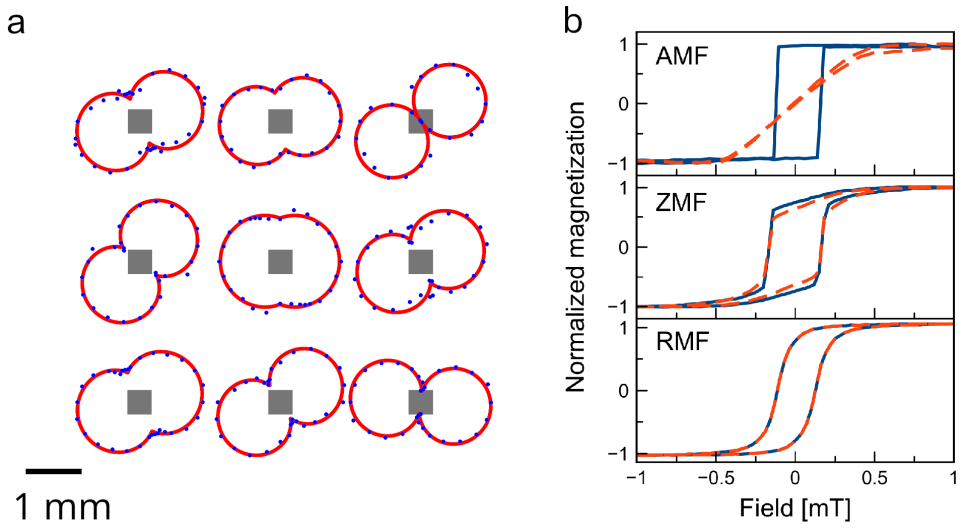

Figure 3.7: Impact of the different magnetic field modes applied during film deposition on the magnetic properties of continuous films. (a) The remanence magnetization is plotted against the angle of the field applied during measurement for RMF, and the normalized fits are shown. Grey squares indicate the areas on the continuous permalloy film that have been examined using Kerr microscopy. (b) Hysteresis loops obtained through VSM for AMF, RMF, and ZMF films. The loops for the easy axis are represented in blue, and those for the hard axis are in red.

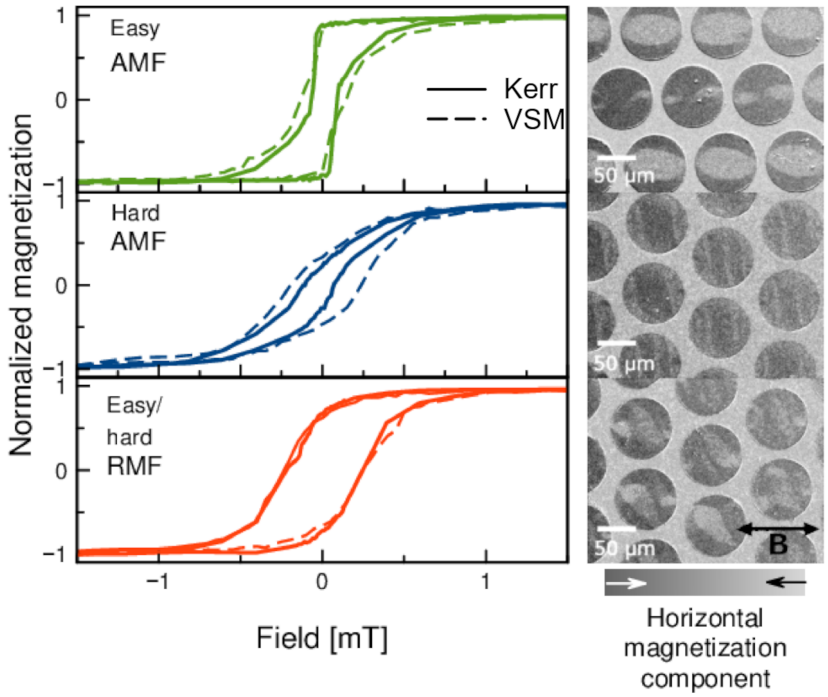

Figure 3.8: Hysteresis loops of patterned permalloy samples deposited using AMF and RMF are presented, with the solid lines representing local measurements taken with Kerr microscopy and integrated over the given field of view, and the dashed lines representing integral values obtained from the entire pattern using VSM; the remanent magnetization configurations that correspond to these loops are also shown

local material parameters as well as by a reduction of the stray field energy orienting the magnetic moments along the edges of the discs.

Using a square packaging might introduce biaxial anisotropy due to interaction between neighboring discs, so we chose a hexagonal arrangement, which also improves the signal-to-noise ratio of MOKE measurements due to a larger filling factor. Measurements of the angle-resolved coercivity and remanence magnetization on the patterned samples did not exhibit any notable angular $\frac{\pi}{3}$ -periodicity, so we can exclude a significant contribution of the dipolar interaction between discs. The remanent magnetization states and corresponding magnetization hysteresis curves (solid lines) of two samples are presented in Figure 3.8 (1200 W power, P_{Ar}=5.5·10^3, AMF and RMF). The corresponding hysteresis curves obtained for continuous films are given as dashed lines. Compared to the continuous-film results, the patterned AMF samples retain their easy-axis directions, but the easy-axis hysteresis loops become less square and the hard-axis loops exhibit a higher coercivity when patterned into discs. The hysteresis curves of RMF samples show higher coercivities in all in-plane directions and a completely vanishing anisotropy, which indicates that applying an RMF is an effective strategy to further optimize the permalloy properties.

The magnetic states of demagnetized discs of the presented samples are also qualitatively different: AMF permalloy discs tend to form S-states [186], where the magnetization is predominantly aligned with the easy axis, while RMF discs form single vortices with circular magnetization distribution dominated by shape anisotropy (Figure 3.9). For demagnetizing before taking the images, a gradually decreasing alternating magnetic field was applied in the horizontal direction.

Another interesting finding is the non-zero anisotropy of the Py films sputtered onto the rotating substrate in ZMF conditions (Figure 3.7). This provides further insight into the interaction of the aligning abilities of the tilted target and the external magnetic field. Previous studies have shown that without substrate rotation, a RMF during deposition results in isotropic Py films only for a normal target position, while target tilt results in a uniaxial anisotropy, with the direction and magnitude defined by the tilt angle [96]. Another study concluded that the deposition in a static external magnetic field using a tilted target with perpendicular (competing) directions results in a target-tilt-defined

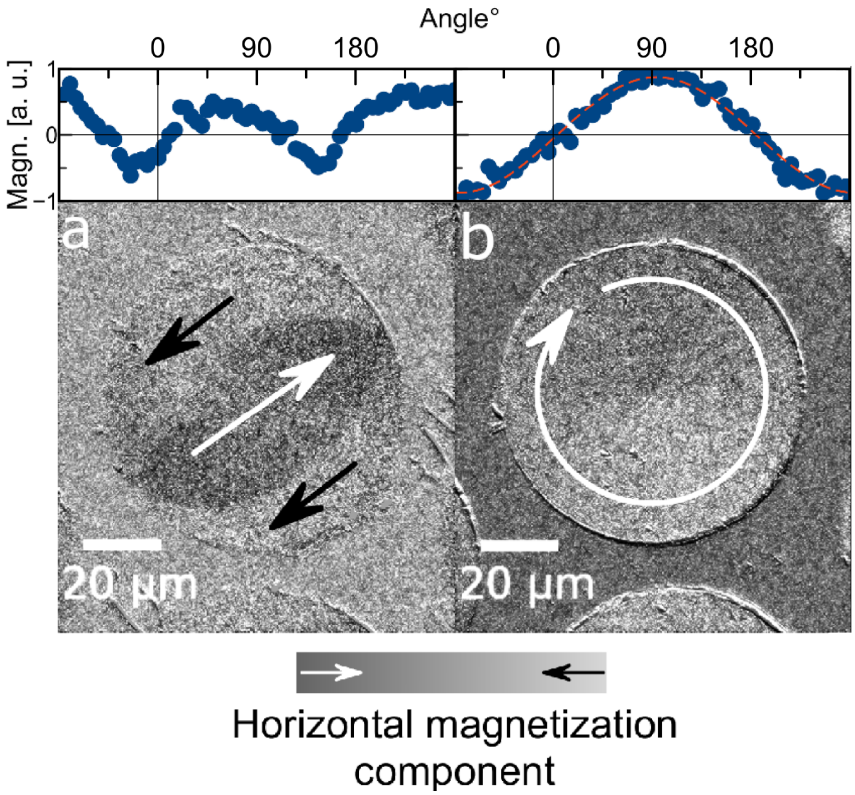

Figure 3.9: Characteristic magnetisation configurations of demagnetized permalloy discs from Kerr microscopy images: (a) S-state for AMF samples and (b) symmetric vortex state for RMF samples and the corresponding averaged intensities in a disc sector as functions of their polar angles

anisotropy direction [187]. In our experiment, the aligning effect of the magnetic field prevails over the disorientation caused by the target tilt, resulting in a well-defined uniaxial anisotropy (Figure 3.7 b, AMF sample). Globally isotropic films are only produced by the combined disorienting effects of the rotating molecular beam axis and the rotating magnetic field (Figure 3.7 b, RMF sample).

The microscopic examination of the magnetic properties of samples sputtered in RMF or ZMF reveals that within a single field of view there are significant variations in anisotropy directions and magnitudes. The varying anisotropy directions and magnitudes shown in Figure 3.7 a cannot be explained by a simple permalloy texture or strain that is symmetric across the sample, nor can it be explained by an influence from the edges of the film, which would result in a symmetric distribution. One possible explanation are random irregularities of the substrate during growth, such as dust particles, scratches or randomly formed magnetization clusters or voids, that orient the soft Py in an extended region around. Since Py is a very soft magnetic material, such defects can also serve as

DW nucleation sites, which dominate the switching properties of the film and lead to spatially varying hysteresis loops. In this case, the integral measurements may not be representative of the intrinsic properties of the Py but rather simply probe such random imperfections.

The shape of the hysteresis loops observed for the patterned AMF samples along the easy axis direction is typical for disc-patterned samples [188] and is caused by the formation of two magnetization vortices, followed by their migration to the disc edge and finally, annihilation. Switching along the hard axis occurs through the formation of elongated parallel domains confined by the disc size, resulting in an increased coercivity of the hysteresis loops. Switching in the RMF samples also takes place through the formation of multidomain states, however, they are more complex and show more variation (Figure 3.8). The magnetic state of the horizontally demagnetized discs of RMF Py is a symmetric vortex, which is the ground state in the discs in the absence of anisotropy. In contrast, the magnetization of the AMF discs reflects the interaction between the introduced anisotropy and the reduction of stray field energy at the edge of the discs, resulting in S-states. This approach to the study of samples exposed to AMFs or RMFs during deposition provides two observations. First, the AMF results in Py films with uniform magnetic properties and a defined anisotropy direction, despite the disorienting effects of the target tilt caused by substrate rotation. Secondly, it can be seen that the data obtained by the VSM and Kerr in Figure 3.8 are almost identical. Thus, patterning of the samples effectively isolates major defects. This results in the RMF Py films demonstrating isotropic magnetic properties on the relevant scales.

To conclude, the effect of varying magnetron sputtering conditions on the magnetic properties of Py was investigated. The best samples, characterised by the lowest coercivity (down to 0.01 mT) and vanishing average anisotropy, were obtained using higher sputtering powers (1200 W) and low argon pressures (4-10^{-3} mbar). A local variation of the magnetic properties of continuous Py films was observed despite the use of disorienting effects such as sample rotation with respect to the target tilt and the rotating external magnetic field. This variation was suppressed when such films were patterned into arrays of discs, suggesting a dominant long-range influence of random defects affecting the magnetic properties of the films in the unpatterned samples.

Chapter 4

Control of the Walker breakdown by periodical magnetic wire-width modulation

The results presented in this chapter have been partially published as a paper [189]. Improving the performance and reliability of devices that use magnetic domain walls, such as logic gates, memory storage, and sensors, requires finding a way to prevent the Walker breakdown [46] from occurring. Through computer simulations, it was demonstrated that by periodically changing the width of a wire in a specific way, one can completely suppress the Walker breakdown for a certain field range and conserve the spin structure of the magnetic domain wall throughout the entire device field operating window. However, the effectiveness of this technique varies depending on the width and thickness of the wire. Additionally, using this technique on intersecting wires was investigated and proved its importance. By preserving the structure of the magnetic domain walls, one can reduce the stochasticity of the DW propagation through a wire intersection.

Furthermore, the movement of magnetic DWs through wires with periodical wire-width modulation has been studied in an experiment using magnetic field pulses under the Kerr microscope. It was shown that the success of preventing the Walker breakdown depends on the shape of the wire, and that the velocity of the domain walls changes in a specific way that is different from wires with smooth edges.

4.1 Suppression of the Walker breakdown

One major challenge in using magnetic domain walls (DWs) in devices is their potentially unpredictable movement and pinning/depinning behavior [190, 191, 192]. This behavior is particularly problematic in devices that have complex geometries, such as curved wires [7, 48], notches [39], and intersections [193], where reliable DW propagation is difficult. In addition, real systems often have material and processing-related imperfections that can act as pinning centers, limiting the magnetic field operating window (FOW) and device reliability. The movement of DWs across these pinning centers is strongly affected by the DW spin structure.

Propagation of DWs above the Walker breakdown is undesirable in most applications because it results in unpredictable changes to the DW spin structure. Therefore, the most robust and preferred method for device applications is fast and steady propagation below the Walker breakdown. The Walker field depends on the wire composition [194, 195, 196] and geometry [196], but in many cases it is lower than the field required to move the walls in the device. Achieving precise control over the external field driving the DW in a real device is often not possible, which means that devices need to operate above the Walker field in highly random and turbulent DW propagation regimes.

To overcome these issues, various specific approaches to designing a magnetic wire have been proposed and shown to significantly affect the DW motion, providing ways to achieve deterministic and reliable DW propagation. For example, applying an oscillating longitudinal external magnetic field can suppress the Walker breakdown [197], but this is difficult to implement in devices. Simulations of magnetic wires with random, rough edges have also shown suppression of the vortex nucleation associated with the Walker breakdown, enabling higher DW velocities [45]. Another approach is the periodic modulation of the magnetic wire width using different geometries (such as comb-like [198], gap-introducing [199], triangular [200], or wavy [201, 202, 203, 204, 145, 205]) to generate a periodical stray field modulation and thus provide a means to control the Walker breakdown. Another possible mechanism that contributes to the suppression of the Walker breakdown is the absorption and emission of spin waves [203], which disrupt the DW spin structure transformations.

Research on these approaches has been conducted in simulations [202, 203, 204, 145, 205] and experiments [196, 203] on simple, short, and straight wires. In particular, a wire-width modulation with a period smaller than the Walker period has been proposed to disturb every spin-structure transformation and suppress the Walker breakdown [203]. Simulations have also demonstrated the suppression of the Walker breakdown by introducing a 50-nm-period wire-width modulation (100 nm average wire width, 10 nm thickness, 7.5% modulation amplitude) with fields up to 30 mT [202]. Enhanced robustness of DW propagation through magnetic wire intersections has also been observed by introducing wire-width modulation [205]. However, while the concept of wire-width modulation has been proven, more work is needed to determine the optimal geometries for maximizing the field operating window and achieving efficient device operation in both straight wires and more complex device elements such as intersections.

4.1.1 Introducing periodical width modulation in magnetic wires

The work conducted by Burn [203] provides a detailed examination of domain wall (DW) propagation and offers several important findings. Firstly, it demonstrates the potential to suppress the Walker breakdown by introducing periodical wire-width modulation. Secondly, it highlights the necessity for the modulation period to be smaller than the walker period of the corresponding wire. While these findings lay the groundwork for the present study, they lack an in-depth analysis of the observed phenomena. It is evident that the suggested modulation period of 400 nm cannot be universally applied to wires with different widths and thicknesses. Furthermore, the paper does not provide insights into how the wire geometry influences the walker period, nor does it provide a rationale for the chosen modulation amplitude.

The transformation of DWs occurs due to the interplay between Zeeman and stray field energy. The applied field's precessional torque overcomes the demagnetizing field in the presence of a damping torque, resulting in a net azimuthal torque that leads to the Walker breakdown [206, 46]. Consequently, periodic changes in the stray field may distort the

DW spin structure, thereby suppressing the Walker breakdown. The stability of the DW spin structure is dependent on the width and thickness of the magnetic wire [45]. To investigate the patterns of DW transformations, a magnetic wire configuration close to the isoenergetic line of the DW phase diagram was selected. This configuration is prone to transformations, and it is expected to exhibit the strongest response to varietions of e. g. the geometry, aiding in better understanding the mechanism behind suppressing the Walker breakdown. This mechanism can be later utilized for stable systems intended for device applications.

4.1.2 Isoenergetic configuration

In order to investigate the effect of a periodic wire-width modulation on the domain wall propagation, micromagnetic simulations on field-induced domain wall propagation were conducted for different amplitudes of the modulation, while keeping the other geometrical parameters constant. The magnetic wire cross section is 12 nm thick and 150 nm wide, just on the isoenergetic line of the phase diagram [45, 41, 44]. The simulated displacement of the DW versus time was analyzed to understand the propagation regimes. At low applied fields, the DW displacement changes linearly with time (as seen in Figure 4.1a, blue curve). As the field strength increases above the Walker breakdown point, periodic reverse DW motion is observed, reflected in oscillations in the graph and a decrease in average DW velocity (as seen in the change in slope in Figure 4.1a, red curve). The DW displacement over one time period is called the Walker period. At even higher applied fields, both the Walker and time periods gradually decrease and the propagation becomes more linear again (as seen in Figure 4.1a, green curve). When the wire width is modulated at an amplitude of 3%, the DW propagation mechanism is the same as in the unmodulated wire, but shifted towards higher magnetic fields, as demonstrated in the right panel of Figure 4.1a.

To further visualize this effect, the slope of the DW–displacement-versus-time curve was used to calculate the DW velocity, which is plotted in Figure 4.1b along with the Walker

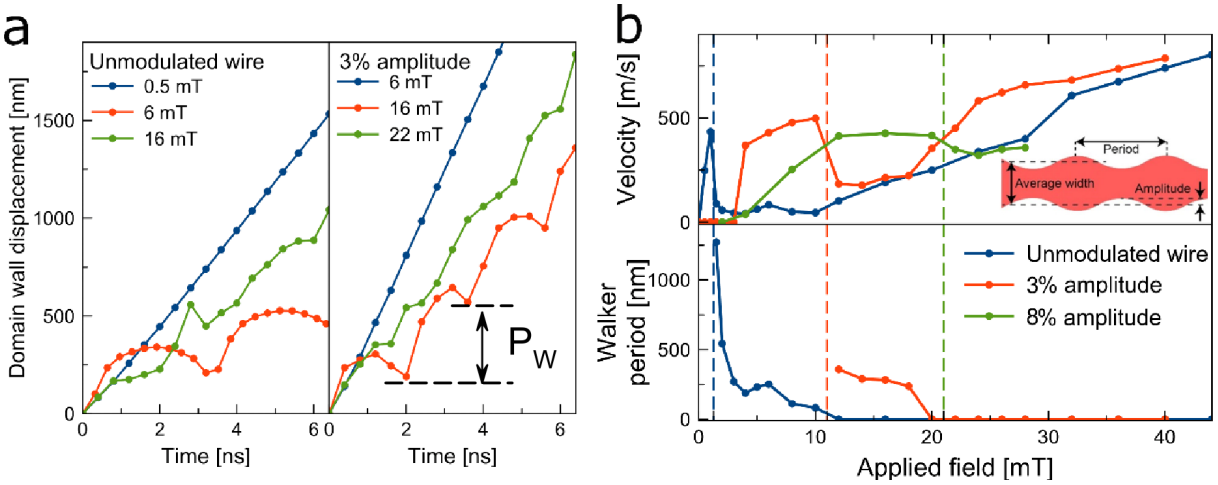

Figure 4.1: (a) Domain wall displacement under external field as a function of time for an unmodulated and a modulated (50 nm period and 3% amplitude) magnetic wire with 12 nm thickness and 150 nm average width. The curves show three different DW propagation regimes: steady (blue), oscillatory (red) and turbulent (green). (b) Examples of DW velocities and Walker periods vs. applied field for magnetic wires with 12 nm thickness, 150 nm average width, 50 nm modulation period and 0, 3, and 8% modulation amplitudes (blue, red, and green curve, respectively). The dotted vertical lines represent the Walker breakdown values for the corresponding wires. A schematic representation of the magnetic wire-width modulation is shown in the inset.

period as a function of the applied field. The figure demonstrates how a periodic wire width modulation affects the DW propagation. The graphs depict the simulated DW velocities and Walker periods for three magnetic wires with 150 nm average width, 12 nm thickness, 50 nm modulation period, and 0%, 3%, and 8% modulation amplitude (blue, red, and green curve, respectively). A schematic of the geometry can be seen in the inset. Corresponding snapshots from the simulations at certain time steps for selected field strengths of 6 and 16 mT are shown in Figure 4.2.

For the unmodulated wire (blue curve), a linear velocity–versus-field dependence is observed below 2 mT, followed by an abrupt velocity drop corresponding to the onset of oscillating DW motion with a slow average velocity and periodic spin structure changes, leading to a finite Walker period (as seen in Figure 4.2, 0% wire at 6 mT). Starting from 10 mT, the DW propagation becomes turbulent (0% wire in Figure 4.1 at 16 mT) and the DW velocity rises approximately linearly again with increasing applied field. Only above 20 mT does the velocity approach and then exceed the velocities in the steady-motion regime. In this turbulent regime, there is no well-defined change in spin structure and

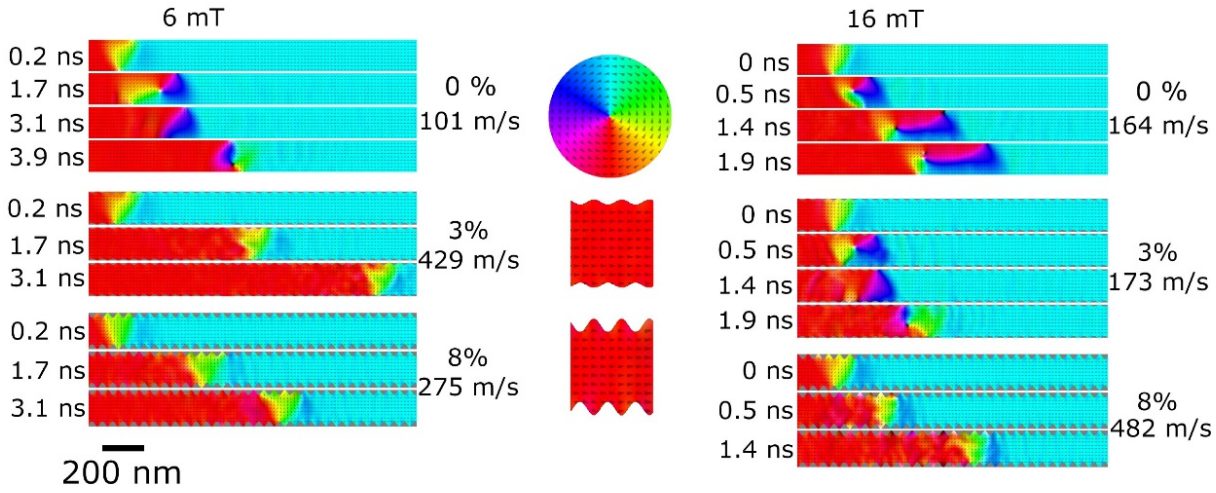

Figure 4.2: Snapshots of sections of the micromagnetic simulations demonstrating the DW propagation through an unmodulated (0%) magnetic wire and wires with 3% and 8% modulation (the same wires investigated in Figure 4.1) at certain time steps for selected field strengths of 6 mT (left) and 16 mT (right). At 6 mT the unmodulated wire undergoes a DW spin-structure transformation, while transverse DWs propagate through the modulated wires unchanged. At 16 mT the 3% modulated wire also exhibits a Walker breakdown accompanied by DW structure transformations and a significant drop of the average DW velocity, as indicated on the right, while the 8% modulated wire sustains a stable DW. In the center, a color wheel encoding the magnetization directions is given, together with enlarged sections of the modulated wires visualizing the used width modulation.

therefore the effective Walker period tends to zero.

The red curve demonstrates the case for 3% wire amplitude modulation. Here, there is no DW propagation below 4 mT, since the DW is pinned. With further increase in applied field, the DW is depinned and propagates steadily with increasing velocity up to the Walker breakdown at around 10 mT (as seen in the 3% wire in Figure 4.2 at 6 mT, which demonstrates steady DW propagation and at 16 mT oscillatory motion). Above 18 mT turbulent motion is observed. Periodical magnetic wire width modulation shifts both the Walker breakdown and the transition between oscillatory and turbulent regimes towards higher fields, and the range of the oscillatory regime shrinks significantly. The DW propagation in the turbulent regime demonstrates the same mechanism and similar velocities for both, modulated and unmodulated wires, as seen in Figure 4.1b.

The DW propagation in the modulated wire demonstrates only steady motion at lower fields (8% wire in Figure 4.1b) which becomes turbulent [48] above 21 mT. There are no oscillatory spin structure changes seen, resulting in no defined Walker period. The DW velocity vs. applied field curves demonstrate a smaller slope for higher modulation amp-

litudes in the steady regime.

It is evident that the Walker period is not constant for a specific wire geometry but rather depends on the external field as also expected from theory. In Figure 4.1b, for the magnetic nanowire with a 3% modulation amplitude (red curve), it is correct to observe that the Walker breakdown occurs when the modulation period (50 nm) surpasses the Walker period of the corresponding unmodulated wire (blue curve). However, it is clear that the wire with an 8% modulation actually shifts the Walker breakdown towards even higher fields.

4.1.3 Walker period

The periodical wire-width modulation induces spatial variations in the stray field, aiming to distort the transformations of the DW spin structure. These transformations occur periodically, and the Walker period serves as a spatial metric for them. As mentioned previously, the Walker period relies on the external field and the dimensions of the magnetic wire. To explore this dependency, a series of simulations was conducted using magnetic wires of varying widths and thicknesses. The outcomes of these 0K simulations are illustrated in Figure 4.3.

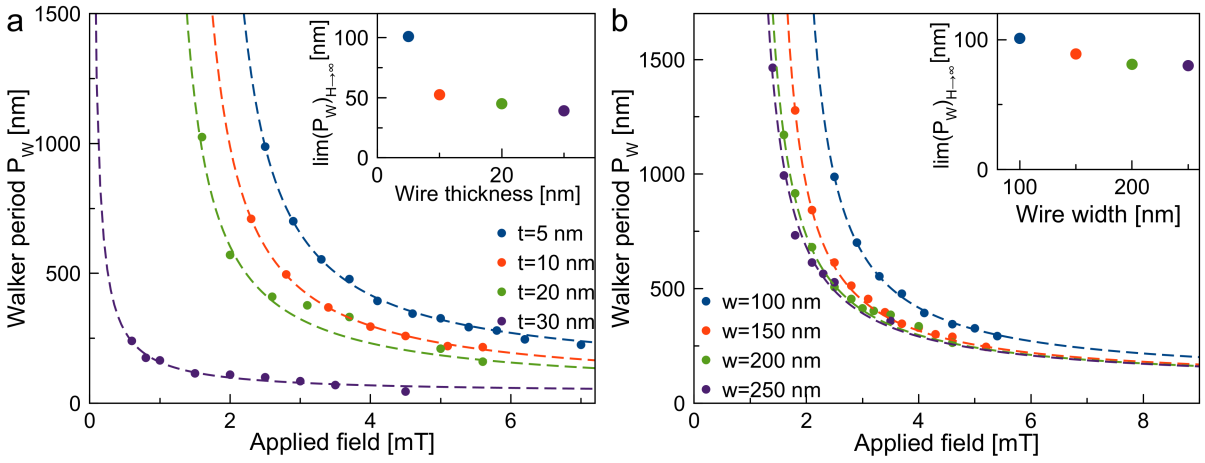

Figure 4.3: Walker periods of the DWs propagating in soft magnetic wires with rectangular cross-sections and straight edges: (a) the wire thickness is fixed t=5 nm and the width is varied, (b) the wire width is fixed w=100 nm and the thickness is varied. Dashed lines represent function fits

The obtained data points phenomenologically exhibit a resemblance to hyperbolic dependencies and were thus fitted using the equation $P_W = \frac{a}{H - H_W + c}$, where P_W represents the Walker period and H_W corresponds to the Walker field. Here, a denotes a normalization coefficient, and $c = lim(P_W)_{H \to \inf}$ represents the limit of P_W as H approaches infinity. The Walker fields derived from this equation demonstrate good agreement with Ref. [201] and Ref. [203]. Extrapolating the Walker periods to larger fields aids in identifying the optimal magnetic wire size and serves as a starting point for determining the optimal modulation period. The Walker periods decrease as both wire widths and thicknesses increase. These findings suggest a potentially more significant impact of periodical wire width modulation on thicker and wider wires compared to thinner and narrower ones.

When the wire-width modulation with a 10% amplitude [203] and various periods is introduced to the magnetic wires from Figure 4.3a, it results in an increase in the propagation field. This increase is attributed to the formation of an energy barrier between DWs positioned in the narrow and wide regions within the wires as previously studied [49]. The propagation fields, along with the corresponding fits from Figure 4.3a, are plotted in Figure 4.4. It is apparent that for thinner wires (t=5 nm, t=10 nm), the propagation fields for a given modulation period lie below the inverted P_W vs. applied field plot. This indicates the existence of a useful range for DW propagation within a modulated wire with a specific modulation period above the propagation field and below the Walker period value at the given field (indicated by the marked area in Figure 4.4). However, for thicker wires (t=20 nm, t=30 nm), the propagation fields lie below the Walker-period curves.

From Figure 4.4, it can be observed that for a 20-nm-thick wire, the lowest propagation field is achieved for a modulation period of 250 nm, resulting in a value of 6 mT. For a 10 nm thick, the depinning field for the same modulation period is 2.6 mT. Figure 4.5 showcases the displacements of DWs in these four wires (modulated and unmodulated with thicknesses of 10 nm and 20 nm) under different applied fields.

To compare the impact of periodic wire-width modulation on the behavior of DW in the two latter cases, plots of DW velocities versus applied field are presented in Figure 4.5. In the case of the unmodulated wire with a thickness of 10 nm (Figure 4.5a), distinct

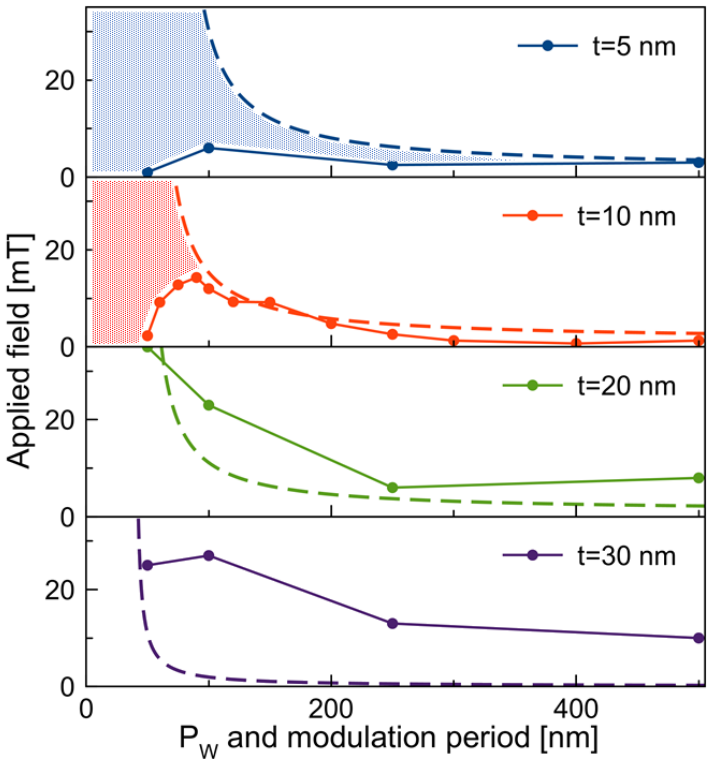

Figure 4.4: DW propagation fields in magnetic wires with different thicknesses and periodical width modulation, 250 nm average width and 10% amplitude (solid lines), compared to the inverse P_W vs. applied field fits for unmodulated wires (dashed lines). The marked areas represent a useful range for DW propagation within a modulated wire with a specific modulation period above the propagation field and below the Walker period value at the given field.

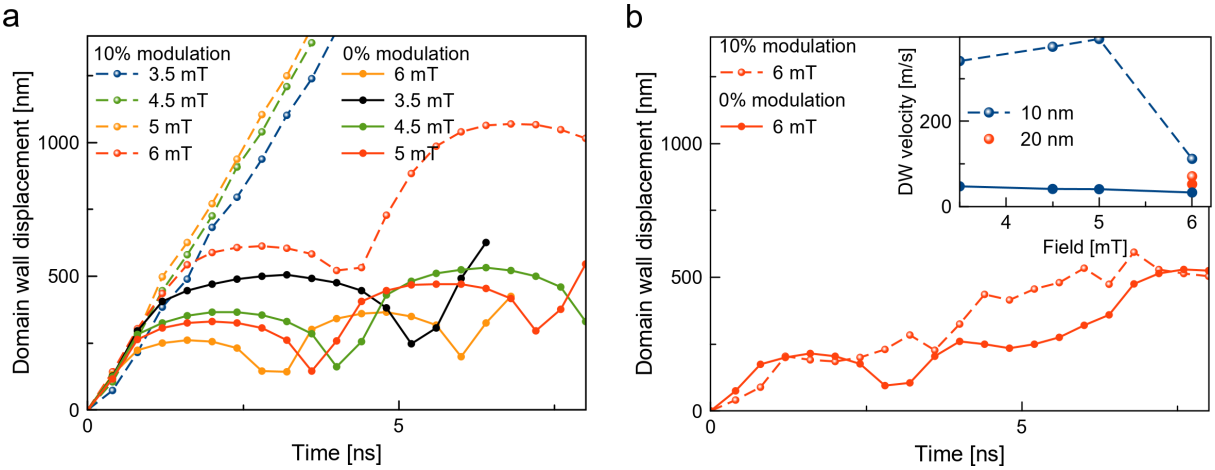

Figure 4.5: DW displacement plots under external fields of different amplitudes versus time for unmodulated (0% modulation amplitude, solid lines) and modulated (10% modulation amplitude, 250 nm period, dashed lines) magnetic wires with (a) 10 nm and (b) 20 nm thickness, the average wire width is 100 nm. The DW velocities for both cases are given in the inset.

oscillations can be observed, with the period decreasing at higher fields. However, the introduction of a width modulation suppresses the transformations of the DW spin struc-

ture at low fields. At 6 mT, the oscillations reappear, but their period is much longer compared to the unmodulated wire. For the 20 nm thick wire, both the modulated and unmodulated wires exhibit turbulent DW propagation already at 6 mT (Figure 4.5b). The inset in Figure 4.5b shows the DW velocities. In the case of the thinner wire, a clear suppression of the Walker breakdown is observed, accompanied by a significant increase in DW velocities. Conversely, for the thicker wire, the DW velocity remains almost unchanged.

4.1.4 Nucleation field

Another significant finding derived from the micromagnetic simulations (see section 2.8) is the reduction in the nucleation field, resulting from the introduction of periodical wire-width modulation. The DW nucleation fields are dependent on the magnetic wire dimensions [48], as represented by the equation $H_n = \frac{1}{2} M_s \frac{t}{t+w}$, where t and w are the thickness and width of the wire, respectively, and M_s is the saturation magnetization. The local widening of the wire in the modulation process results in facilitating the nucleation of new, undesired DWs at lower fields in the modulated wire, in comparison to the unmodulated wire.

Overall, the periodic wire-width modulation with 3% amplitude in Figure 4.1 expands the upper limit of the steady DW flow range from 2 mT to 6 mT, but with a slight reduction in the range of oscillating DW propagation. Additionally, the field operating window (FOW, the range between the DW depinning and nucleation fields) decreases from 44 mT for the unmodulated wire to 36 mT for 3% amplitude modulation. There is also a small increase in the maximum steady-state DW velocity. With a larger modulation amplitude of 8%, the DW depinning field is pushed to even higher fields (5 mT) and the nucleation of new DWs occurs at lower fields (28 mT), resulting in a reduction of the FOW to 23 mT compared to 44 mT in the case of the unmodulated wire.

Introducing a wire-width modulation with increasing amplitude, the DW depinning field

gradually rises while the nucleation field decreases. Consequently, this causes a reduction in the FOW for devices relying on DW propagation. However, the wire-width modulation also progressively suppresses the Walker breakdown resulting in a gradual increase in the Walker field, thereby enhancing the velocities of the DWs.

4.2 DW velocity diagrams

Having seen that the width modulation can increase the Walker field, we aim to identify wire-width-modulation parameters that keep the Walker breakdown field above the DW nucleation fields, allowing for steady DW motion throughout the FOW and full suppression of the Walker breakdown. A set of modulated wires with different thicknesses ranging from 5 to 30 nm were simulated to observe changes in DW propagation behavior with varying initial DW states for a fixed width and modulation period (150 nm average width and 50 nm period). Depending on the magnetic wire width and thickness, transverse and vortex DWs can be stable or metastable [39, 45]; larger width and thickness wires tend to support vortex domain walls or more complex multi-DW states [40, 207], while transverse DWs are stable for smaller widths and thicknesses. One might expect qualitatively different DW behavior in these geometries. The simulated DW velocities as a function of both the applied field and the wire thickness are shown in a color map in Figure 4.6 for the case of (a) 8% modulation and (b) no modulation. The boundaries of the DW depinning, new domain wall nucleation, and the onset of the Walker breakdown are indicated by the lines on the graph. Field values below the depinning field, where no DW propagation is observed, and above nucleation, where new undesirable DWs arise in the wire, are marked dark blue and dark red, respectively. The unmodulated wire demonstrates no pinning in the simulations and the Walker fields do not exceed 1 mT for all geometries and thus are not presented in the graph. In the case of modulated wires, the Walker fields can be outside the FOW, making their determination impossible.

One can observe a fast Walker field decay with increasing wire thickness and a correspond-

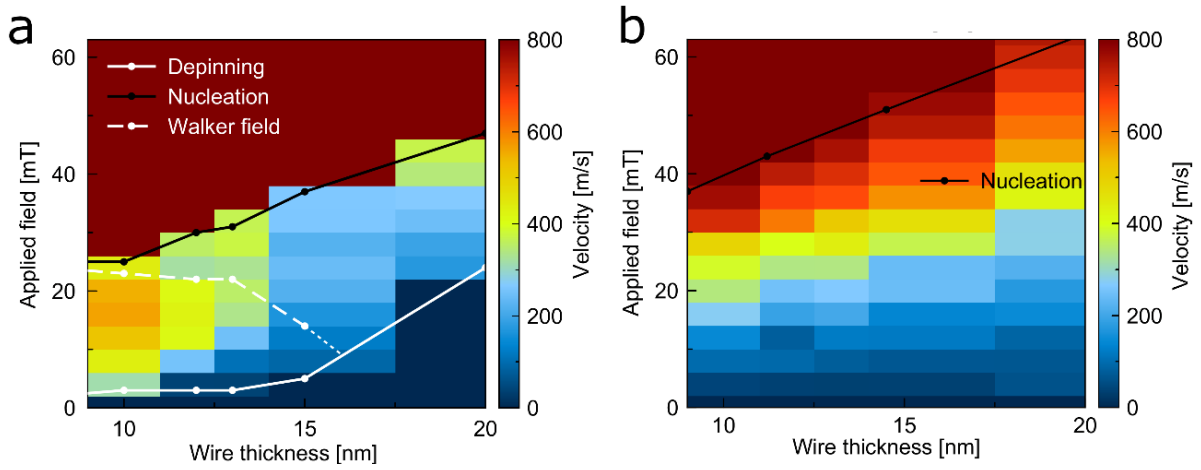

Figure 4.6: DW velocity colour maps vs. applied field and magnetic wire thickness, and DW nucleation, depinning and Walker fields plotted vs. magnetic wire thickness, for (a) width-modulated at fixed period (50 nm) and fixed amplitude (8%) and (b) unmodulated magnetic wires, the average wire width is 150 nm. Black lines depict the nucleation field for new DWs, solid white lines represent the depinning field and dashed white lines represent the Walker field. The unmodulated wire demonstrates no pinning in our simulations and the Walker fields do not exceed 1 mT for all geometries and thus are not presented in the graph.

ing reduction of the width-modulation efficiency for the modulated wire in Figure 4.6 a, while no change in the propagation mechanism is observed in Figure 4.6 b, depicting the case of unmodulated wires. This highlights a qualitative difference in the effect of width modulation on DW propagation for wires with different widths and thicknesses.

As mentioned before, according to the DW phase diagram [45], there are distinct ranges of permalloy wire widths and thicknesses providing stable transverse DWs (in the case of smaller widths and thicknesses) or vortex DWs (for larger widths and thicknesses). To separately investigate these two regimes, we simulated one set corresponding to energetically favorable transverse DWs (10 nm thickness, 100 nm width, 45-1000 nm modulation periods and 0-12% amplitudes) and a second set of simulations for stable vortex DWs (30 nm thickness, 200 nm width, 80-1000 nm modulation periods and 0-15% amplitudes).

Figure 4.7 illustrates the color-coded map of DW velocity in a magnetic wire with a thickness and width that supports stable transverse DWs as the lowest-energy static configuration (10 nm thick and 100 nm average width). Introducing a wire width modulation with increasing amplitude (Figure 4.7 a) gradually increases the depinning field and decreases the nucleation field of DWs, resulting in a decrease in the FOW of devices based on

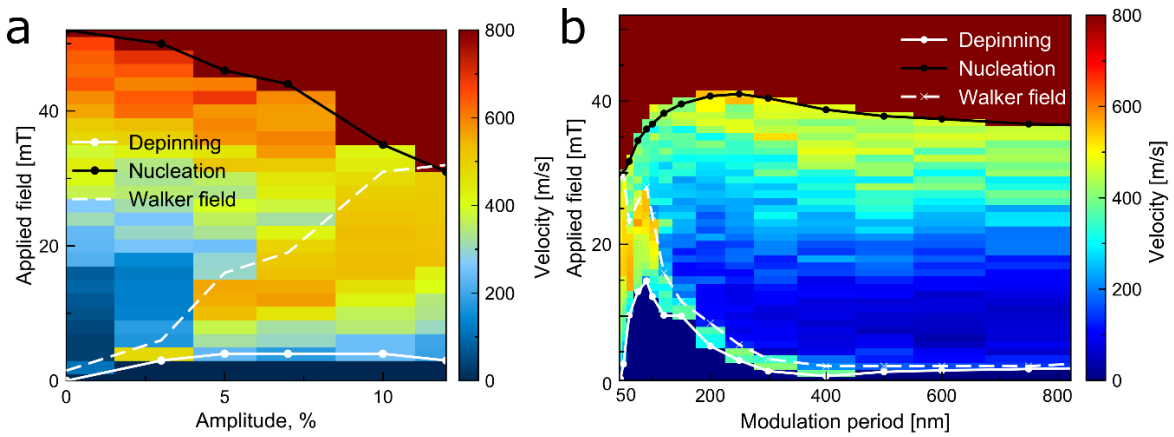

Figure 4.7: DW velocity colour maps vs. applied field and DW nucleation, depinning and Walker fields plotted vs. (a) width-modulation amplitude at fixed period (50 nm) and (b) width-modulation period at fixed amplitude (10%). The wire thickness is 10 nm and the average width is 100 nm. The initial domain wall configuration is a transverse DW, which remains stable below the Walker field.

DW propagation. However, the modulation also gradually suppresses the Walker breakdown (gradual rise of the Walker field), leading to an increase in DW velocities. In the region of high-amplitude wire-width modulation (10-12% on the graph), the Walker field is pushed beyond the nucleation field, resulting in steady DW propagation throughout the FOW with velocities higher than for an unmodulated wire (amplitude 0% on the graph). Therefore, the Walker breakdown is completely suppressed within the FOW. Figure 4.7 b demonstrates the DW velocities for different modulation periods at a fixed width modulation amplitude of 10%. For large modulation periods, we find a reduction of DW nucleation fields, which can be attributed to the introduction of narrow areas of extended lengths in the magnetic wires, while other DW behavior characteristics remain similar to the unmodulated wire (low depinning and Walker fields, similar values of DW velocities). For small modulation periods, a strong non-monotonicity in the dependence of nucleation, depinning, and Walker fields on the modulation period is observed. The FOW is strongly reduced, but the Walker field remains above the nucleation field, indicating the conservation of the DW spin structure within the FOW. For very small modulation periods of 45-50 nm, we find very low DW depinning fields that are beneficial for applications.

In contrast, Figure 4.8 illustrates the dynamics of DW propagation in thicker magnetic wires with larger widths. Notably, a distinct behavior is evident as there is no notable in-

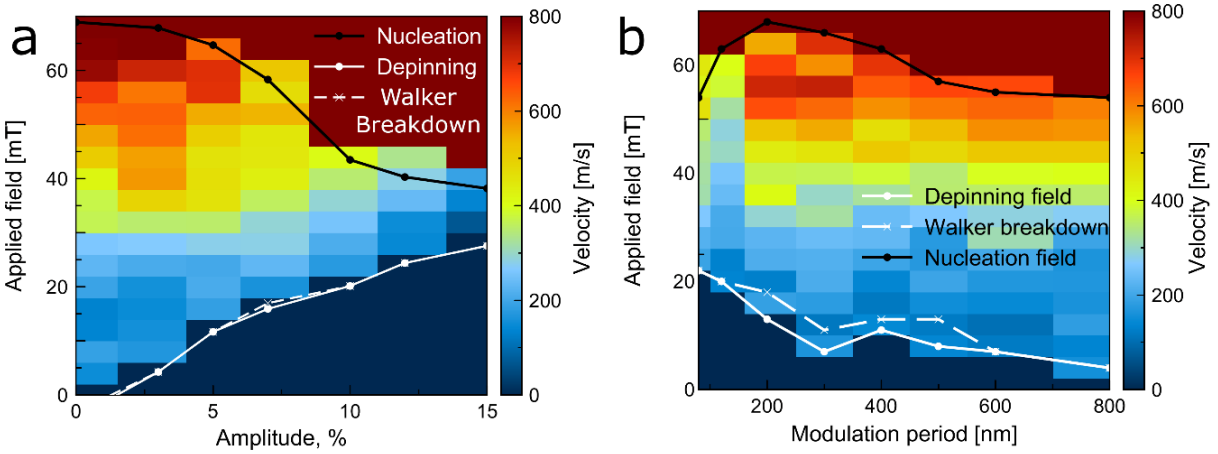

Figure 4.8: DW velocity colour maps vs. applied field and DW nucleation, depinning and Walker fields plotted vs. (a) width modulation amplitude at fixed period (80 nm) and (b) width modulation period at fixed amplitude (8%). The wire thickness is 30 nm and the average width is 200 nm. The initial domain wall configuration is a vortex DW, which remains stable below the Walker field.

crease in the Walker field due to the significantly larger depinning fields, which are either higher than or just below the Walker field for vortex walls. The nucleation fields exhibit a similar trend in relation to the wire width modulation amplitude as seen in the case of smaller widths and thicknesses. The impact of the DW slowdown caused by the wire width modulation is observable through the decreased velocities in regions of higher modulation amplitudes as shown in Figure 4.8 a and in areas of smaller modulation periods in Figure 4.8 b.

The observed DW propagation behavior in soft magnetic wires is in agreement with previous work [16–18]. Above the Walker field, the DW propagation becomes oscillatory with periodical reverse motion, and the Walker period, which characterizes the spin structure transformation length, becomes smaller with higher applied fields. The effect of the periodical wire width modulation can be understood as a result of introducing a spatially oscillating stray field energy that distorts the DW spin structure transformations [24,25,30], resulting in increasing Walker periods (Figure 4.5 a and 4.1 b). A width modulation with sufficient amplitude and a period smaller than the spin transformation length at a given field is found to suppress the Walker breakdown leading to steady DW propagation [28,30-32].

However, this simple description is clearly an oversimplification since the simulations here indicate a significant influence of the wire dimensions. For smaller widths and thick-

nesses, in the case of energetically favorable static transverse DW states, the periodical wire width modulation greatly affects the propagation and significantly helps to conserve the transverse DW structure. As a result, the Walker breakdown is pushed towards higher fields, enabling its full suppression within the FOW. One can find an optimal region of the wire width modulation period around 50 nm (Figure 4.6, 100 nm wire width, 10 nm wire thickness, and 10% modulation amplitude) corresponding to fully suppressed Walker breakdown and a gradually reduced effect at higher values (Figure 4.7).

Larger widths and thicknesses of magnetic wires provide larger nucleation fields and thus a larger FOW [10], which is desirable for many applications. However, we observe a significant rise in the depinning field when introducing the periodical wire-width modulation, which is either higher or similar to the rise in the Walker field. Thus, the wire width modulation does not provide any gain in the DW steady propagation field range.

Undesirable effects of the wire width modulation, such as the rise of the depinning field, reduction of the nucleation field, significantly reducing the FOW, and a smaller slope of the velocity/applied field curve (Figure 4.1 b) with increasing modulation amplitude, are observed for all wire geometries. These detrimental effects are minimal for large modulation periods where, due to the small edge curvature, the DW behavior resembles an unmodulated wire. Also, a significant reduction of the DW propagation fields for wires with smaller widths and thicknesses in the region of low modulation periods in Figure 4.7 b, enlarging the FOW is an important finding. The modulation period in this case is close to the DW width, which can be identified as a potential reason for the effect.

To summarize, the micromagnetic simulations reveal the impact of a wire-width modulation on the DW propagation in soft magnetic wires. Notable variations in the effectiveness of wire width modulation are contingent upon the widths and thicknesses of the wires. Particularly, for magnetic wires with smaller widths and thicknesses, which correspond to energetically favorable static transverse DWs, the introduction of periodic wire width modulation with adequate amplitude and a period smaller than the Walker period at a given field can effectively suppress the Walker breakdown. As a result, the DW propagation in magnetic wires and more intricate structures becomes faster and more reproducible.

4.3 DW propagation through a magnetic wire intersection

Magnetic wire intersections are critical elements for many device concepts with DW motion in planar structures. The intersection region can not only act as both a pinning and a nucleation center, but under certain conditions DWs propagating through wire intersections can undergo an undesired change of direction, which causes device failure. This DW behaviour is greatly affected by the DW spin structure. To study how the spin structure conservation via the periodic width modulation affects the DW propagation through such critical intersection regions, the DW propagation under an external field that is applied at different angles with respect to the longer arm of a cross of intersecting wires was investigated (Figure 4.9 a). The left arm of the cross structure is longer to initiate the DW propagation before it enters the intersection.

The initial magnetic state (t=0 s) of the investigated structures is presented in Figure 4.9 a for unmodulated and Figure 4.9 b for modulated wires. The average magnetic wire width is 100 nm, the thickness 10 nm, and the modulation period 50 nm with 10% amplitude in the case of the modulated wire. Possible outcomes of the DW propagation through the intersection are presented as selected snapshots and include successful propagation (Figure 4.9 c), DW pinning at the intersection, when the applied field strength is too low (Figure 4.9 d), new DW nucleation (Figure 4.9 e) and DW vertical deflection (Figure 4.9 f). For clarity, the simulation snapshots presented in figures Figure 4.9 c-f show only the results for the unmodulated wire cross - the magnetic configurations of the different possible scenarios are qualitatively the same for the modulated wire cross.

The compiled simulation results are presented in Figures 4.10 a and b. Yellow dots represent DW pinning, green successful propagation and red ones stand for device failure, i.e. DW nucleation or vertical arm reversal [10]. The green and red lines mark the lower (depinning) and higher (nucleation) FOW borders; the FOW in both cases is reduced compared to nonintersecting wires. The FOW borders mark the lowest applied field mag-

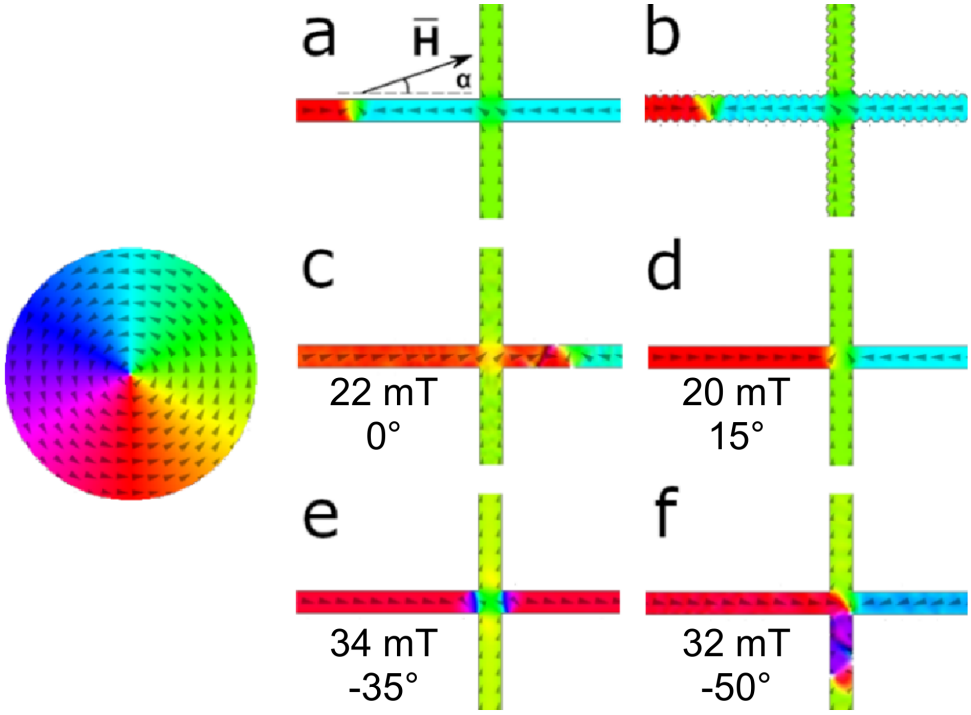

Figure 4.9: Exemplary snapshots of the DW propagation through a magnetic wire intersection under an external in-plane field H pointing at an angle α with respect to the horizontal arm: (a) initial state of the unmodulated structure (magnetisation up and left in the intersection and the TW in the longer arm of the cross), (b) initial state of the structure composed of width-modulated wires, and possible outcomes including (c) successful DW propagation through the cross, (d) DW pinning at the cross, (e) new DW nucleation at the cross and (f) vertical reversal of the DW propagation [10]

.

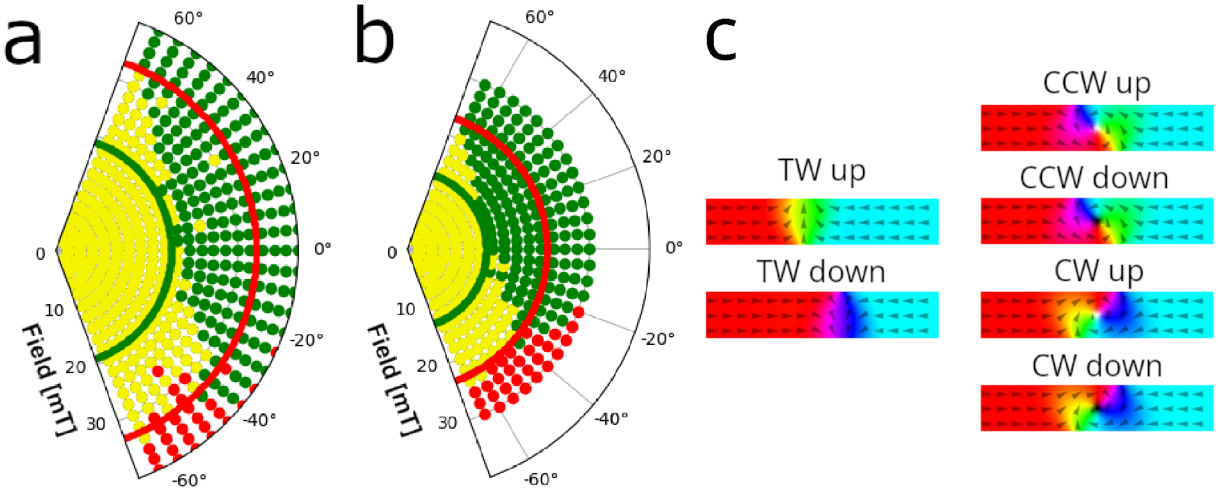

Figure 4.10: Simulation of the DW propagation through the intersection region results for intersections of (a) unmodulated and (b) modulated wires: DW pinning is marked in yellow, successful propagation is green, vertical reversal and nucleation are red. Depinning and nucleation fields are marked by the green and red lines correspondingly. (c) Sketch of the different DW chiralities in head-to-head DW configuration [208].

nitudes for successful DW propagation through the intersection as the depinning value, and for DW nucleation as the nucleation value. The FOW serves as a visual guide to the eye. In both cases the diagrams are not symmetric due to the vertical arm asymmetry.

An analysis of the chirality of the DWs propagating through the crosses reveals a strong dependence of the behaviour on the exact spin structure [209, 210]: transverse down and clockwise vortex walls are pinned at lower applied field values compared to counter-clockwise and transverse up DWs (Figure 4.10 c) which leads to DW propagation stochasticity in the unmodulated structure under applied fields in a positive direction in Figure 4.10. Vertical arm reversal or nucleation at higher fields can occur for counter-clockwise vortex walls. However, in contrast to the unmodulated wire cross, the modulated cross does not demonstrate vertical arm reversal in the whole FOW range. This is an additional important advantage of the width modulation, meaning that additional control over the applied field angle e. g. introducing syphons [10] is not required to ensure successful propagation across the intersection region.

The propagation of DWs through complex structures, such as notches, curved shapes, and wire intersections, is often highly unpredictable due to the way DW spin structures interact with the edges of magnetic wires. However, by suppressing the Walker breakdown and conserving the DW chirality, the typical stochasticity of DW propagation through these structures can be greatly reduced or eliminated entirely. In particular, research has shown [210] that the chirality of DWs plays a significant role in their behavior when passing through intersections of width-modulated magnetic wires. By controlling the DW chirality, the direction of propagation can be manipulated.

4.4 Experimental observation of the DW propagation

To investigate the DW velocities in magnetic wires experimentally, an experimental scheme utilizing Ørsted field pulses [211] was used. For this purpose, permalloy nanowires were patterned on top of a conductive Ørsted line. The material stack used for the sample and the Ørsted-line scheme are presented in Figure 4.11 a and b. Short current pulses were

applied through the Ørsted line, generating short field pulses parallel to the nanowires, thereby displacing the DWs (Figure 4.11 c).

The domain wall velocities were evaluated by analyzing static Kerr microscopy images before and after the pulses. Initially, the nanowires were saturated in the direction parallel to the wire and antiparallel to the Ørsted field pulses using an externally applied saturation field of 20 mT and a so-called background MOKE image was recorded. Then a small static magnetic field of 1 mT in the direction parallel to the Ørsted pulses was applied to nucleate a new domain in the nucleation pad and correspondingly create a new DW between the nucleation pad and the magnetic wire. Then in the absence of an external magnetic field a number (3-10) of short pulses (50 ns) was sent through the Ørsted line causing the DW to propagate along the magnetic wire. The subtraction of the background image from the Kerr microscopy image of the resulting magnetisation state provides information on the DW displacement and subsequently the DW velocity. Using this procedire, both the nucleation pads and the switched parts of the magnetic wires give contrast from the non-magnetic Ørsted line. The highlighted nucleation pads facilitate the identification of the small magnetic wires in the Kerr images (Figure 4.11 d, e and f). The DW depinning from the nucleation pads requires a higher magnetic field then the propagation through the wire, so for low fields (below 8 mT) a short depinning pulse (5 ns) was used to initiate the kinetic depinning and start the DW movement. A separate experiment was conducted utilizing only the depinning pulses and the obtained DW displacements were substracted during the DW velocity analysis.

Figure 4.12 shows a combined image of the patterned permalloy nanowires (in reality the wire separation is 4-6 μm) with different modulation periods and amplitudes. The bright lines at the wire edges result mainly from edge fencing of the structures. The average width of the wires is 200 nm, and the modulated width follows a sine curve: $w = w_{\mathrm{av}} \cdot (1 + 2a \cdot \sin(x))$, where w_{av} is the average width (200 nm) and a is the modulation amplitude (5% or 10%).

Figures 4.13 and 4.14 a show the dependence of the magnetic DW propagation velocities on the applied magnetic field for magnetic wires with different geometries, averaged over multiple (15-100) measurements. Magnetic DW propagation fields were determined as the

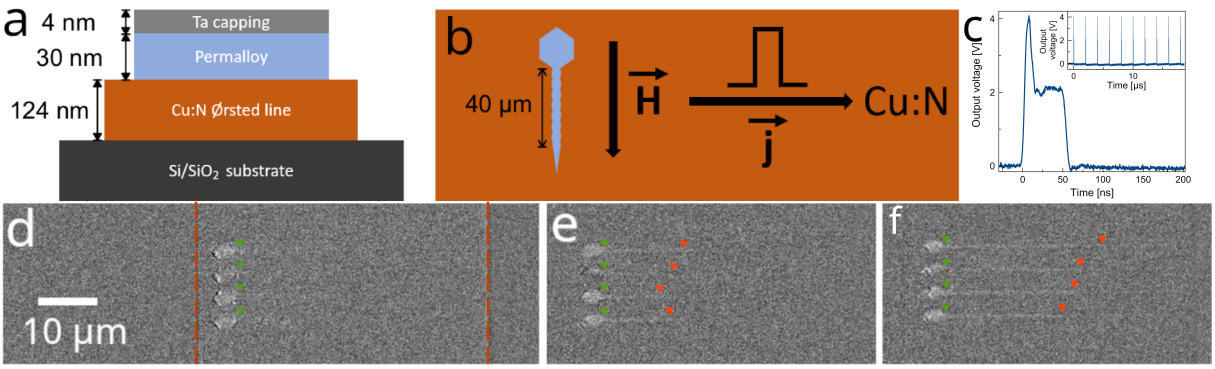

Figure 4.11: (a) Deposited material's stack for the studied samples, including the substrate, the Ørsted line, and the magnetic wire, and (b) scheme for the generation of short magnetic pulses (5-50 ns) in the Ørsted line showing a single Py wire with its nucleation pad on top. (c) DW displacement pulse shape and the whole sequence in the inset 10×[5 ns depinning + 50 ns displacement] (d-f) experimental Kerr images of four nominally identical permalloy nanowires. Orange dashed lines mark the edges of the Ørsted line, green arrows the beginning of the magnetic wire and red arrows – the shifted position of the DW. The magnetic configuration before the pulse is presented in (d), after the series of depinning pulses (10×5 ns) in (e) and after the displacement pulses in (f) correspondingly.

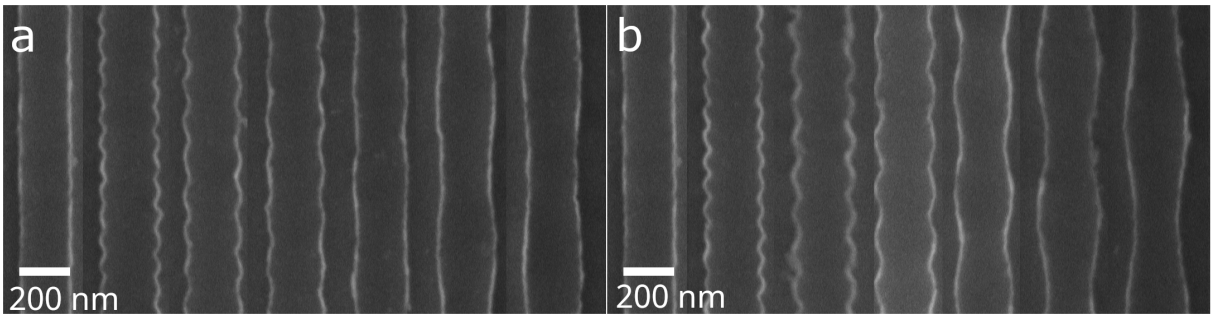

Figure 4.12: Scanning electron microscope images of the patterned permalloy wires on top of the Ørsted line with modulated widths of a modulation amplitude (a) 5% and (b) 10%.

minimal magnetic fields required to cause the DW displacement larger than the one caused solely by the depinning pulses. To determine the Walker fields both the DW-velocity trends and the standard deviation were analyzed, since above the Walker breakdown DW spin structure transformations take place, which reduces the DW velocity and increases its scatter.

The permalloy wires with smooth edges (200 nm wide, 30 nm thick, red line) show a rapid increase in the velocity until the Walker breakdown occurs, followed by a drastic drop, indicating the occurrence of oscillating DW propagation (red arrows). The Walker breakdown is also reflected in the increase in the standard deviation (Figure 4.13 a inset) due to the higher scatter of the DW displacement. In contrast, magnetic wires with mod-

ulated widths (200 nm average width, 30 nm thickness, 150 nm modulation period, 5% and 10% amplitude, green and blue lines, respectively) show smooth curves with shallow dips corresponding to the Walker breakdown (green and blue arrows).

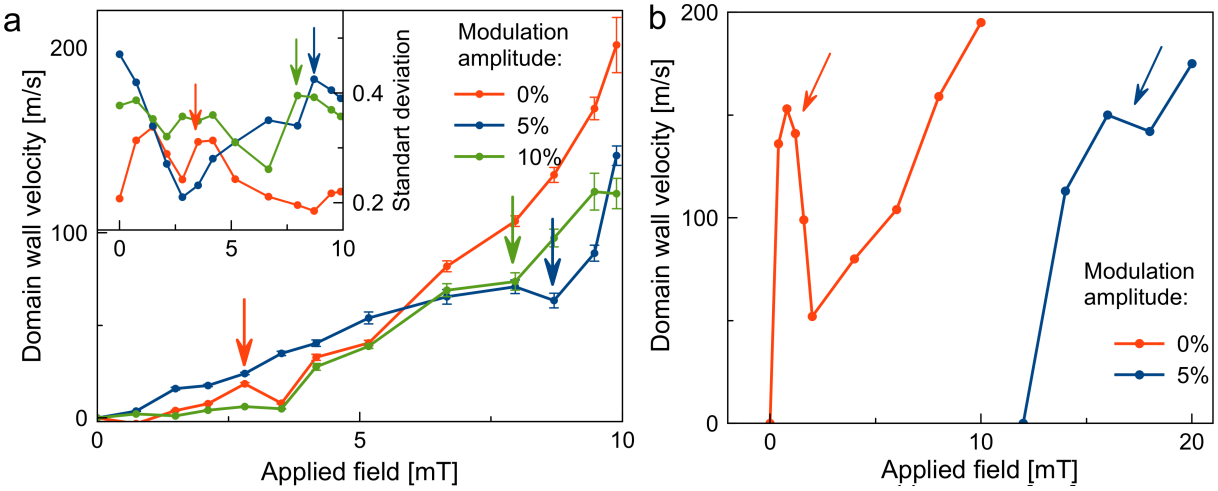

Figure 4.13: (a) Experimental results for the DW velocities vs. applied magnetic field for selected wires (200 nm average width, 30 nm thickness, 150 nm modulation period), the relative standard deviation is plotted in the inset. Arrows indicate the Walker field, above which DW spin structure transformations take place. (b) Room-temperature micromagnetic simulations of the DW velocities for these wires.

The DW velocities for the unmodulated and wire-width modulated wires shown in Figure 4.13 a exhibit qualitatively different behaviors in response to the applied magnetic fields. Micromagnetic simulations at 0 Kelvin yielded similar observations: introducing the wire width modulation on one hand reduces the DW nucleation field which is generally observed for narrower wires and on the other hand increases the depinning field forming an energy barrier. The periodical wire width modulation shifts the Walker breakdown towards higher applied magnetic fields (Figure 4.1). The velocity drop accompanying the Walker breakdown in the case of periodically modulated wires is shallower as the field range of the regime of oscillating motion is shrinking and with the sufficient modulation amplitude the Walker breakdown takes place between the fast steady and turbulent regimes.

Zero-temperature micromagnetic simulations for thicker and wider wires mimicking the experiment exhibit a dramatic rise of the depinning field with increasing modulation amplitude (Figure 4.8 a). For 5% amplitude the depinning field is 13 mT and for 10% it reaches 18 mT. For this reason, a set of room temperature micromagnetic simulations

was performed for two permalloy nanowires (200 average width, 30 nm thickness, 150 nm modulation period, 0% and 5% modulation amplitudes). The increased temperature conducts energy to the system and increases the probability of the DW to overcome the pinning energy barrier and to start the motion. Simulation results are presented in Figure 4.13 b. The unmodulated nanowire (red curve) demonstrates zero pinning due to the perfect smooth edges. The DW velocity rises fast and drops quickly after reaching the Walker breakdown. The DW in the periodically modulated wire (blue curve) is pinned up to 12 mT applied magnetic field. The DW velocity rises slower and the Walker-breakdown-associated velocity drop is negligible. Overall, the simulation results at 0 K and room temperature exhibit negligible differences.

The color maps in Figure 4.14 represent the DW velocities versus wire-width modulation-period data for the different magnetic wires studied in the experiment. The depinning field, which is the minimum field required to initiate DW propagation in a magnetic wire, is plotted as white dots in Figure 4.14. The Walker field is plotted as black dots. One can see an increase in the Walker field and a small increase in DW velocity corresponding to the DWs propagating in modulated wires with periods of 100 nm and 150 nm for both 5% and 10% modulation amplitudes. Increasing the modulation period leads to a gradual decrease of this effect. Larger modulation amplitudes result in an increase of the depinning field. The highest value of the Walker field is obtained for 150 nm modulation and 5% amplitude. Both increasing the modulation period and amplitude further decreases the Walker field.

The DW velocities and Walker field values are consistent with previously published data for similar permalloy wire geometries [47, 203]. We also observe the reported detrimental effect of an increase in the depinning field for larger modulation amplitudes due to the increasing pinning potential of the narrow regions of the wire, which disappears with increasing modulation periods [189] (Figure 4.14 b). The DW-velocity versus applied-field curves for modulated wires show characteristic hills followed by shallow pits instead of a sharp peak and a dramatic drops, indicating the Walker breakdown described in Ref. [189]. Micromagnetic simulations in Figure 4.13 b clearly show the difference in DW propagation mechanisms between the unmodulated and width-modulated wires. The un-

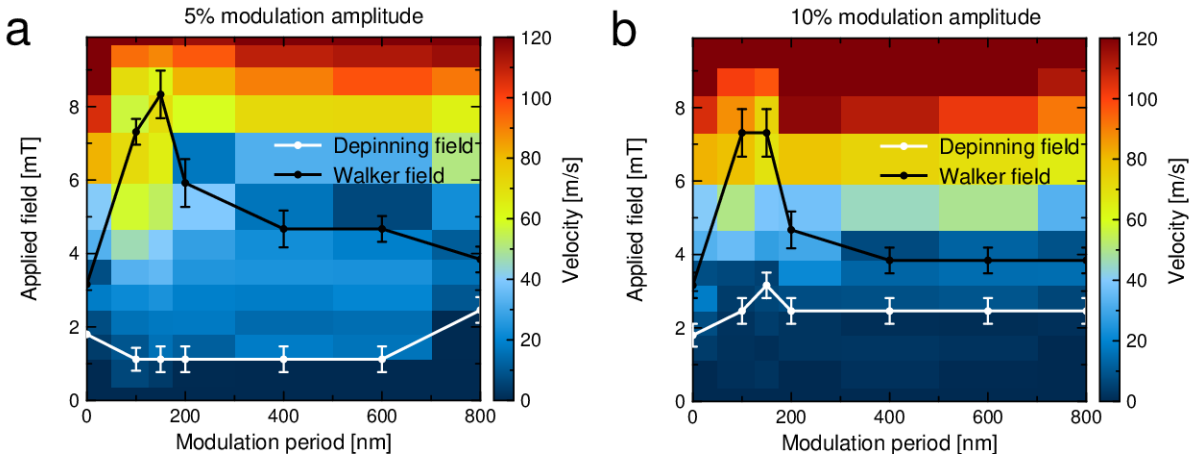

Figure 4.14: : DW-velocity color maps for modulated magnetic wires (200 nm average width, 30 nm thickness) vs. applied field and the wire-width modulation period with (a) 5% and (b) 10% modulation amplitude compiled from the field-pulse experiments in the Kerr microscope.

modulated wire exhibits the predicted Walker behavior, while the velocity versus applied field increase is suppressed by the wire edge modulation and the Walker breakdown is shifted towards higher fields. The occurrence of DW spin structure transformations is not accompanied by a significant drop in DW velocity.

The most efficient suppression of the Walker breakdown was achieved in simulations by using a modulation period close to the DW width in magnetic wires. For permalloy wires with a thickness and width of 30 nm and 200 nm, respectively, the stable vortex wall [45] size is about 200 nm [42], and the largest shift in the Walker field is indeed observed using 100-200 nm modulation periods.

DW logic applications [8] require fast DW propagation under controlled conditions which can be achieved close to the Walker breakdown which for real straight wires is very close or even below the depinning field. Introducing a slight periodical wire width modulation can increase the Walker field making the high-velocty DW field region applicable.

While there is qualitative agreement between the experimental results regarding the effect of periodical wire-width modulation on DW propagation in magnetic nanowires and the predictions from micromagnetic simulations, there are certain discrepancies. The lower experimental values for the Walker fields and domain wall velocities can be attributed to inevitable sample imperfections, such as finite grain size, surface and edge roughness, and voids, which can act as pinning centers and distort DW propagation. However, the observed depinning fields in the experiment are significantly lower than those even in the

room temperature simulations, which remains a surprising observation. Possible reasons for this discrepancy include the finite mesh size used in the simulations and the different approaches to kinetic depinning employed in the experiment (depinning voltage pulse) and simulations (acceleration track), possibly leading to these disparate results.

Summary and Outlook

This thesis provides an extensive investigation into the impact of varying the parameters of magnetron sputtering on the magnetic properties of Py (permalloy), in order to produce magnetically isotropic thin films with improved soft-magnetic properties. The findings indicate that the best samples with the lowest coercivity (as low as 0.01 mT) and vanishing average anisotropy are obtained using higher sputtering powers (1200 W) and low argon pressures ($4{\cdot}10^3$ mbar). This approach has resulted in the formation of denser and smoother films, a behaviour in line with previous observations on thin film growth [179].

A local variation of the magnetic properties of continuous Py films was observed, despite using the disorienting effects of sample rotation combined with a target tilt and the rotating external magnetic field. However, patterning these films into arrays of discs was found to suppress this variation, which suggests that random spurious defects have a dominant long-range influence on the magnetic properties of the films in unpatterned samples. Therefore, studying patterned samples provides a general and robust approach to investigate the intrinsic film properties, which can then be unambiguously related to variations in deposition conditions.

As a second part of the thesis, a comprehensive set of micromagnetic simulations to study the influence of a periodic wire-width modulation on the propagation of domain walls (DWs) in soft-magnetic wires was conducted. The simulations revealed key differences in the effectiveness of wire width modulation for wires with different widths and thicknesses, as these variations can lead to different types of DWs being energetically stable. In particular, it was found that for magnetic wires with smaller widths and thicknesses (100 and 10 nm respectively), corresponding to the energetically favorable transverse DWs,

that a periodic wire-width modulation with sufficient amplitude of 10% and a period (50 nm) smaller than the Walker period at a given field can fully suppress the Walker breakdown. This makes the DW propagation in magnetic wires and more complex structures faster and more reproducible. The results suggest that a periodic width modulation is a promising approach for improving the reliability of DW propagation in devices within an extended range of the field operating window (FOW).

Experimental studies were conducted on the propagation of DWs through periodically width-modulated soft magnetic wires. Using short magnetic pulses to move the DWs and Kerr microscopy to record their displacement, magnetic wires with different width modulation periods and amplitudes were examined. The velocities of DWs and the values of Walker fields align with previously published data for similar Py wire geometries [47, 203]. The negative impact of increasing depinning fields for larger modulation amplitudes was also observed. However, this effect is reduced with higher modulation periods. DW-velocity versus applied field curves for modulated wires exhibit characteristic shape [189]: the predicted Walker behavior is evident in unmodulated wires, while the width modulation suppresses the rise in velocity and shifts the Walker breakdown to higher fields, where the transformations in DW spin structure do not cause a significant drop in velocity.

The findings from this study have potential applications for practical device applications. Deposition patterns that result in smooth and dense Py films can be combined with various seed layers (such as NiCrFe [78], Pt [212], or CoFeB [213]) known to enhance the anisotropic magnetoresistance (AMR), thereby improving the performance of AMR-based devices. Moreover, the direct integration of optimized Py films as AMR sensors, along with investigating the integration of CMOS devices with such Py films, has shown feasibility. Promising results were achieved through the use of application-specific electronics provided by PREMA Semiconductor [214], where the magnetic functionality of the layers remained unaffected, and the sensor successfully operated using on-chip operational amplifiers for voltage measurement and on-chip current sources.

Preserving the DW spin structure in nanowires holds benefits for DW-based applications. Control over the DW chirality has proven crucial for effective DW propagation in real devices with intricate structures, including notches, curved shapes, and wire intersections, due to the interactions between DW spin structures and wire edges. By suppressing

the Walker breakdown and maintaining the DW chirality, the inherent stochasticity in DW propagation through these structures can be significantly reduced or eliminated altogether. Preserving transverse DWs in a closed-loop rotation sensor [10] aims to enhance the accuracy of DW propagation through intersection regions, as demonstrated by simulation results in this study, while also greatly reducing DW pinning in curved areas [53] such as syphons [10] or turns.

Bibliography

[1] G. E. Moore et al. *Cramming more components onto integrated circuits*. 1965.

[2] T. Shinjo. *Nanomagnetism and Spintronics*. Elsevier, 2013.

[3] M. N. Baibich et al. "Giant magnetoresistance of (001) Fe/(001) Cr magnetic superlattices". In: *Physical Review Letters* 61.21 (1988), p. 2472.

[4] S. D. Bader and S. S. P. Parkin. "Spintronics". In: *Annu. Rev. Condens. Matter Phys.* 1.1 (2010), pp. 71–88.

[5] P. Dey and J. N. Roy. *Spintronics*. Springer, 2021.

[6] O. Boulle, G. Malinowski and M. Kläui. "Current-induced domain wall motion in nanoscale ferromagnetic elements". In: *Materials Science and Engineering: R: Reports* 72.9 (2011), pp. 159–187.

[7] D. A. Allwood et al. "Magnetic Domain-Wall Logic". In: *Science* 309.5741 (2005), pp. 1688–1692.

[8] S. S. P. Parkin, M. Hayashi and L. Thomas. "Magnetic domain-wall racetrack memory". In: *Science* 320.5873 (2008), pp. 190–194.

[9] M. Diegel et al. "A new four bit magnetic domain wall based multiturn counter". In: *IEEE Transactions on Magnetics* 45.10 (2009), pp. 3792–3795.

[10] B. Borie et al. "Reliable propagation of magnetic domain walls in cross structures for advanced multiturn sensors". In: *Physical Review Applied* 8.4 (2017), p. 044004.

[11] C. Cui et al. "Maximized lateral inhibition in paired magnetic domain wall racetracks for neuromorphic computing". In: *Nanotechnology* 31.29 (2020), p. 294001.

[12] Y. Wang et al. "An energy-efficient nonvolatile in-memory computing architecture for extreme learning machine by domain-wall nanowire devices". In: *IEEE Transactions on Nanotechnology* 14.6 (2015), pp. 998–1012.

[13] R. Sbiaa. "Multistate magnetic domain wall devices for neuromorphic computing". In: *Physica Status Solidi (RRL)–Rapid Research Letters* 15.7 (2021), p. 2100125.

[14] K. Barmak and K. Coffey. *Metallic films for electronic, optical and magnetic applications: Structure, processing and properties*. Woodhead Publishing, 2014.

[15] H. N. Russell and F. A. Saunders. "New regularities in the spectra of the alkaline earths". In: *The Astrophysical Journal* 61 (1925), p. 38.

[16] W. Heisenberg. "Zur Theorie des Ferromagnetismus". In: *Original Scientific Papers Wissenschaftliche Originalarbeiten*. Springer, 1985, pp. 580–597.

[17] A. Aharoni et al. *Introduction to the Theory of Ferromagnetism*. Vol. 109. Clarendon Press, 2000.

[18] P. Weiss. "L'hypothèse du champ moléculaire et la propriété ferromagnétique". In: *J. Phys. Theor. Appl.* 6.1 (1907), pp. 661–690.

[19] F. Bloch. "Zur theorie des austauschproblems und der remanenzerscheinung der ferromagnetika". In: *Zur Theorie des Austauschproblems und der Remanenzerscheinung der Ferromagnetika*. Springer, 1932, pp. 295–335.

[20] L. Néel et al. "Magnetic surface anisotropy and superlattice formation by orientation. anisotropie magnétique superficielle et surstructures d'orientation p. 225". In: *Journal de Physique et le Radium* 15.4 (1954).

[21] L. Néel. "Energie des parois de Bloch dans les couches minces". In: *Comptes Rendus Hebdomadaires Des Seances De L Academie Des Sciences* 241.6 (1955), pp. 533–537.

[22] A. Hubert and R. Schäfer. *Magnetic domains: the analysis of magnetic microstructures*. Springer Science & Business Media, 2008.

[23] N. Wiese et al. "On the scaling behaviour of cross-tie domain wall structures in patterned NiFe elements". In: *EPL (Europhysics Letters)* 80.5 (2007), p. 57003.

[24] M. Prutton. *Thin ferromagnetic films*. Butterworths, 1964.

[25] E. Kondorsky. "On hysteresis in ferromagnetics". In: *J. Phys.(USSR)* 2.2 (1940), pp. 161–81.

[26] S. Chikazumi and C. D. Graham. *Physics of ferromagnetism*. 94. Oxford university press, 1997.

[27] E. C. Stoner and E. P. Wohlfarth. "A mechanism of magnetic hysteresis in heterogeneous alloys". In: *Philosophical Transactions of the Royal Society of London. Series A, Mathematical and Physical Sciences* 240.826 (1948), pp. 599–642.

[28] J. C. Slonczewski. "Research Memorandum RM 003.111. 224". In: *IBM Research Center Poughkeepsie* (1956).

[29] W. Wernsdorfer et al. "Magnetisation reversal by uniform rotation (Stoner–Wohlfarth model) in FCC cobalt nanoparticles". In: *Journal of Magnetism and Magnetic Materials* 242 (2002), pp. 132–138.

[30] J. L. F. Cuñado et al. "Emergence of the Stoner-Wohlfarth astroid in thin films at dynamic regime". In: *Scientific Reports* 7.1 (2017), pp. 1–9.

[31] L. D. Landau and E. M. Lifshitz. "On the Theory of the Dispersion of Magnetic Permeability in Ferromagnetic Bodies. Reproduced in Collected Papers of LD Landau". In: *Pergamon, New York* (1935).

[32] J. Fidler and T. Schrefl. "Micromagnetic modelling-the current state of the art". In: *Journal of Physics D: Applied Physics* 33.15 (2000), R135.

[33] M. Kläui. "Nanomagnetism of High-symmetry Magnetic Structures". PhD thesis. PhD thesis, University of Cambridge, 2003.

[34] T. L Gilbert. "A Lagrangian formulation of the gyromagnetic equation of the magnetization field". In: *Phys. Rev.* 100 (1955), p. 1243.

[35] D. J. Twisselmann and R. D. McMichael. "Intrinsic damping and intentional ferromagnetic resonance broadening in thin Permalloy films". In: *Journal of Applied Physics* 93.10 (2003), pp. 6903–6905.

[36] W. F. Brown Jr. "Domains, micromagnetics, and beyond: Reminiscences and assessments". In: *Journal of Applied Physics* 49.3 (1978), pp. 1937–1942.

[37] A. Thiaville and Y. Nakatani. "Micromagnetics of Domain Wall Dynamics in Soft Nanostrips". In: *Nanomagnetism and Spintronics*. Elsevier, 2014, pp. 261–313.

[38] R. D. McMichael and M. J. Donahue. "Head to head domain wall structures in thin magnetic strips". In: *IEEE Transactions on Magnetics* 33.5 (1997), pp. 4167–4169.

[39] M. Kläui. "Head-to-head domain walls in magnetic nanostructures". In: *Journal of Physics: Condensed Matter* 20.31 (2008), p. 313001.

[40] V. Estévez and L. Laurson. "Head-to-head domain wall structures in wide permalloy strips". In: *Physical Review B* 91.5 (2015), p. 054407.

[41] M. Laufenberg et al. "Observation of thermally activated domain wall transformations". In: *Applied Physics Letters* 88.5 (2006), p. 052507.

[42] V. D. Nguyen et al. "Third type of domain wall in soft magnetic nanostrips". In: *Scientific Reports* 5.1 (2015), pp. 1–7.

[43] A. Thiaville and Y. Nakatani. "Domain-wall dynamics in nanowiresand nanostrips". In: *Spin dynamics in confined magnetic structures III*. Springer, 2006, pp. 161–205.

[44] P. Krautscheid et al. "Domain wall spin structures in mesoscopic Fe rings probed by high resolution SEMPA". In: *Journal of Physics D: Applied Physics* 49.42 (2016), p. 425004.

[45] Y. Nakatani, A. Thiaville and J. Miltat. "Head-to-head domain walls in soft nanostrips: a refined phase diagram". In: *Journal of Magnetism and Magnetic Materials* 290 (2005), pp. 750–753.

[46] N. L. Schryer and L. R. Walker. "The motion of 180 domain walls in uniform dc magnetic fields". In: *Journal of Applied Physics* 45.12 (1974), pp. 5406–5421.

[47] G. S. D. Beach et al. "Dynamics of field-driven domain-wall propagation in ferromagnetic nanowires". In: *Nature Materials* 4.10 (2005), pp. 741–744.

[48] B. Borie et al. "Geometrical dependence of domain-wall propagation and nucleation fields in magnetic-domain-wall sensors". In: *Physical Review Applied* 8.2 (2017), p. 024017.

[49] M. Kläui et al. "Domain wall pinning in narrow ferromagnetic ring structures probed by magnetoresistance measurements". In: *Physical Review Letters* 90.9 (2003), p. 097202.

[50] M. Kläui et al. "Controlled magnetic switching in single narrow rings probed by magnetoresistance measurements". In: *Applied Physics Letters* 81.1 (2002), pp. 108–110.

[51] L. K. Bogart et al. "Dependence of domain wall pinning potential landscapes on domain wall chirality and pinning site geometry in planar nanowires". In: *Physical Review B* 79.5 (2009), p. 054414.

[52] D. Djuhana, Erwin Supriyanto and Dong Hyun Kim. "Micromagnetic simulation of the depinning field domain wall on symmetric double notch ferromagnetic wires". In: *Makara Journal of Science* (2014), pp. 42–46.

[53] S.–M. Ahn et al. "Geometric dependence of static and kinetic pinning of domain walls on ferromagnetic nanowires". In: *Journal of Applied Physics* 111.7 (2012), p. 07D309.

[54] M. Hayashi et al. "Dependence of current and field driven depinning of domain walls on their structure and chirality in permalloy nanowires". In: *Physical Review Letters* 97.20 (2006), p. 207205.

[55] D. Atkinson, D. S. Eastwood and L. K. Bogart. "Controlling domain wall pinning in planar nanowires by selecting domain wall type and its application in a memory concept". In: *Applied Physics Letters* 92.2 (2008), p. 022510.

[56] A. Himeno et al. "Domain wall ratchet effect in a magnetic wire with asymmetric notches". In: *Journal of Applied Physics* 103.7 (2008), 07E703.

[57] V. Mohanan and P. S. A. Kumar. "Chirality dependent pinning and depinning of magnetic vortex domain walls at nano-constrictions". In: *Journal of Magnetism and Magnetic Materials* 422 (2017), pp. 419–424.

[58] D. M. Burn et al. "Dynamic interaction between domain walls and nanowire vertices". In: *Physical Review B* 90.14 (2014), p. 144414.

[59] J. Leliaert et al. "Influence of material defects on current-driven vortex domain wall mobility". In: *Physical Review B* 89.6 (2014), p. 064419.

[60] P. J. Metaxas et al. "Creep and flow regimes of magnetic domain-wall motion in ultrathin Pt/Co/Pt films with perpendicular anisotropy". In: *Physical Review Letters* 99.21 (2007), p. 217208.

[61] E. R. Lewis et al. "Magnetic domain wall pinning by a curved conduit". In: *Applied Physics Letters* 95.15 (2009), p. 152505.

[62] P. Ripka. *Magnetic sensors and magnetometers*. Artech house, 2021.

[63] J. E. Lenz. "A review of magnetic sensors". In: *Proceedings of the IEEE* 78.6 (1990), pp. 973–989.

[64] M. A. Khan et al. "Magnetic sensors-A review and recent technologies". In: *Engineering Research Express* 3.2 (2021), p. 022005.

[65] H. Hauser et al. “Magnetoresistive Sensors”. In: *Proceedings of a Workshop at the Vienna University of Technology*. Institute of Industrial Electronics and Material Science Technische Universität Wien. 2000, p. 15.

[66] C. Fermon and M. Pannetier-Lecoeur. *Giant Magnetoresistance (GMR) sensors, from Basis to State-of-the-Art applications (eds Reig, C. et al.), 47–70*. 2013.

[67] K. Fuchs. “The conductivity of thin metallic films according to the electron theory of metals”. In: *Mathematical Proceedings of the Cambridge Philosophical Society*. Vol. 34. 1. Cambridge University Press. 1938, pp. 100–108.

[68] E. H. Sondheimer. “The mean free path of electrons in metals”. In: *Advances in Physics* 50.6 (2001), pp. 499–537.

[69] A. F. Mayadas, J. F. Janak and A. Gangulee. “Resistivity of Permalloy thin films”. In: *Journal of Applied Physics* 45.6 (1974), pp. 2780–2781.

[70] A. F. Mayadas and M. Shatzkes. “Electrical-resistivity model for polycrystalline films: the case of arbitrary reflection at external surfaces”. In: *Physical Review B* 1.4 (1970), p. 1382.

[71] L. J. van der Pauw. “A method of measuring the resistivity and Hall coefficient on lamellae of arbitrary shape”. In: *Philips technical review* 20 (1958), pp. 220–224.

[72] M. Kateb, E. Jacobsen and S. Ingvarsson. “Application of an extended van der Pauw method to anisotropic magnetoresistance measurements of ferromagnetic films”. In: *Journal of Physics D: Applied Physics* 52.7 (2018), p. 075002.

[73] A. Grosz et al. “Planar hall effect sensors with subnanotesla resolution”. In: *IEEE Magnetics Letters* 4 (2013), pp. 6500104–6500104.

[74] W. Thomson. “XIX. On the electro-dynamic qualities of metals:—Effects of magnetization on the electric conductivity of nickel and of iron”. In: *Proceedings of the Royal Society of London* 8 (1857), pp. 546–550.

[75] J. Smit. “Magnetoresistance of ferromagnetic metals and alloys at low temperatures”. In: *Physica* 17.6 (1951), pp. 612–627.

[76] T. McGuire and R. L. Potter. “Anisotropic magnetoresistance in ferromagnetic 3d alloys”. In: *IEEE Transactions on Magnetics* 11.4 (1975), pp. 1018–1038.

[77] V. Mor, A. Grosz and L. Klein. “Planar Hall effect (PHE) magnetometers”. In: *High Sensitivity Magnetometers*. Springer, 2017, pp. 201–224.

[78] W. Y. Lee, M. F. Toney and D. Mauri. "High magnetoresistance in sputtered Permalloy thin films through growth on seed layers of $(Ni_{0.81}Fe_{0.19})_{1-x}Cr_x$". In: *IEEE transactions on magnetics* 36.1 (2000), pp. 381–385.

[79] G. Binasch et al. "Enhanced magnetoresistance in layered magnetic structures with antiferromagnetic interlayer exchange". In: *Physical Review B* 39.7 (1989), p. 4828.

[80] S. S. P. Parkin. "Giant magnetoresistance in magnetic nanostructures". In: *Annual Review of Materials Science* 25.1 (1995), pp. 357–388.

[81] N. F. Mott. "Electrons in transition metals". In: *Advances in Physics* 13.51 (1964), pp. 325–422.

[82] H. Corte-León et al. "Influence of geometry on domain wall dynamics in Permalloy nanodevices". In: *IEEE Transactions on Magnetics* 51.1 (2015), pp. 1–4.

[83] M. A. Bashir et al. "Remote domain wall chirality measurement via stray field detection". In: *Journal of Applied Physics* 110.12 (2011), p. 123912.

[84] *Novotechnik Rotary Sensors Multi Turn*. URL: `https://www.novotechnik.de/en/products/rotary-sensors-linear-position-transducer`.

[85] *Multiturn Position Sensor Provides True Power-On Capabilities with Zero Power*. URL: `https://www.analog.com/en/analog-dialogue/articles/multiturn-position-sensor-provides-true-power-on-capabilities-with-zero-power.html`.

[86] R. Mattheis et al. "Concepts and steps for the realization of a new domain wall based giant magnetoresistance nanowire device: From the available 24 multiturn counter to a 212 turn counter". In: *Journal of Applied Physics* 111.11 (2012), p. 113920.

[87] H. D. Arnold and G. W. Elmen. "Permalloy, a new magnetic material of very high permeability". In: *Bell System Technical Journal* 2.3 (1923), pp. 101–111.

[88] E. T. Ferguson. "Uniaxial magnetic anisotropy induced in Fe–Ni alloys by magnetic anneal". In: *Journal of Applied Physics* 29.3 (1958), pp. 252–253.

[89] R. M. Bozorth. *Magnetic Properties of Metals and Alloys*. American Society for Metals, 1959.

[90] M. S. Blois Jr. "Preparation of thin magnetic films and their properties". In: *Journal of Applied Physics* 26.8 (1955), pp. 975–980.

[91] P. E. Tannenwald and M. H. Seavey Jr. "Ferromagnetic resonance in thin films of Permalloy". In: *Physical Review* 105.2 (1957), p. 377.

[92] D. O. Smith. "Static and dynamic behavior of thin permalloy films". In: *Journal of Applied Physics* 29.3 (1958), pp. 264–273.

[93] P. Bruno. "Tight-binding approach to the orbital magnetic moment and magnetocrystalline anisotropy of transition-metal monolayers". In: *Physical Review B* 39.1 (1989), p. 865.

[94] D. O. Smith. "Anisotropy in permalloy films". In: *Journal of Applied Physics* 30.4 (1959), S264–S265.

[95] M. Kateb et al. "Comparison of magnetic and structural properties of permalloy $Ni_{80}Fe_{20}$ grown by dc and high power impulse magnetron sputtering". In: *Journal of Physics D: Applied Physics* 51.28 (2018), p. 285005.

[96] E. Fuchs and W. Zinn. "Isotropic permalloy films". In: *Journal of Applied Physics* 34.9 (1963), pp. 2557–2562.

[97] T. G. Knorr and R. W. Hoffman. "Dependence of geometric magnetic anisotropy in thin iron films". In: *Physical Review* 113.4 (1959), p. 1039.

[98] T. Iwata and F. B. Hagedorn. "Annealing behavior of induced anisotropy and related magnetic properties in Permalloy films". In: *Journal of Applied Physics* 40.5 (1969), pp. 2258–2266.

[99] S. Chikazumi and T. Oomura. "On the origin of magnetic anisotropy induced by magnetic annealing". In: *Journal of the Physical Society of Japan* 10.10 (1955), pp. 842–849.

[100] S. Chikazumi. "Ferromagnetic properties and superlattice formation of iron nickel alloys (I)". In: *Journal of the Physical Society of Japan* 5.5 (1950), pp. 327–333.

[101] C. M. Williams. "Effects of ^{3}He Irradiation on the Anisotropy-Field Inhomogeneity and Coercive Force in Thin Permalloy Films". In: *Journal of Applied Physics* 39.10 (1968), pp. 4741–4744.

[102] S. Yaegashi, T. Kurihara and H. Segawa. "Epitaxial growth and magnetic properties of Fe (211)". In: *Journal of Applied Physics* 74.7 (1993), pp. 4506–4512.

[103] M. S. Cohen. "Oblique-Incidence Magnetic Anisotropy in Codeposited Alloy Films". In: *Journal of Applied Physics* 38.2 (1967), pp. 860–869.

[104] C. H. Wilts and F. B. Humphrey. "Magnetic anisotropy in flat ferromagnetic films: a review". In: *Journal of Applied Physics* 39.2 (1968), pp. 1191–1196.

[105] E. J. Torok. "Origin and effects of local regions of complex biaxial anisotropy in thin ferromagnetic films with uniaxial anisotropy". In: *Journal of Applied Physics* 36.3 (1965), pp. 952–960.

[106] J. R. Kench and S. B. Schuldt. "Concerning the origin of uniaxial magnetic anisotropy in electrodeposited permalloy films". In: *Journal of Applied Physics* 41.8 (1970), pp. 3338–3346.

[107] M. Kateb and S. Ingvarsson. "Correlation of uniaxial magnetic anisotropy axes and principal resistivities in polycrystalline ferromagnetic films". In: *Journal of Magnetism and Magnetic Materials* 532 (2021), p. 167982.

[108] B. D. Cullity and C. D. Graham. *Introduction to magnetic materials*. John Wiley & Sons, 2011.

[109] M. Masuda, S. Uchiyama and Y. Sakaki. "Temperature dependence of uniaxial anisotropy and anisotropy dispersion in Ni-Fe thin films". In: *Japanese Journal of Applied Physics* 5.8 (1966), p. 726.

[110] F. G. West and C. L. Simmons. "Dependence of angular dispersion on grain size in evaporated permalloy films". In: *Journal of Applied Physics* 37.3 (1966), pp. 1283–1284.

[111] W. R. Grove. "VII. On the electro-chemical polarity of gases". In: *Philosophical Transactions of the Royal Society of London* 142 (1852), pp. 87–101.

[112] K. Wasa and S. Hayakawa. "Handbook of sputter deposition technology". In: (1992).

[113] P. Sigmund. "Theory of sputtering. I. Sputtering yield of amorphous and polycrystalline targets". In: *Physical Review* 184.2 (1969), p. 383.

[114] G. K. Wehner, C. Kenknight and D. L. Rosenberg. "Sputtering rates under solar-wind bombardment". In: *Planetary and Space Science* 11.8 (1963), pp. 885–895.

[115] D. E. Harrison Jr et al. "Computer simulation of sputtering". In: *Journal of Applied Physics* 39.8 (1968), pp. 3742–3761.

[116] D. E. Harrison Jr and C. B. Delaplain. "Computer simulation of the sputtering of clusters". In: *Journal of Applied Physics* 47.6 (1976), pp. 2252–2259.

[117] P. Dimitrakis, E. Valov and S. Tappertzhofen. *Metal Oxides for Non-Volatile Memory*. 2021.

[118] O. A. Streletskiy et al. "Magnetron deposition of aC: ND coatings by nanodiamond transfer: pulse number impact on aggregation and graphitization". In: *Applied Physics A* 128 (2022), pp. 1–8.

[119] R. V. Stuart. *Vacuum technology, thin films, and sputtering: an introduction*. Academic Press, 2012.

[120] *Singulus Technologies. Rotaris, Universal Sputtering System*. URL: `https://www.singulus.de/de/rotaris.html`.

[121] P. N. Solovev, A. V. Izotov and B. A. Belyaev. "Microstructural and magnetic properties of thin obliquely deposited films: A simulation approach". In: *Journal of Magnetism and Magnetic Materials* 429 (2017), pp. 45–51.

[122] B. L. Flur and J. Riseman. "Preparation of Uniaxial Permalloy Films by Cathodic Sputtering on Glass and Metal Substrates". In: *Journal of Applied Physics* 35.2 (1964), pp. 344–347.

[123] N. Kaiser. "Review of the fundamentals of thin-film growth". In: *Applied optics* 41.16 (2002), pp. 3053–3060.

[124] M. Volmer and A. Weber. "Novel growth mechanism in heteroepitaxial semiconductor growth". In: *Z. phys. Chem* 119 (1926), p. 277.

[125] J. Venables. *Introduction to surface and thin film processes*. Cambridge university press, 2000.

[126] H. L. Seet et al. "Effect of deposition methods on the magnetic properties of nanocrystalline permalloy". In: *Journal of alloys and compounds* 449.1-2 (2008), pp. 284–287.

[127] Kh. Gheisari, Sh. Shahriari and S. Javadpour. "Structural evolution and magnetic properties of nanocrystalline 50 Permalloy powders prepared by mechanical alloying". In: *Journal of Alloys and Compounds* 574 (2013), pp. 71–82.

[128] B. A. Movchan and A. V. Demchishin. "Structure and properties of thick condensates of Nickel, Titanium, Tungsten, Aluminum oxides, and Zircnium dioxide in vacuum". In: *Fiz. Metal. Metalloved. 28: 653-60 (Oct 1969)*. (1969).

[129] J. A Thornton. “Influence of substrate temperature and deposition rate on structure of thick sputtered Cu coatings”. In: *Journal of Vacuum Science and Technology* 12.4 (1975), pp. 830–835.

[130] E. Kusano. “Structure-zone modeling of sputter-deposited thin films: a brief review”. In: *Applied Science and Convergence Technology* 28.6 (2019), pp. 179–185.

[131] Y.-S. Chaug and D. L. Williamson. “Sputter-induced changes in permalloy target microstructure”. In: *Journal of Vacuum Science & Technology A: Vacuum, Surfaces, and Films* 9.3 (1991), pp. 505–509.

[132] M. S. Sultan. “Effect of gas pressure and flow rate on the plasma power and deposition rate in magnetron sputtering system”. In: *Res. J. Nanosci. Eng* 2 (2018), pp. 1–8.

[133] S. Kezilebieke et al. “Magnetic properties of ultrathin $Ni_{81}Fe_{19}$ films with Ta and Ru capping layers”. In: *Journal of Physics: Condensed Matter* 25.47 (2013), p. 476003.

[134] M. Kowalewski et al. “The effect of Ta on the magnetic thickness of permalloy (Ni 81 Fe 19) films”. In: *Journal of Applied Physics* 87.9 (2000), pp. 5732–5734.

[135] D. Schönke. “Static and Dynamic Magnetic Imaging of Diffent Magnetic Materials Using Scanning Electron Microscopy with Polarization Analysis”. PhD thesis. Mainz, 2021.

[136] L. G Parratt. “Surface studies of solids by total reflection of X-rays”. In: *Physical Review* 95.2 (1954), p. 359.

[137] H. Kiessig. “Interferenz von Röntgenstrahlen an dünnen Schichten”. In: *Annalen der Physik* 402.7 (1931), pp. 769–788.

[138] A. M. Miller et al. “Extracting information from X-ray diffraction patterns containing Laue oscillations”. In: *Zeitschrift für Naturforschung B* 77.4-5 (2022), pp. 313–322.

[139] A. Glavic and M. Björck. “GenX 3: the latest generation of an established tool”. In: *Journal of Applied Crystallography* 55.4 (2022).

[140] G. Binnig et al. “Surface studies by scanning tunneling microscopy”. In: *Physical Review Letters* 49.1 (1982), p. 57.

[141] G. Binnig, C. F. Quate and Ch. Gerber. "Atomic force microscope". In: *Physical Review Letters* 56.9 (1986), p. 930.

[142] M. Ohring. *Materials science of thin films: depositon & structure*. Elsevier, 2001.

[143] D. Nečas and P. Klapetek. "Gwyddion: an open-source software for SPM data analysis". In: *Open Physics* 10.1 (2012), pp. 181–188.

[144] C.-H. Lee et al. "a Comparison Between the Atomic Force Microscopy and X-Ray Reflectivity on the Characterization of Surface Roughness". In: *International Journal of Nanoscience* 2.04n05 (2003), pp. 343–348.

[145] C.-H. Lee et al. "The Coherent Limitation of the Specular X-ray and Neutron Reflectivity on the Characterization of the Physical Vapor Deposition Thin Films". In: *Chinese Journal of Physics* 50.2 (2012), pp. 301–310.

[146] H.-C. Su et al. "A comparison between X-ray reflectivity and atomic force microscopy on the characterization of a surface roughness". In: *Chinese Journal of Physics* 50.2 (2012), pp. 291–300.

[147] P. Scherrer. *Göttinger Nachrichten Gesell., vol. 2*. 1918.

[148] J. I. Langford and A. J. C. Wilson. "Scherrer after sixty years: a survey and some new results in the determination of crystallite size". In: *Journal of Applied Crystallography* 11.2 (1978), pp. 102–113.

[149] C. G. Willson, R. R. Dammel and A. Reiser. "Photoresist materials: a historical perspective". In: *Metrology, Inspection, and Process Control for Microlithography XI*. Vol. 3050. SPIE. 1997, pp. 38–51.

[150] Microresist Technology, ed. *ma-P 1200 Serie / ma-P 1275HV*. URL: `https://www.microresist.de/produkt/ma-p-1200-series-ma-p-1275-hv/`.

[151] Allresist GmbH, ed. *E-Beam Resist AR-N 7520 series*. URL: `https://www.allresist.com/portfolio-item/e-beam-resist-ar-n-7520-series/`.

[152] V. T. Cherepin. *Secondary ion mass spectroscopy of solid surfaces*. VSP, 1987.

[153] R. M. Reeve et al. "Scaling of intrinsic domain wall magnetoresistance with confinement in electromigrated nanocontacts". In: *Physical Review B* 99.21 (2019), p. 214437.

[154] S. Foner. "Versatile and sensitive vibrating-sample magnetometer". In: *Review of Scientific Instruments* 30.7 (1959), pp. 548–557.

[155] I. V. Soldatov and R. Schäfer. "Selective sensitivity in Kerr microscopy". In: *Review of Scientific Instruments* 88.7 (2017), p. 073701.

[156] J. Kerr. "XLIII. On rotation of the plane of polarization by reflection from the pole of a magnet". In: *The London, Edinburgh, and Dublin Philosophical Magazine and Journal of Science* 3.19 (1877), pp. 321–343.

[157] S. Polisetty et al. "Optimization of magneto-optical Kerr setup: Analyzing experimental assemblies using Jones matrix formalism". In: *Review of Scientific Instruments* 79.5 (2008), p. 055107.

[158] A. Green and M. Prutton. "Magneto-optic detection of ferromagnetic domains using vertical illumination". In: *Journal of Scientific Instruments* 39.5 (1962), p. 244.

[159] K. A. Thórarinsdóttir et al. "Finding order in disorder: Magnetic coupling distributions and competing anisotropies in an amorphous metal alloy". In: *APL Materials* 10.4 (2022), p. 041103.

[160] M. T. Johnson et al. "Magnetic anisotropy in metallic multilayers". In: *Reports on Progress in Physics* 59.11 (1996), p. 1409.

[161] M. Dumm et al. "Magnetism of ultrathin FeCo (001) films on GaAs (001)". In: *Journal of Applied Physics* 87.9 (2000), pp. 5457–5459.

[162] K. Wang et al. "Investigation of magnetic properties in thick CoFeB alloy films for controllable anisotropy". In: *Applied Physics A* 122 (2016), pp. 1–5.

[163] R. P. Feynman, R. B. Leighton and M. Sands. *The Feynman lectures on physics, V. 1, 2.5, 2.6. Electricity and magnetism*. 1966.

[164] NT-MDT spectrum instruments, ed. *2.7.9 MAGNETIC FIELD OF RECTANGULAR CONDUCTOR WITH CURRENT*. URL: `https://www.ntmdt-si.com/resources/spm-theory/theoretical-background-of-spm/2-scanning-force-microscopy-(sfm)/27-magnetic-force-microscopy-quantitative-results-treatment/279-magnetic-field-of-rectangular-conductor-with-current`.

[165] A. Vansteenkiste et al. "The design and verification of MuMax3". In: *AIP Advances* 4.10 (2014), p. 107133.

[166] R. J. LeVeque. "Finite difference methods for differential equations". In: *Draft version for use in AMath* 585.6 (1998), p. 112.

[167] W. F. Brown Jr. "Thermal fluctuations of a single-domain particle". In: *Physical Review* 130.5 (1963), p. 1677.

[168] J. H Mathews, Kurtis D Fink et al. *Numerical methods using MATLAB*. Vol. 4. Pearson prentice hall Upper Saddle River, NJ, 2004.

[169] S. Ingvarsson et al. "Role of electron scattering in the magnetization relaxation of thin $Ni_{81}Fe_{19}$ films". In: *Physical Review B* 66.21 (2002), p. 214416.

[170] G. S. Abo et al. "Definition of magnetic exchange length". In: *IEEE Transactions on Magnetics* 49.8 (2013), pp. 4937–4939.

[171] D. Schönke et al. "Magnetic state control via field-angle-selective switching in asymmetric rings". In: *Physical Review Applied* 14.3 (2020), p. 034028.

[172] Z. Wang et al. "Highly sensitive flexible magnetic sensor based on anisotropic magnetoresistance effect". In: *Advanced Materials* 28.42 (2016), pp. 9370–9377.

[173] T. Griesbach, M. C. Wurz and L. Rissing. "Design, fabrication, and testing of a modular magnetic field microsensor on a flexible polymer foil". In: *IEEE Transactions on Magnetics* 48.11 (2012), pp. 3843–3846.

[174] G. Choe and M. Steinback. "Surface roughness effects on magnetoresistive and magnetic properties of NiFe thin films". In: *Journal of Applied Physics* 85.8 (1999), pp. 5777–5779.

[175] S. Cercelaru et al. "A comparative study of the magnetic properties of thin permalloy films". In: *Journal of Magnetism and Magnetic Materials* 160 (1996), pp. 338–340.

[176] N. Djuzhev et al. "Effects of average grain size on the magnetic properties of permalloy films". In: *EPJ Web of Conferences*. Vol. 185. EDP Sciences. 2018, p. 01003.

[177] M. A. Akhter et al. "Thickness and grain-size dependence of the coercivity in permalloy thin films". In: *Journal of Applied Physics* 81.8 (1997), pp. 4122–4124.

[178] K. Glasner et al. "Ostwald ripening of droplets: the role of migration". In: *European journal of Applied Mathematics* 20.1 (2009), pp. 1–67.

[179] C. V. Thompson. "Structure evolution during processing of polycrystalline films". In: *Annual Review of Materials Science* 30.1 (2000), pp. 159–190.

[180] A. Gentils et al. “Variation of domain-wall structures and magnetization ripple spectra in permalloy films with controlled uniaxial anisotropy”. In: *Journal of Applied Physics* 98.5 (2005), p. 053905.

[181] H. Hoffmann. “Theory of magnetization ripple”. In: *IEEE Transactions on Magnetics* 4.1 (1968), pp. 32–38.

[182] K. J. Harte. “Theory of magnetization ripple in ferromagnetic films”. In: *Journal of Applied Physics* 39.3 (1968), pp. 1503–1524.

[183] T. Ried and P. Tsatsoulis. “Universality of the magnetization ripple (03.03. 2021)”. In: ().

[184] R. H. Wade. “Some factors in the easy axis magnetization of permalloy films”. In: *Philosophical Magazine* 10.103 (1964), pp. 49–66.

[185] V. P. Panaetov. “Magnetic Structure of Thin Permalloy Films with Interacting Domain Walls”. In: *Physics of Metals and Metallography* 121.5 (2020), pp. 412–415.

[186] M. Schneider et al. “Stability of magnetic vortices in flat submicron permalloy cylinders”. In: *Journal of Applied Physics* 92.3 (2002), pp. 1466–1472.

[187] M. Kateb and S. Ingvarsson. “Thickness-dependent magnetic and magnetoresistance properties of permalloy prepared by field assisted tilt sputtering”. In: *2017 IEEE Sensors Applications Symposium (SAS)*. IEEE. 2017, pp. 1–5.

[188] R. Ferrero et al. “Influence of shape, size and magnetostatic interactions on the hyperthermia properties of permalloy nanostructures”. In: *Scientific Reports* 9.1 (2019), pp. 1–12.

[189] O. Lozhkina et al. “Control of the Walker breakdown by periodical magnetic wire-width modulation”. In: *Journal of Applied Physics* 131.23 (2022), p. 233902.

[190] T. J. Hayward. “Intrinsic Nature of Stochastic Domain Wall Pinning Phenomena in Magnetic Nanowire Devices”. In: *Scientific Reports* 5.13279 (2015).

[191] T. J. Hayward and K. A. Omari. “Beyond the quasi-particle: stochastic domain wall dynamics in soft ferromagnetic nanowires”. In: *Journal of Physics D: Applied Physics* 50.8 (Jan. 2017), p. 084006.

[192] E. Lage, R. Mattheis and J. McCord. "Stochasticity of domain wall pinning in curved ferromagnetic nanowires investigated by high-resolution Kerr microscopy". In: *Journal of Magnetism and Magnetic Materials* 487 (2019), p. 165273.

[193] B. Borie et al. "Geometrically enhanced closed-loop multi-turn sensor devices that enable reliable magnetic domain wall motion". In: *Applied Physics Letters* 111.24 (2017), p. 242402.

[194] T. A. Moore et al. "Magnetic-field-induced domain-wall motion in permalloy nanowires with modified Gilbert damping". In: *Phys. Rev. B* 82 (9 Sept. 2010), p. 094445.

[195] J.-Y. Lee, K.-S. Lee and S.-K. Kim. "Remarkable enhancement of domain-wall velocity in magnetic nanostripes". In: *Applied Physics Letters* 91.12 (2007), p. 122513.

[196] J. Brandão et al. "Understanding the role of damping and Dzyaloshinskii-Moriya interaction on dynamic domain wall behaviour in platinum-ferromagnet nanowires". In: *Scientific Reports* 7.1 (2017), pp. 1–10.

[197] K. Weerts et al. "Suppression of complex domain wall behavior in Ni80Fe20 nanowires by oscillating magnetic fields". In: *Applied Physics Letters* 96.6 (2010), p. 062502.

[198] E. R. Lewis et al. "Fast domain wall motion in magnetic comb structures". In: *Nature Materials* 9.12 (2010), pp. 980–983.

[199] X.-P. Ma et al. "Suppression of Walker breakdown in gapped magnetic nanowires". In: *Journal of Applied Physics* 124.8 (2018), p. 083905.

[200] J. Brandão and D. Atkinson. "Controlling the stability of both the structure and velocity of domain walls in magnetic nanowires". In: *Applied Physics Letters* 109.6 (2016), p. 062405.

[201] M. T. Bryan, T. Schrefl and D. A. Allwood. "Dependence of transverse domain wall dynamics on permalloy nanowire dimensions". In: *IEEE Transactions on Magnetics* 46.5 (2010), pp. 1135–1138.

[202] H.-G. Piao et al. "Domain wall propagation in wavy ferromagnetic nanowire". In: *IEEE Transactions on Magnetics* 45.10 (2009), pp. 3926–3929.

[203] D. M. Burn and D. Atkinson. "Suppression of Walker breakdown in magnetic domain wall propagation through structural control of spin wave emission". In: *Applied Physics Letters* 102.24 (2013), p. 242414.

[204] D. M. Burn, E. Arac and D. Atkinson. "Magnetization switching and domain-wall propagation behavior in edge-modulated ferromagnetic nanowire structures". In: *Physical Review B* 88.10 (2013), p. 104422.

[205] E. Semenova et al. "Field operating window of nanodevices employing the domain wall propagation through the stripes intersection: Numerical optimization". In: *Journal of Applied Physics* 124.15 (2018), p. 153901.

[206] O. Ozatay et al. "Spin-based data storage". In: (2016).

[207] M. J. Donahue and RD Mcmichael. "Head to head domain wall structures in thin magnetic stripes". In: *1997 IEEE International Magnetics Conference (INTERMAG)*. IEEE. 1997, GC–GC.

[208] J. Brandão et al. "Control of the magnetic vortex chirality in Permalloy nanowires with asymmetric notches". In: *Journal of Applied Physics* 116.19 (2014), p. 193902.

[209] K. A. Omari et al. "Toward Chirality-Encoded Domain Wall Logic". In: *Advanced Functional Materials* 29.10 (2019), p. 1807282.

[210] B. Borie. "The propagation and nucleation of magnetic domain walls in multi-turn counter sensor devices". PhD thesis. Johannes Gutenberg University Mainz, 2017.

[211] D. Ilgaz et al. "Domain-Wall Depinning Assisted by Pure Spin Currents". In: *Phys. Rev. Lett.* 105 (7 Aug. 2010), p. 076601. DOI: 10.1103/PhysRevLett.105.076601. URL: https://link.aps.org/doi/10.1103/PhysRevLett.105.076601.

[212] Y. F. Liu, J. W. Cai and L. Sun. "Large enhancement of anisotropic magnetoresistance and thermal stability in Ta/NiFe/Ta trilayers with interfacial Pt addition". In: *Applied Physics Letters* 96.9 (2010), p. 092509.

[213] M. Li et al. "Effect of a CoFeB layer on the anisotropic magnetoresistance of Ta/CoFeB/MgO/NiFe/MgO/CoFeB/Ta films". In: *Journal of Magnetism and Magnetic Materials* 439 (2017), pp. 17–21.

[214] *PREMA Semiconductor*. URL: https://www.prema.com/index.php/en/.